

VILNIUS GEDIMINAS TECHNICAL UNIVERSITY

Juozas MASĖNAS

**FLEXURAL STIFFNESS MODEL FOR
LAYERED CONCRETE ELEMENTS WITH
PARTIAL SHEAR CONNECTION**

DOCTORAL DISSERTATION

TECHNOLOGICAL SCIENCES,
CIVIL ENGINEERING (T 002)

Vilnius, 2026

The doctoral dissertation was prepared at Vilnius Gediminas Technical University in 2021–2026.

Supervisor

Prof. Dr Juozas VALIVONIS (Vilnius Gediminas Technical University, Civil Engineering – T 002).

The Dissertation Defence Council of the Scientific Field of Civil Engineering of Vilnius Gediminas Technical University:

Chairman

Prof. Dr Romualdas KLIUKAS (Vilnius Gediminas Technical University, Civil Engineering – T 002).

Members:

Prof. Dr Darius BAČINSKAS (Vilnius Gediminas Technical University, Civil Engineering – T 002),

Dr Eduardo CAVACO (NOVA University Lisbon, Portugal, Civil Engineering – T 002),

Prof. Dr Alfonsas DANIŪNAS (Vilnius Gediminas Technical University, Civil Engineering – T 002),

Prof. Dr Habil. Gintautas DZEMYDA (Vilnius University, Informatics Engineering – T 007).

The dissertation will be defended at the public meeting of the Dissertation Defence Council of Civil Engineering in the *Aula Doctoralis* Meeting Hall of Vilnius Gediminas Technical University at **10 a.m. on 14 May 2026**

Address: Saulėtekio al. 11, LT-10223 Vilnius, Lithuania.

Tel.: +370 5 274 4956; fax +370 5 270 0112; e-mail: doktor@vilniustech.lt

A notification on the intended defence of the dissertation was sent on 13 April 2026. A copy of the doctoral dissertation is available for review at Vilnius Gediminas Technical University repository <https://etalpykla.vilniustech.lt> and the Library of Vilnius Gediminas Technical University (Saulėtekio al. 14, LT-10223 Vilnius, Lithuania).

Vilnius Gediminas Technical University book No. 2026-018-M

<https://doi.org/10.20334/2026-018-M>

© Vilnius Gediminas Technical University, 2026

© Juozas Masėnas, 2026

juozas.masenas@vilniustech.lt

VILNIAUS GEDIMINO TECHNIKOS UNIVERSITETAS

Juozas MASĖNAS

SLUOKSNIUOTŲJŲ GELŽBETONINIŲ
KONSTRUKCIJŲ SU DALINAI
STANDŽIOMIS SLUOKSNIŲ JUNGTIMIS
LENKIAMOJO STANDUMO VERTINIMO
MODELIS

DAKTARO DISERTACIJA

TECHNOLOGIJOS MOKSLAI,
STATYBOS INŽINERIJA (T 002)

Vilnius, 2026

Disertacija rengta 2021–2026 metais Vilniaus Gedimino technikos universitete.

Vadovas

prof. dr. Juozas VALIVONIS (Vilniaus Gedimino technikos universitetas, Statybos inžinerija – T 002).

Vilniaus Gedimino technikos universiteto Statybos inžinerijos mokslo krypties disertacijos gynimo taryba:

Pirmininkas

prof. dr. Romualdas KLIUKAS (Vilniaus Gedimino technikos universitetas, Statybos inžinerija – T 002).

Nariai:

prof. dr. Darius BAČINSKAS (Vilniaus Gedimino technikos universitetas, Statybos inžinerija – T 002),

dr. Eduardo CAVACO (Naujasis Lisabonos universitetas, Portugalija, Statybos inžinerija – T 002),

prof. dr. Alfonsas DANIŪNAS (Vilniaus Gedimino technikos universitetas, Statybos inžinerija – T 002),

prof. habil. dr. Gintautas DZEMYDA (Vilniaus Universitetas, Informatikos inžinerija – T 007).

Disertacija bus ginama viešame Statybos inžinerijos mokslo krypties disertacijos gynimo tarybos posėdyje **2026 m. gegužės 14 d. 10 val.** Vilniaus Gedimino technikos universiteto *Aula Doctoralis* posėdžių salėje.

Adresas: Saulėtekio al. 11, LT-10223 Vilnius, Lietuva.

Tel.: (0 5) 274 4956; faksas (0 5) 270 0112; el. paštas doktor@vilniustech.lt

Pranešimai apie numatomą ginti disertaciją išsiųsti 2026 m. balandžio 13 d.

Disertaciją galima peržiūrėti Vilniaus Gedimino technikos universiteto talpykloje <https://etalpykla.vilniustech.lt/> ir Vilniaus Gedimino technikos universiteto bibliotekoje (Saulėtekio al. 14, LT-10223 Vilnius, Lietuva).

Abstract

Layered concrete structural elements consist of two or more concrete layers cast at different times and often with varying material properties. These elements can offer significant structural, architectural, and environmental advantages, provided that composite behaviour between the layers is maintained. The key factor governing this composite action is the performance of the interface between the concrete layers. In practice, the interface may exhibit reduced initial stiffness and will inevitably experience stiffness degradation as cracking develops. As the interface loses stiffness, the individual layers begin to perform more independently, leading to a reduction in the overall flexural stiffness of the layered element. Despite this, most current design codes lack an analytical approach for calculating deflections that account for interface partial shear connection, and such methods remain limited in scientific literature. In practice, standard reinforced concrete flexural analysis is typically suggested.

This dissertation proposes an analytical approach to determine the flexural stiffness (deflection) of layered concrete elements, accounting for the varying interface stiffness as the element deforms. The approach begins with an interface behaviour model, which describes the relationship between interface shear stress and layer slip. This model is characterised by four distinct stages of interface behaviour, each governed by different shear mechanisms, interface material properties, and a differential shrinkage effect. It remains applicable from the onset of interface loading through to significant interface deformations. From the shear stress-slip relationship, the variable interface shear stiffness modulus is derived. This modulus is then used in the second stage of the analytical approach: the built-up layers deflection estimation model. This model allows for the calculation of deflection in layered elements while accounting for the stiffness of individual layers, the composite stiffness of the entire element, evolving geometries due to cracking, and the changing interface shear stiffness.

Experimental and numerical analyses were conducted on concrete interfaces and layered concrete elements subjected to bending. The interface analysis provided insights into the effects of concrete strength, connector geometry and strength, differential shrinkage, interface roughness, and its overall geometry on interface strength, stiffness, and the intensity of different shear mechanisms. The analysis of layered beams and slabs clarified the cracking behaviour of individual concrete layers, the distribution of shear stress along the interface, the influence of connector inclination, and layer depth on flexural capacity and cracking patterns. Experimental results were used to validate the proposed analytical approach, showing strong agreement and confirming its effectiveness for analysing layered concrete elements.

Reziუმэ

Sluoksnuiotieji gelžbetoniniai konstrukciniai elementai susideda iš dviejų ar daugiau betono sluoksnių, betonuotų skirtingu laiku ir dažnai pasižyminčių skirtingomis medžiagų savybėmis. Šie elementai gali suteikti reikšmingų konstrukcinių, ekonominių ir aplinkosauginių pranašumų, jei užtikrinamas bendras sluoksnių darbas. Pagrindinis veiksnys, lemiantis šią kompozitinę elgseną, yra betono sluoksnių jungties darbas. Realiomis sąlygomis jungtis gali būti mažesnio (nei monolitinio) pradinio standumo. Galiausiai, standumas neišvengiamai mažėja jungčiai pleišėjant. Atskiri sluoksniai pradeda dirbti individualiau, dėl ko mažėja bendras sluoksniuotojo elemento lenkiamasis standumas. Daugumoje dabartinių projektavimo normų ir mokslinėje literatūroje trūksta analitinių įlinkio skaičiavimo metodų, vertinančių dalinį jungties standumą. Vietoj to rekomenduojama standartinė lenkiamo gelžbetoninio elemento analizė.

Disertacijoje siūlomas analitinis metodas sluoksniuotų gelžbetoninių elementų lenkiamajam standumui (įlinkiui) nustatyti, atsižvelgiant į kintantį jungties standumą elementui deformuojantis. Pirmas metodo žingsnis – jungties šlyties standumo modelis, kuris apibūdina santykį tarp jungties šlyties įtempių ir sluoksnių pasislinkimo. Modelis susideda iš keturių jungties elgsenos stadijų. Kiekvienoje stadijoje vertinami skirtingi šlyties mechanizmai. Šiame modelyje taip pat vertinamas ir sluoksnių traukumo skirtumo efektas. Jungties standumo modelis gali būti taikomas nuo jungties apkrovimo pradžios iki žymių jungties deformacijų. Iš žinomo šlyties įtempių ir sluoksnių pasislinkimo santykio nustatomas kintantis jungties šlyties standumo modulis. Šis dydis naudojamas antrajame analitinio metodo etape – sudėtinių sluoksnių modelyje. Šiuo modeliu apskaičiuojamas sluoksniuoto elemento įlinkis, atsižvelgiant į atskirų sluoksnių standumą, viso elemento kompozitinį standumą, kintantį jungties šlyties standumą ir kintančias geometrines charakteristikas dėl sluoksnių pleišėjimo.

Eksperimentinė ir skaitinė analizė atlikta tiriant sluoksnių jungtis ir sluoksniuotus lenkiamus gelžbetoninius elementus. Jungties analizės rezultatai suteikė žinių apie betono stiprumo, jungties inkarų geometrijos ir stiprumo, sluoksnių traukumo skirtumo, jungties šurkštumo ir jos geometrijos įtaką jungties stiprumui, standumui ir skirtingų šlyties mechanizmų intensyvumui. Lenkiamųjų elementų analizė suteikė žinių apie betono sluoksnių pleišėjimo pobūdį, šlyties įtempių pasiskirstymą jungtyje, inkarų išdėstymo ir sluoksnio storio įtaką lenkiamajai galiai ir pleišėjimo pobūdžiui. Eksperimentiniai rezultatai buvo naudojami siūlomo analitinio metodo validacijai. Dėl artimo eksperimentinių ir analitinių rezultatų sutapimo galima patvirtinti pasiūlyto analitinio metodo tinkamumą sluoksniuotų elementų analizei.

Notations

Symbols

- G_{eff} – interface shear stiffness modulus (liet. *jungties šlyties standumo modulis*);
 τ – interface shear stress (liet. *jungties šlyties įtempiai*);
 s – interface layer slip (liet. *jungties sluoksnių pasislinkimas*);
 E_c – concrete elastic modulus (liet. *betono tamprumo modulis*);
 η – shear stress intensity coefficient (liet. *šlyties įtempių intensyvumo koeficientas*);
 f_{ct} – concrete tensile strength (liet. *betono tempiamasis stipris*);
 f_c – concrete compressive strength (liet. *betono gniuždomasis stipris*);
 f_y – reinforcement/connector yield stress (liet. *armatūros / inkarų takumo įtempiai*);
 S_{L1} – first moment of area of the bottom layer (liet. *pirmojo sluoksnio statinis momentas*);
 S_L – first moment of area of composite cross-section (liet. *kompozitinio skerspjuvio statinis momentas*);
 κ – concrete and connectors' contribution coefficient (liet. *betono ir inkarų įtakos koeficientas*);
 D – fourth interface behaviour stage coefficient (liet. *ketvirtos jungties darbo stadijos koeficientas*);
 μ – interface surface friction coefficient (liet. *jungties paviršiaus trinties koeficientas*);
 α_c – connector inclination angle (liet. *inkarų posvyrio kampas*);
 ρ – connector ratio (liet. *inkarų santykis*);
 A_s – connector cross-sectional area (liet. *inkarų skerspjuvio plotas*);

σ_n – compressive stress (liet. *gniuždomieji įtempiai*);
 τ_{fr} – friction shear stress (liet. *trinties šlyties įtempiai*);
 τ_{dw} – dowel action shear stress (liet. *kaiščio efekto šlyties įtempiai*);
 σ_{sh} – differential shrinkage shear stress (liet. *sluoksnių susitraukimo skirtumo efekto šlyties įtempiai*);
 F_v – differential shrinkage longitudinal force (liet. *sluoksnių susitraukimo skirtumo efekto išilginė jėga*);
 F – second layer tensile force (liet. *antro sluoksnio tempiamoji jėga*);
 M_c – composite cross-section bending moment (liet. *kompozitinio skerspjūvio lenkimo momentas*);
 M_1 – first layer bending moment due to bent reinforcement (liet. *pirmojo sluoksnio lenkimo momentas dėl lenkiamos armatūros*);
 M_2 – second layer bending moment due to bent reinforcement (liet. *antrojo sluoksnio lenkimo momentas dėl lenkiamos armatūros*);
 S – first moment of area of one layer (liet. *vieno sluoksnio statinis momentas*);
 I_c – moment of inertia of composite cross-section (liet. *kompozitinio skerspjūvio inercijos momentas*);
 e – distance between composite and second layer centroids (liet. *atstumas tarp kompozitinio ir antro sluoksnio svorio centrų*);
 l_i – interface length (liet. *jungties ilgis*);
 b – interface width (liet. *jungties plotis*);
 h_2 – second layer height (liet. *antro sluoksnio aukštis*);
 y_1 – bottom-centroid first layer distance (liet. *pirmo sluoksnio apačios-svorio centro atstumas*);
 y_2 – top-centroid second layer distance (liet. *antro sluoksnio viršaus-svorio centro atstumas*);
 a_1 – bottom-reinforcement first layer distance (liet. *pirmo sluoksnio apačios-armatūros centro atstumas*);
 a_2 – top-reinforcement first layer distance (liet. *antro sluoksnio viršaus-armatūros centro atstumas*);
 A_2 – second layer cross-section area (liet. *antro sluoksnio skerspjūvio plotas*);
 A_{s1} – first layer reinforcement area (liet. *pirmo sluoksnio armatūros plotas*);
 A_{s2} – first layer reinforcement area (liet. *antro sluoksnio armatūros plotas*);
 m – first-second layer elastic modulus ratio (liet. *pirmo-antro sluoksnių tamprumo modulių santykis*);
 $E_{c,eff}$ – composite cross-section concrete elastic modulus (liet. *kompozitinio skerspjūvio betono tamprumo modulis*);
 E_s – reinforcement elastic modulus (liet. *armatūros tamprumo modulis*);
 ε_1 – first layer free shrinkage (liet. *pirmo sluoksnio laisvosios traukumo deformacijos*);
 ε_2 – second layer free shrinkage (liet. *antro sluoksnio laisvosios traukumo deformacijos*);
 ε_s – differential shrinkage strain (liet. *sluoksnių susitraukimo deformacijų skirtumas*);
 $\varepsilon_{2,y}$ – second layer centroid shrinkage strain (liet. *traukumo deformacija antro sluoksnio svorio centre*);

$\varepsilon_{1,t}$ – shrinkage strain at the top of the first layer (liet. *traukumo deformacija pirmo sluoksnio viršuje*);
 $\varepsilon_{2,t}$ – shrinkage strain at the top of the second layer (liet. *traukumo deformacija antro sluoksnio viršuje*);
 $\varepsilon_{1,0}$ – initial first-layer shrinkage (liet. *pradinė pirmo sluoksnio traukumo deformacija*);
 $\varepsilon_{2,c}$ – concrete tensile strain (liet. *betono tempiamoji deformacija*);
 $\varepsilon_{2,r}$ – shrinkage restriction due to contact between the layers (liet. *traukumo suvaržymas dėl sluoksnių kontakto*);
 $\varepsilon_{2,s}$ – shrinkage restriction due to layer size effect (liet. *traukumo suvaržymas dėl sluoksnių dydžio efekto*);
 σ_c – tensile stress in concrete due to shrinkage (liet. *tempimo įtempiai betone dėl traukumo*);
 R – shrinkage restriction coefficient (liet. *traukumo suvaržymo koeficientas*);
 w – deflection (liet. *įlinkis*);
 l – span of the element under bending (liet. *lenkiamo elemento tarpatramis*);
 M – bending moment of the element under bending (liet. *lenkiamo elemento lenkiamasis momentas*);
 $E_{eff} I_{eff}$ – flexural stiffness of the layered element (liet. *sluoksniuoto elemento lenkiamasis standumas*);
 $1/D$ – flexural stiffness of layered element (liet. *sluoksniuoto elemento lenkiamasis standumas*);
 λ – coefficient, describing interface shear stiffness (liet. *koeficientas, apibudinantis jungties šlyties standumą*);
 γ – coefficient, describing interface shear stiffness (liet. *koeficientas, apibudinantis jungties šlyties standumą*);
 α – coefficient, describing interface shear stiffness (liet. *koeficientas, apibudinantis jungties šlyties standumą*);
 $A_{eff,1,cr}$ – first layer cross-sectional area (liet. *pirmo sluoksnio skerspjūvio plotas*);
 $A_{eff,2,cr}$ – second layer cross-sectional area (liet. *antro sluoksnio skerspjūvio plotas*);
 $I_{eff,1,cr}$ – first layer moment of inertia (liet. *pirmo sluoksnio inercijos momentas*);
 $I_{eff,2,cr}$ – second layer moment of inertia (liet. *antro sluoksnio inercijos momentas*);
 $E_{c,eff,1}$ – first layer concrete elastic modulus (liet. *pirmo sluoksnio betono tamprumo modulis*);
 $E_{c,eff,2}$ – second layer concrete elastic modulus (liet. *antro sluoksnio betono tamprumo modulis*);
 z_{eff} – distance between centroids of the layers (liet. *atstumas tarp sluoksnių svorio centrų*);
 $x_{i,cr}$ – neutral axis of cracked cross-section (liet. *supleišėjusio skerspjūvio neutraliosios ašies padėtis*);
 d_i – layer effective depth (liet. *naudingasis sluoksnio skerspjūvio aukštis*);
 V – transverse load (liet. *skersinė apkrova*).

Abbreviations

- DIC – digital image correlation (liet. *skaitmeninės vaizdo koreliacijos metodas*);
EC – Eurocode (liet. *konstrukcijų projektavimo standartas „Eurokodas“*);
LVDT – linear variable differential transformer (liet. *tiesinis kintamo diferencialo transformatorius*);
MC – Model Code (liet. *konstrukcijų projektavimo standartas „Model Code“*);
RC – reinforced concrete (liet. *gelžbetonis*);
RMSE – root mean square error (liet. *vidutinis kvadratinis nuokrypis*);
UHPFRC – ultra-high-performance fibre-reinforced concrete (liet. *itin aukšto stiprumo pluoštu armuotas betonas*).

Contents

INTRODUCTION	1
Problem Formulation.....	1
Relevance of the Dissertation.....	2
Research Objects.....	2
Aim of the Dissertation	3
Tasks of the Dissertation	3
Research Methodology.....	3
Scientific Novelty of the Dissertation	4
Practical Value of the Research Findings.....	4
Defended Statements.....	5
Approval of the Research Findings	5
Structure of the Dissertation.....	6
Acknowledgements	6
1. FLEXURAL STIFFNESS ANALYSIS OF LAYERED CONCRETE ELEMENTS WITH PARTIAL SHEAR CONNECTION INTERFACES.....	7
1.1. Analysis of Concrete Interface Research.....	7
1.2. Analysis of Concrete Interface Behaviour Models.....	11
1.2.1. Interface Shear Resistance Models.....	11
1.2.2. Interface Shear Stiffness Models	15
1.3. Engineering Characteristics and Review of Experimental Studies of Layered Concrete Elements Under Bending.....	20
1.3.1. Types and Characteristics of Layered Concrete Elements	20

1.3.2. Review of Experimental Studies of Layered Concrete Elements	23
1.4. Methods for Calculating Flexural Stiffness of Layered Concrete Elements with Partial Shear Connection Interfaces	30
1.4.1. Magnucki et al. Model.....	30
1.4.2. Foraboschi Model.....	33
1.4.3. Peng et al. Model.....	37
1.4.4. Marčiukaitis et al. Model.....	39
1.4.5. Comparison of Flexural Stiffness Models	41
1.5. Conclusions of the First Chapter and Formulation of the Dissertation Tasks	42
2. STIFFNESS MODELS FOR LAYERED CONCRETE INTERFACES AND LAYERED CONCRETE ELEMENTS UNDER BENDING	45
2.1. Shear Stiffness Model for Layered Concrete Interface	45
2.2. Flexural Stiffness Model for Layered Concrete Beams with Partial Shear Connection Interfaces	53
2.3. Numerical Model of Layered Concrete Element with Partial Shear Connection Interface	55
2.3. Conclusions of the Second Chapter.....	61
3. EXPERIMENTAL INVESTIGATIONS OF LAYERED CONCRETE ELEMENTS WITH PARTIAL SHEAR CONNECTION INTERFACES	63
3.1. Experimental Investigation of Concrete Interface	63
3.2. Experimental Investigation of Layered Concrete Beams	77
3.3. Experimental Investigation of Semi-Precast Concrete Slabs with Plastic Void Formers	85
3.4. Comparative Analysis of Theoretical and Experimental Results	91
3.4.1. Theoretical Interface Behaviour Model Validation	91
3.4.2. Layered Concrete Element Flexural Stiffness Model Validation	96
3.5. Conclusions of the Third Chapter.....	107
GENERAL CONCLUSIONS	109
REFERENCES	111
LIST OF SCIENTIFIC PUBLICATIONS BY THE AUTHOR ON THE TOPIC OF THE DISSERTATION.....	119
SUMMARY IN LITHUANIAN.....	121
ANNEXES.....	137
Annex A. Push-Off Specimen Characteristics	138

Introduction

Problem Formulation

Structural elements composed of concrete layers cast at different times, often with different properties, are referred to as layered concrete structural elements. When an additional layer of higher-strength concrete is used, such elements may offer several advantages over solid cross-sections, including lower material consumption, smaller structural depth, reduced deflections, and increased shear capacity. Concrete overlays may also be used to strengthen existing structures, making renovation more sustainable by reducing demolition, material use, and waste. In addition, layered elements can incorporate plastic void formers, which reduce self-weight and concrete volume while providing environmental benefits through lower cement consumption and the use of recycled plastic. Examples of layered concrete structural elements include filigree slabs, bridge girders with concrete decks, and hollow-core slabs with an additional concrete topping. Concrete may also be cast in stages for technological reasons.

The performance of layered concrete structural elements largely depends on the characteristics of the interface between the layers. Insufficient bond reduces the shear stiffness of the interface and, consequently, the overall flexural stiffness of the element under bending. Studies have shown (Cavaco & Camara, 2017; Foraboschi, 2009; Marčiukaitis et al., 2006) that interfaces in layered structures

rarely exhibit full-shear connection and should be treated as elements of partial-shear connection, even before loading.

Most concrete design codes and existing theoretical models do not account for the partial-shear connection of concrete interfaces. They commonly assume a perfectly bonded interface and recommend structural analysis procedures identical to those used for solid cross-section elements, as a result, overestimating the flexural stiffness of a layered concrete element. Neglecting discrete concrete layers introduces additional significant limitations. Ignoring the distinct material properties and geometric characteristics of a layer leads to additional inaccurate predictions of flexural stiffness. Furthermore, disregarding the performance of individual layers prevents predicting individual layer cracking. Lastly, existing analytical models reported in the literature do not account for the differential shrinkage effect arising from different casting times of concrete layers. This phenomenon induces interface stresses that reduce interface strength and stiffness.

Relevance of the Dissertation

This dissertation presents an analysis of concrete interfaces and the behaviour of layered concrete elements subjected to bending. Novel theoretical models for interface strength and stiffness, differential shrinkage effect, and for the flexural stiffness of layered elements are introduced. Together, these developments propose a new analytical layered concrete element stiffness approach that explicitly incorporates the partial-shear connection of the interface. The experimental and numerical investigations carried out in this work deepen the understanding of layered concrete elements and their interfaces, including the factors that influence their performance. The proposed theoretical models broaden the analytical possibilities for evaluating such elements. By appropriately accounting for interface behaviour and more accurately predicting structural performance, safer and more efficient design of layered concrete elements can be achieved. This, in turn, enables the effective use of their advantages: reduced material consumption, faster construction, environmentally favourable solutions, and both structural and economic benefits.

Research Objects

The objects of the presented research are the behaviour analysis of layered concrete elements, the shear stiffness model of concrete layer interfaces, and the flexural stiffness model of layered concrete elements, all subjected to static monotonic short-term load.

Aim of the Dissertation

This dissertation aims to develop an analytical model for evaluating the flexural stiffness of layered concrete elements under bending, accounting for the properties and behaviour of the layer interfaces.

Tasks of the Dissertation

The following research tasks were defined:

1. To review existing research on layered concrete interfaces and layered concrete elements subjected to bending, including previously proposed theoretical models describing interface behaviour and flexural behaviour of a layered element under bending.
2. To develop an analytical model for concrete interface behaviour, which accounts for the differential shrinkage effect.
3. To develop an analytical flexural stiffness model for layered concrete elements under bending, which accounts for partial interface shear connection.
4. To perform a numerical analysis of a semi-precast concrete slab incorporating plastic void formers.
5. To carry out experimental investigations of layered concrete interfaces, layered concrete beams and layered concrete slabs.
6. To validate the proposed analytical models by comparing analytical results to experimental test and numerical analysis results.

Research Methodology

To investigate the research objects, the following methods were employed:

- Theoretical methods: analytical models describing the behaviour of concrete interfaces and layered concrete elements subjected to bending were developed. In addition, a numerical model of a layered concrete element was created.
- Experimental methods: concrete interfaces and layered concrete elements under bending were experimentally tested.
- Statistical methods: conclusions were drawn by collecting, analysing and explaining the statistical data.

Scientific Novelty of the Dissertation

The scientific novelty of the theoretical and experimental investigations of layered concrete elements is summarised as follows:

1. Novel analytical calculation models were created capable of predicting the stiffness and shear strength of layered concrete interfaces, as well as the flexural stiffness of layered concrete elements with partial-shear connection interfaces.
2. A new theoretical model was created to determine differential shrinkage strain and the resulting differential shrinkage-induced interface shear stress, affecting interface performance.
3. Novel data was produced on the factors governing the strength and stiffness of layered concrete interfaces and layered concrete elements under bending, including analysis of failure modes and cracking behaviour.
4. Novel data was produced on the numerical modelling procedures and numerical analysis of layered concrete elements.

Practical Value of the Research Findings

The aspects of practical value in the theoretical and experimental investigations of layered concrete elements are as follows:

1. A novel theoretical calculation model that can be used in the design of layered concrete interfaces. This model enables the selection of optimal material properties and reduces the risk of prevalent failure modes.
2. A novel differential shrinkage model for evaluating the severity of differential shrinkage effects on concrete interface shear resistance and stiffness.
3. A novel theoretical flexural stiffness model that can be applied in the design of layered concrete elements with partial-shear connection interfaces. By accounting for the actual interface shear stiffness, this model allows for a more accurate estimation of the flexural stiffness of the layered element.
4. Experimental results for concrete interfaces and layered concrete elements provide practical insights into failure modes, cracking patterns, material influences, and other factors governing the behaviour of the studied elements.

5. By using the analysis data presented in this dissertation, the practical benefits of layered concrete elements can be more effectively exploited, including reduced material consumption, accelerated construction, environmentally favourable engineering solutions, structural and economic advantages.

Defended Statements

The following statements, based on the results of the present investigation, may serve as the official hypotheses to be defended:

1. The proposed analytical method for layered concrete interface behaviour accurately predicts the interface shear stress–layer slip relationship throughout the four stages of interface behaviour. From known shear stress and corresponding slip values, the interface shear stiffness modulus can be determined.
2. The proposed differential shrinkage model accurately predicts differential shrinkage strain and the resulting differential shrinkage-induced interface shear stress.
3. The proposed analytical method, which accounts for partial interface shear connection, accurately predicts the deflection of layered concrete elements subjected to bending across different levels of interface stiffness and imposed loading.

Approval of the Research Findings

The research findings of the dissertation have been published in five scientific articles, four of them in Web of Science journals with an Impact Factor. The research results were presented at three scientific conferences, two of which were international:

- 25th Conference for Lithuanian Junior Researchers “Science – Future of Lithuania”, Civil Engineering. Vilnius, Lithuania, 2021.
- 14th International Conference Modern Building Materials, Structures and Techniques (MBMST 2023). Vilnius, Lithuania.
- 5th International Conference on Civil Engineering Fundamentals and Applications (ICCEFA 2024). Lisbon, Portugal.

Structure of the Dissertation

The dissertation consists of an introduction, three chapters, general conclusions, a list of references, a list of the author's publications related to the topic of the dissertation, and a summary in Lithuanian.

Excluding the annexes, the dissertation comprises 136 pages and has 139 numbered equations, 91 figures, 22 tables, and 102 references.

Acknowledgements

The author of this dissertation would like to express his deepest gratitude to his supervisor, Prof. Dr Juozas Valivonis, Head of the Department of Reinforced Concrete Structures and Geotechnics, for his valuable guidance, shared knowledge, and constant encouragement throughout the course of this research.

Sincere appreciation is also extended to all those who assisted during the experimental phase of the research. The author gratefully acknowledges Gintaras Jurkėnas, Head of the Laboratory of Building Structures and Geotechnics, as well as Dr Aleksandr Sokolov, Lolita Kairytė, Juozas Gervė, Aleksandr Zajac, Grigorij Kuksov, and Lukas Ravnaličėvas for their invaluable technical support. The contribution and collaboration of fellow PhD colleagues are also sincerely appreciated. Gratitude is further extended to Doc. Dr Remigijus Šalna, Dean of the Faculty of Civil Engineering, for his encouragement and support.

The author also wishes to express his appreciation to the colleagues at NOVA University Lisbon, where a research internship and the research presentation were conducted. Special thanks go to Dr Eduardo Cavaco and fellow PhD students Barbara Gomes and Peiman Ghaderi for their generous exchange of knowledge regarding the mechanics of layered concrete elements, numerical modelling, and concrete structural behaviour.

The author would also like to express his gratitude to the company "Aksa" for manufacturing the precast components of the filigree slabs used in the experimental research, and to the company "Arkada" for their assistance during various preparation stages of the experimental specimens.

Some of the research was conducted as part of the execution of Project "Mission-driven Implementation of Science and Innovation Programmes" (No. 02-002-P-0001), funded by the Economic Revitalization and Resilience Enhancement Plan "New Generation Lithuania".

Finally, the author would like to thank his family, his parents, for encouraging him to pursue doctoral studies, and his wife, Viktorija and his children, for their calming presence, unwavering support, and for providing the opportunity to continue his education and personal development.

Flexural Stiffness Analysis of Layered Concrete Elements with Partial Shear Connection Interfaces

This chapter presents a review of published studies on the behaviour of layered concrete interfaces and layered concrete elements under bending. It examines methods found in the literature for determining interface strength and shear stiffness. In addition, practical engineering solutions and experimental investigations of layered concrete elements with partial shear connection interfaces are analysed, together with existing analytical methods for predicting their flexural stiffness. Finally, the chapter concludes with a summary and the formulation of the dissertation tasks. The aspects discussed here have been addressed in the author's previously published works (Masénas, 2022; Masénas et al., 2021, 2023; Masénas & Valivonis, 2024a, 2024b, 2025; Valivonis et al., 2026).

1.1. Analysis of Concrete Interface Research

In the design and construction of concrete structural elements, a cross-section with varying material properties can arise either as a deliberate design choice or simple inevitability during the assembly of a broader structural system. These types of

structural elements, known as layered concrete elements, present both advantages and limitations when compared to traditional solid cross-section elements. Unlike solid sections, layered systems can offer shorter construction times, as seen with filigree slabs (Cao et al., 2024; Hillebrand et al., 2021; Newell & Goggins, 2019). They also enable reductions in material usage and facilitate waste management through the incorporation of void formers (Molkens & Van Gysel, 2021; Valivonis et al., 2015), achieved by lowering cement consumption and using recycled-plastic formers. Void formers additionally allow longer slab spans, which may be architecturally advantageous. Filigree slab can be combined with other structural elements, like cantilever balconies, and other architectural features. Use of a filigree slab also opens a possibility for a continuous concrete slab (Hillebrand & Hegger, 2023). Layered concrete elements also appear in retrofit applications. By adding a new concrete layer to an existing structural element, the strength or stiffness of the older element can be increased (Mansour et al., 2017; Mokhtari & Hassan, 2024; Mones & Breña, 2013; Rahman et al., 1999; J. L. Silfwerbrand, 2009). This approach is beneficial not only structurally but also environmentally, as it strengthens the existing element rather than replacing it, thereby reducing material consumption (Daneshvar et al., 2022). Additional examples of layered concrete elements include bridge components (Abu-Abaileh & Soltani, 2026; Mahmoodreza, 2016) and multi-layered structures formed due to interrupted construction processes. Researchers have also reported that casting a self-compacting concrete layer onto an existing concrete element reduces vibration in the resulting layered element (Yuan et al., 2023). All such cases fall within the scope of layered concrete structural element research.

The appropriate performance of a layered concrete element is only ensured when full composite action is maintained between its layers. This requirement is governed primarily by the characteristics of the interface. As interface stresses increase, cracks may form, and the interface shear stiffness decreases, causing the layers to act more independently. The susceptibility of the concrete interface to failure is therefore the principal weakness of layered concrete elements. Interface opening perpendicular to the plane of the interface corresponds to Mode I failure, while failure caused by relative layer slip corresponds to Mode II failure (Cavaco & Camara, 2017), as illustrated in Figure 1.1.

Studies on layered concrete elements conclude that both the stiffness and capacity of the interface must be considered, and that, in general, the interface should be treated as an element of partial shear connection (Cavaco & Camara, 2017; Foraboschi, 2009; Marčiukaitis et al., 2006). The conventional flexural stiffness analysis might overestimate the flexural stiffness of a layered concrete element (Zajac et al., 2021). Due to the lack of analytical models for interface shear stiffness and the limited availability of flexural stiffness models that account

for interface characteristics, this dissertation focuses on investigating the flexural stiffness of layered concrete elements.

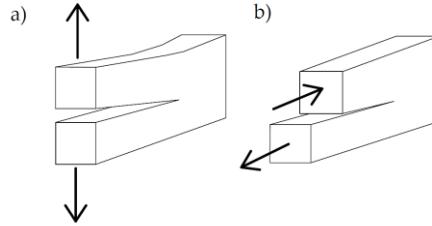


Fig. 1.1. Concrete fracture mechanics: a) Mode I fracture; b) Mode II fracture (Guo et al., 2017)

The performance of the interface is governed by several shear-transfer mechanisms, each contributing to the interface's ability to resist normal and shear stresses. Adhesion represents the chemical bond formed between concrete layers, while mechanical interlock arises from the micro-roughness of the interface surface (Barbosa et al., 2017; International Federation for Structural Concrete (fib), 2020). These mechanisms are illustrated in Figure 1.2. Adhesive strength increases with the concrete's compressive strength, and mechanical interlock improves with both higher strength and greater surface roughness. Factors that reduce adhesion and interlock include surface contamination (laitance, dust, and grease) (Manawadu et al., 2023; B. Zhang et al., 2022), improper surface moisture conditions (Daneshvar et al., 2022), and differential shrinkage between layers (Beushausen & Alexander, 2007; Elliott & Jolly, 2014; Y. Fang et al., 2021; Lam et al., 2019; J. Silfwerbrand, 1997). If the interface is uncracked before loading, adhesion and mechanical interlock are the first mechanisms resisting shear. Once adhesive bonds and surface protrusions fail, typically at very small slip values (around 0.05 mm or slightly higher), other shear-transfer mechanisms assume the load. In this initial stage, while adhesion and interlock dominate, the interface behaviour remains stiff (International Federation for Structural Concrete (fib), 2020).

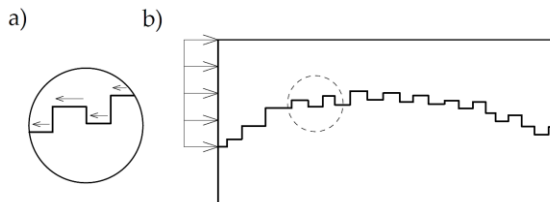


Fig. 1.2. Concrete layer mechanical interlock and adhesion (International Federation for Structural Concrete (fib), 2020)

Another interface shear mechanism is shear friction, which may be divided into two forms: friction generated by compressive force acting perpendicular to the interface, and friction produced by connector-induced clamping. These mechanisms are illustrated in Figure 1.3a and b. Compressive friction develops when the layers begin to slip, and the interface deformation is resisted by surface roughness in combination with perpendicular compression. Increasing either the interface roughness or the applied compression results in higher shear friction resistance (Widodo, 2017). Clamping friction arises when slip causes the interface to open perpendicularly due to surface roughness (Gołdyn, 2022), inducing tension in the connectors (steel reinforcement crossing the interface). The tensile resistance of these connectors creates a clamping force. Clamping friction depends on the degree of interface roughness and on the properties and quantity of the interface connectors. Shear friction is characteristic of the ductile stage of interface behaviour (Davaadorj et al., 2020; European Committee for Standardization, 2023; International Federation for Structural Concrete (fib), 2020).

The final interface shear mechanism is dowel action. This phenomenon is illustrated in Figure 1.3c. As the layers slip, the interface connectors are subjected to shear forces. When these connectors are properly anchored, they also undergo bending, resulting in a combined stress state of shear and bending known as dowel action. The dowel action shear force increases with higher connector ratios, higher concrete strength, and higher connector strength. This mechanism is associated with ductile stages of interface behaviour (European Committee for Standardization, 2023; International Federation for Structural Concrete (fib), 2020).

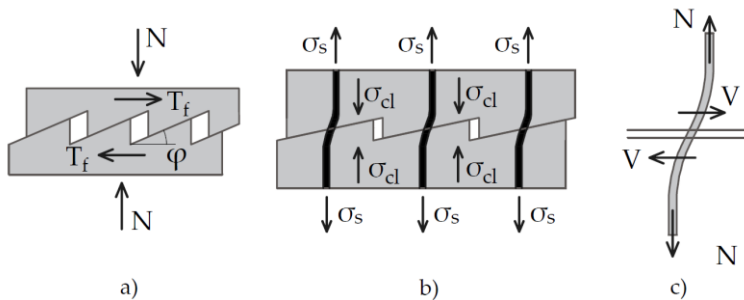


Fig. 1.3. Concrete shear mechanisms: a) friction due to compression; b) friction due to clamping; c) dowel action

The contribution of each interface shear mechanism develops at different stages of interface behaviour, corresponding to different magnitudes of slip. For instance, when the interface shear stress is primarily resisted by adhesion and mechanical interlock, the connectors do not yet experience significant deformation, and dowel action does not occur. Conversely, when dowel action governs the

shear transfer, the adhesive bonds and mechanical interlock mechanisms have already failed (Barbosa et al., 2017; Liu et al., 2019, 2021; Shaw & Sneed, 2014).

1.2. Analysis of Concrete Interface Behaviour Models

1.2.1. Interface Shear Resistance Models

The earliest attempts to theoretically predict the behaviour of concrete interfaces were made by Anderson (1960), Hanson (1960), Mattock and Kaar (1961), Sae-mann and Washa (1964), and Gaston and Kriz (1964). However, the model most widely recognised as the foundation of analytical interface behaviour is the shear-friction theory proposed by Birkeland and Birkeland (1966), which has since been refined by numerous researchers. This model provides an expression for the interface shear resistance (Eq. 1.1):

$$v_u = \mu \rho f_y = \tan(\varphi) \rho f_y, \quad (1.1)$$

here, μ – interface surface friction coefficient, φ – sawtooth model angle, ρ – interface connector ratio, and f_y – connector yield stress. This equation is accompanied by Figure 1.4, which illustrates the underlying mechanics of the shear-friction model.

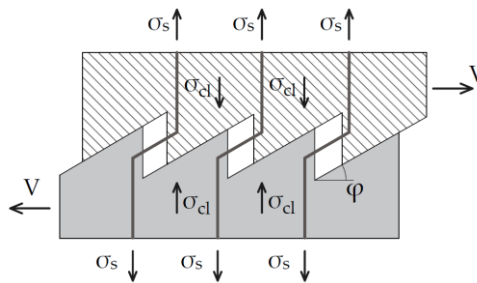


Fig. 1.4. Shear friction theory mechanism (Birkeland & Birkeland, 1966)

Here, the interface roughness is represented as two interlocking sawtooth surfaces in contact. The interface is crossed by connectors, and the figure illustrates the clamping shear mechanism. As the layers slip relative to one another, the inclined surface profile causes the interface to open in the direction perpendicular to the interface plane. This opening places the connectors in tension, and the resulting clamping force generates shear resistance along the interface.

Loov (1978) was the first to propose a shear resistance model that incorporated the influence of concrete strength (Eq. 1.2):

$$\frac{v_u}{f_c} = k \sqrt{\frac{\rho f_y + \sigma_n}{f_c}}, \quad (1.2)$$

here, v_u – interface shear resistance, k – constant, for which a value of $k = 0.5$ is recommended for uncracked interface, σ_n – normal stress, acting perpendicular to the interface, and f_c – concrete compressive strength.

Vecchio and Collins (1986) proposed an interface behaviour model aimed at predicting the shear resistance of an already cracked interface. This model does not consider connector characteristics and focuses on the influence of concrete properties, primarily mechanical interlock. The equation for estimating the interface shear resistance is presented in Eq. 1.3:

$$v_u = 0.18v_{ci\ max} + 1.64f_{ci} - 0.82 \frac{f_{ci}^2}{v_{ci\ max}}, \quad (1.3)$$

$$v_{ci\ max} = \frac{\sqrt{f_c}}{0.31 + \frac{24w}{a+16}}, \quad (1.4)$$

here, $v_{ci\ max}$ – shear stress resistance of interface crack, f_{ci} – compressive stress at the interface, w – current interface crack width, and a – concrete aggregate size. Values for w and a are in mm, and f_c in MPa. The model can be explained by Figure 1.5.

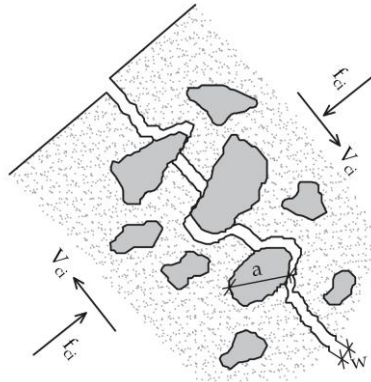


Fig. 1.5. Vecchio & Collins interface crack mechanism (Vecchio & Collins, 1986)

Mattock (Mattock, 1988) proposed a model that includes a cohesion shear mechanism (Eq. 1.5):

$$v_u = 0.467 f_c^{0.545} + 0.8(\rho f_y + \sigma_n). \quad (1.5)$$

Lin and Chen (1989) proposed an equation intended as a more accurate alternative to the expressions used in American design codes. Their study considered concrete strengths ranging from 20.59 MPa to 68.65 and steel stresses ρf_y between 1.2 and 19.5 MPa. The resulting expression for interface shear resistance is presented in Eq. 1.6:

$$v_u = \mu_e (\rho f_y + \sigma_n). \quad (1.6)$$

The equivalent friction coefficient determined according to Eq. 1.7:

$$\mu_e = \left(\frac{1.75\sqrt{f_c}}{\rho f_y + \sigma_n} \right)^{0.5} \leq 0.8 f_c^{0.25}. \quad (1.7)$$

Randl (1997) proposed an equation that incorporates the contributions of cohesion, compressive friction, and dowel action as the governing shear mechanisms (Eq. 1.8):

$$v_u = \tau_{coh} + \mu\sigma_n + \alpha\rho\sqrt{f_c f_y}, \quad (1.8)$$

here, τ_{coh} – interface cohesion shear stress, $\mu\sigma_n$ – friction due to compression, $\alpha\rho\sqrt{f_c f_y}$ – dowel action shear stress, and α – dowel action coefficient. Cohesion can be determined as follows (Eq. 1.9):

$$\tau_{coh} = c \frac{f_{ck}^{\frac{1}{3}}}{\gamma_{coh}}, \quad (1.9)$$

here, c – cohesion coefficient and γ_{coh} – safety factor, considering interface surface preparation variabilities.

A similar configuration for interface shear resistance modelling appears in several subsequent interface models. One such model was introduced in the first-generation Eurocode 2 (ECS, 2006). A notable advantage of this formulation is that it explicitly accounts for the inclination angle of interface connectors. The corresponding expression is presented in Eq. 1.10:

$$v_{Rdi} = c f_{ct} + \mu\sigma_n + \rho f_y (\mu \sin\alpha + \cos\alpha), \quad (1.10)$$

here, c – cohesion coefficient, f_{ct} – tensile concrete strength, μ – interface surface friction coefficient, σ_n – normal stress due to external compression, ρ – connector ratio, f_y – connector yield stress, α – connector inclination angle. Here, member cf_{ct} represents interface cohesion, $\mu\sigma_n$ – interface friction due to compression, and $\rho f_y(\mu\sin\alpha + \cos\alpha)$ – friction due to connector clamping.

Similarly, Model Code 2020 (International Federation for Structural Concrete (fib), 2020) provides an interface model conceptually aligned with the approach introduced by Randl (1997). The interface shear resistance can be determined as follows (Eq. 1.11):

$$\tau_u = \tau_c + \mu(\rho\kappa_1 f_y + \sigma_n) + \kappa_2 \rho \sqrt{f_y f_c}, \quad (1.11)$$

here, κ_1 and κ_2 – coefficients considering the degree of contribution of shear mechanisms. Presented shear mechanisms: τ_c – adhesion, interlocking, $\mu(\rho\kappa_1 f_y + \sigma_n)$ – friction mechanism, and $\kappa_2 \rho \sqrt{f_y f_c}$ – dowel action. This equation is similar to that proposed by the Randl equation; however, by applying different coefficients, the contributions of the individual interface shear mechanisms can be adjusted.

Second-generation Eurocode 2 (European Committee for Standardization, 2023) presented a novel detailed methodology for determining concrete shear resistance. The code suggests two equations for two different cases. For interfaces without connectors, or in cases where the anchorage of the connectors is sufficient to ensure that the connector stress can be taken $\sigma_{sd} = f_{yd}$, the following expression is recommended (Eq. 1.12):

$$\tau_{Rdi} = c_v \sqrt{f_c} + \mu_v \sigma_n + \rho f_y (\mu_v \sin\alpha + \cos\alpha). \quad (1.12)$$

In the case when connector yielding is not ensured (for example, in concrete topping), the following equation is presented (Eq. 1.13):

$$\tau_{Rdi} = c_v \sqrt{f_c} + \mu_v \sigma_n + k_v \rho f_y \mu_v + k_{dowel} \rho \sqrt{f_y f_c}, \quad (1.13)$$

here, c_v – cohesion coefficient, μ_v – friction coefficient, k_v and k_{dowel} – coefficients controlling contributions of different shear mechanisms. Presented shear mechanisms: $c_v \sqrt{f_c}$ – adhesion and interlock, $\mu_v \sigma_n$ – friction due to compressive stress, $\rho f_y (\mu_v \sin\alpha + \cos\alpha)$ – friction due to connector clamping, and $k_{dowel} \rho \sqrt{f_y f_c}$ – dowel action.

Comparing the interface models presented in Eurocode and Model Code, it can be stated that in the first-generation Eurocode 2, the interface shear resistance is calculated as a direct superposition of different shear mechanisms, without applying specific coefficients to reduce or amplify individual contributions. This approach differs from that of the second-generation Eurocode 2, where, for example, the coefficient c_v for a smooth interface between a precast element and a concrete topping is taken as zero. Likewise, Model Code 2020 does not specify a value or coefficient for τ_c for a smooth interface. The absence of these values indicates the insignificance of adhesion in smooth interfaces, opposite to rough interfaces. In the second-generation Eurocode 2, dowel action appears only in the equation governing smooth interfaces, while the clamping stress contribution is reduced using the coefficient $k_v = 0.5$. According to Model Code 2020, the interrelation between clamping and dowel action should be considered by coefficients $\kappa_1 = 0$ and $\kappa_2 = 1.6$ for smooth interfaces and $\kappa_1 = 1.0$ and $\kappa_2 = 0$ for rough interfaces. These values in both the second-generation Eurocode 2 and Model Code 2020 clearly indicate that, after adhesion failure, dowel action becomes the dominant shear mechanism in smooth interfaces, whereas clamping action dominates in rough interfaces.

After reviewing the existing interface behaviour models, it becomes evident that most focus solely on predicting the maximum interface shear resistance, while neglecting the behaviour at other stages of interface deformation. Some models address only the adhesion-dominated stage, whereas others omit adhesion entirely and consider only friction-based mechanisms. Several models treat the total shear resistance as a simple superposition of the peak contributions from different shear mechanisms, even though these mechanisms reach their maximum resistance at different slip levels.

1.2.2. Interface Shear Stiffness Models

The analytical interface behaviour models presented in Section 1.2.1 focus primarily on determining interface shear resistance. Indeed, most models in the literature are concerned only with the ultimate shear resistance of the interface. In this dissertation, however, the emphasis is placed on interface stiffness, which describes not only shear resistance but also the associated shear deformation (slip). Models that describe this combined behaviour are scarce, particularly for concrete-to-concrete interfaces. The following section, therefore, reviews the limited available models that relate shear stress to slip.

The first model presented here was introduced by Yang (2016). It describes the relationship between interface shear stress and slip for smooth concrete interfaces. According to the model, slip initiates once the interface begins to crack at

shear stress τ_{cr} . Shear stress then increases until it reaches the peak value τ_n at a corresponding slip S_0 , after which it decreases as the interface exhausts its shear resistance (Fig. 1.6). The expressions for the initial cracking stress τ_{cr} (Eq. 1.14) and the peak-slip S_0 (Eq. 1.16) were obtained through nonlinear regression analysis of push-off test data, while the equation for the peak shear resistance τ_n (Eq. 1.15) is derived from the upper-bound theorem of concrete plasticity. A notable strength of this model is its inclusion of interface-connector inclination relative to the interface plane in Eq. 1.15.

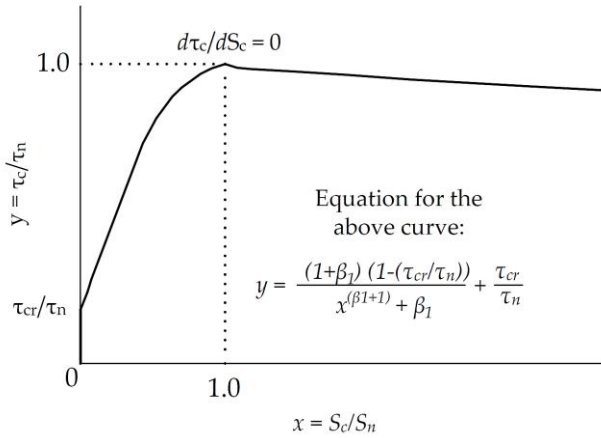


Fig. 1.6. Smooth concrete interface shear stress – slip relationship (Yang, 2016)

$$\tau_{cr} = 2.38 \frac{\sigma_x}{\sqrt{f'_c}} + 0.22 \sqrt{f'_c}, \tag{1.14}$$

$$\tau_n = 0.11 (f'_c)^{0.65} + \rho_{vf} f_y \frac{\cos(\theta_s - 32.8^\circ)}{\cos(32.8^\circ)} + \sigma_x \tan(32.8^\circ), \tag{1.15}$$

$$S_0 = 0.39 \left(\frac{\sigma_{eq}}{\sqrt{f'_c}} \right)^{0.30}, \tag{1.16}$$

$$\sigma_{eq} = \rho_{vf} f_y + \sigma_x. \tag{1.17}$$

Shear stress at any value of S (Eq. 1.18):

$$\tau(S) = \frac{\left(1 - \frac{\tau_{cr}}{\tau_n}\right)(\beta_1 + 1)S}{S^{\beta_1 + 1} + \beta_1} + \frac{\tau_{cr}}{\tau_n}. \tag{1.18}$$

When $S_c \leq S_0$:

$$\beta_1 = 0.024\sigma_{eq} + 0.73. \tag{1.19}$$

When $S_c > S_0$:

$$\beta_1 = 1.54\sigma_{eq}^{-0.90}, \tag{1.20}$$

here, σ_x – stress from external perpendicular compression, f'_c – concrete compressive strength, ρ_{vf} – connector ratio, f_y – connector yield stress, σ_{eq} – equivalent normal interface stress, β_1 – coefficient used for determining shear stress at different interface deformation stages, and θ_s – inclination of interface connectors.

Xu et al. (2015) developed a shear stress–slip relationship model for monolithic concrete interfaces. The resulting shear stress–slip curve is shown in Figure 1.7. The model equations were derived from Mohr–Coulomb failure theory together with regression analysis of experimental data. In this model, slip initiates once shear stress begins to increase, and the shear stress continues to rise until it reaches its maximum value τ_{max} (Eq. 1.21), corresponding to a slip of Δ_1 (Eq. 1.22). After this point, the interface transitions into subsequent phases of shear behaviour (Fig. 1.7). The model is applicable within the following limits: $f'_c \leq 65\text{ MPa}$; $\sigma_x + \rho_{vf}f_y \leq 0.25f'_c$.

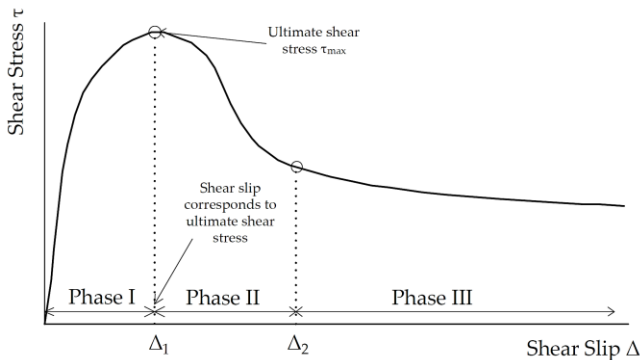


Fig. 1.7. Monolithic concrete interface shear stress – slip relationship (Xu et al., 2015)

$$\tau_{max} = (-0.038f_c'^{0.21})(\rho f_y + \sigma_n)^2 + 0.33f_c'^{0.5}(\rho f_y + \sigma_n) + 0.3f_c'^{0.75}, \quad (1.21)$$

$$\Delta_1 = (-0.011f_c' + 1.72)e^{10^{-16}f_c' + 0.084(\rho f_y + \sigma_n)}. \quad (1.22)$$

Shear stress when the slip is equal to $\Delta < \Delta_1$ (Eq. 1.23):

$$\tau(\Delta) = \tau_{max} \cos\left(\frac{\pi}{2} \frac{\Delta - \Delta_1}{\Delta_1}\right). \quad (1.23)$$

Shear stress when the slip is equal to $\Delta_1 < \Delta < \Delta_2$ (Eq. 1.24):

$$\tau(\Delta) = \tau_{max} \cos\left(-\frac{\pi}{2} 0.6 \frac{\Delta - \Delta_1}{\Delta_1}\right) + 0.01\tau_{max} \sin\left(0.125\pi \frac{\Delta - \Delta_1}{\Delta_1}\right), \quad (1.24)$$

$$\Delta_2 = 1.8\Delta_1. \quad (1.25)$$

Shear stress when the slip is equal to $\Delta > \Delta_2$ (Eq. 1.26):

$$\tau(\Delta) = \tau_2 \left(\frac{\Delta}{\Delta_2}\right)^{-0.38}, \quad (1.26)$$

$$\tau_2 = \tau_{max} \cos\left(-\frac{\pi}{2} 0.6 \frac{\Delta_2 - \Delta_1}{\Delta_1}\right) + 0.01\tau_{max} \sin\left(0.125\pi \frac{\Delta_2 - \Delta_1}{\Delta_1}\right), \quad (1.27)$$

here, f_c' – concrete compressive strength, ρ – connector ratio, f_y – connector yield stress, σ_n – lateral normal pressure, τ_{max} – ultimate shear stress, τ_2 – shear stress at the beginning of the plastic interface behaviour stage, Δ – interface slip, Δ_1 – slip at the point of ultimate shear stress, and Δ_2 – slip at the beginning of the plastic interface behaviour stage.

Model Code 90 (Committee for the Model Code 1990, 1993) presented shear stress–slip relationships for both smooth and rough interfaces. For smooth interfaces, the Code recommends a relatively simple expression that defines the friction-based shear resistance (Eq. 1.28) and the corresponding slip (Eq. 1.29).

$$\tau_{fu} = 0.4\sigma_c, \quad (1.28)$$

$$s_u = 0.15\sqrt{\sigma_c}, \quad (1.29)$$

here, τ_{fu} – interface shear resistance, s_u – shear slip at interface failure (in mm), and σ_c – normal compressive stress at the interface due to external force and clamping (in MPa).

For rough interfaces, a more detailed model is recommended (Fig. 1.8). The model assumes that cracking initiates when the interface reaches 50% of its total shear resistance. The corresponding slip at this stage is taken as 0.10 mm, which represents 5% of the maximum interface slip. Beyond this point, the interface enters a ductile behaviour stage. The subsequent response in this stage is described by the equations provided in Eqs. 1.30, 1.31, and 1.33.

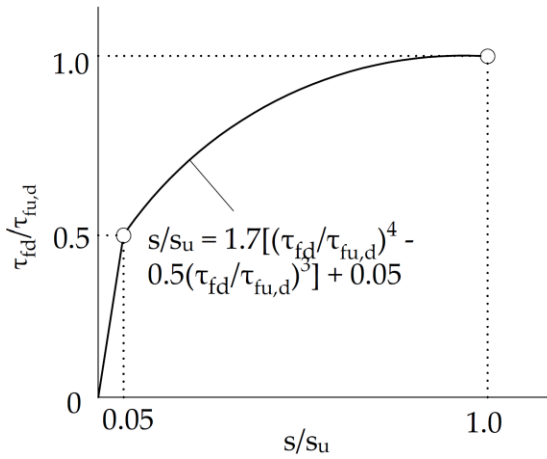


Fig. 1.8. Rough concrete interface shear stress – slip relationship (Committee for the Model Code 1990, 1993)

$$\tau_{fu} = 0.40 f_c^{\frac{2}{3}} (\sigma_c + \rho f_y)^{\frac{1}{3}}, \tag{1.30}$$

$$s_u = 2 \text{ mm}. \tag{1.31}$$

When $s \leq 0.10$ mm:

$$\tau_f = 5\tau_{fu}s. \tag{1.32}$$

When $s > 0.10$ mm:

$$\left(\frac{\tau_f}{\tau_{fu}}\right)^4 - 0.5\left(\frac{\tau_f}{\tau_{fu}}\right)^3 = 0.3s - 0.03, \tag{1.33}$$

here, τ_{fu} – interface shear (friction) resistance, f_c – concrete compressive strength, ρ – interface connector ratio, f_y – interface connector yield stress, τ_f – shear stress at any value of interface slip, s – interface slip, and s_u – ultimate slip, at which the highest shear resistance is achieved.

The presented shear stress–slip relationship models describe interface behaviour in greater detail than models concerned solely with maximum shear resistance. By capturing the relationship between shear stress and slip, these models allow the interface shear stiffness to be evaluated across different stages of interface behaviour. However, models of this type for smooth concrete-to-concrete interfaces remain limited in the literature. Additionally, none of the available models accounts for the effects of differential shrinkage, which must be considered when analysing interface behaviour. The following chapter, therefore, introduces a novel interface shear stress–slip (shear stiffness) model developed by the author.

1.3. Engineering Characteristics and Review of Experimental Studies of Layered Concrete Elements Under Bending

1.3.1. Types and Characteristics of Layered Concrete Elements

Layered concrete elements are structural elements composed of at least two concrete layers, typically subjected to bending. The layers are cast at different times and, therefore, exhibit distinct material properties, including differences in mechanical characteristics, differential shrinkage and more (Figueira et al., 2016; Hillebrand & Hegger, 2023; Lampropoulos et al., 2014; Li et al., 2021). In most cases, the first layer is a precast concrete element, while the second layer is cast in place.

Filigree slabs, also referred to as semi-precast slabs, are a common example of layered concrete elements subjected to bending. They consist of two layers: a thin precast concrete base slab, typically 50–70 mm thick, and an additional cast-in-place concrete layer of variable thickness. The layers are connected by lattice girders embedded in the precast element (Cao et al., 2024; Hillebrand et al., 2021; Newell & Goggins, 2019), as shown in Figure 1.9. This system eliminates the need for formwork, accelerating construction, can be combined with other structural elements such as balconies, or forming a continuous slab (Fédération Internationale de la Précontrainte, 1998; Hillebrand & Hegger, 2023). In addition, the precast-in-situ configuration allows for the formation of voids within the slab.

Plastic void formers (Molkens & Van Gysel, 2021; Sagadevan & Rao, 2019)(Fig. 1.10), polystyrene blocks (Ingeli et al., 2025; Ling et al., 2024; Stehle et al., 2011) or other lightweight materials may be used. Forming voids reduces concrete consumption and, consequently, the amount of cement required, lowering CO₂ emissions associated with cement production (Andrew, 2019; Cheng et al., 2023; Paik et al., 2019; Shah et al., 2022; Volaity et al., 2025). Void formers can also be manufactured from recycled materials (Khouzani et al., 2021; Valivonis et al., 2015). Structurally, reducing the concrete volume decreases the self-weight of the slab without significantly affecting its flexural capacity, as voids are typically formed near the neutral axis of the cross-section. This enables longer spans and may reduce the required amount of flexural reinforcement.

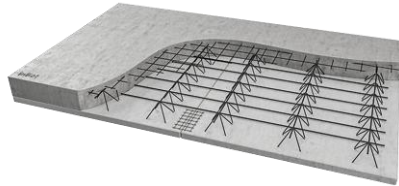


Fig. 1.9. Semi-precast (filigree) slab (InBet Sp. z o.o, n.d.)



Fig. 1.10. Semi-precast (filigree) slab with plastic void formers (Evan Bond, 2016)

A second type of layered concrete element consists of a precast concrete beam with an additional cast-in-place concrete layer (Hossain et al., 2020; Ji & Liu, 2020; Wang et al., 2021; W. Zhang, Lin, et al., 2024; W. Zhang, Zhang, et al., 2024; W. Zhang, Zheng, et al., 2024). The added layer may connect the precast beam to a larger continuous system, as shown in Figure 1.11, or modify the beam's cross-section by introducing concrete of different properties, as shown in Figure 1.12. This solution is used to achieve stiffer behaviour between beams and the slabs they support (Fig. 1.11), to form a continuous layered slab, to intentionally

adjust beam cross-sectional properties (Fig. 1.12), to accommodate multi-stage casting, and to simplify structural assembly. A typical application is a concrete bridge girder with a cast-in-place concrete deck (Fasching et al., 2021; Haber et al., 2020; Jung et al., 2024; Sasaki et al., 2010) (Fig. 1.13).

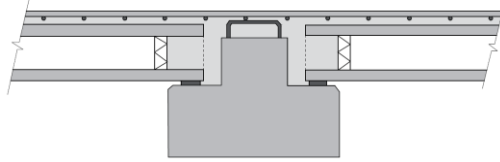


Fig. 1.11. Precast beam–slab structural system

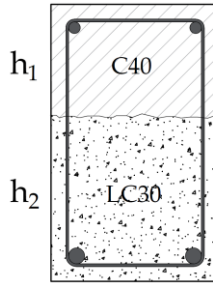


Fig. 1.12. Concrete beam with varying layer properties



Fig. 1.13. Layered precast concrete girder–concrete deck structural system

The final type of layered concrete structural element is the block-and-beam slab system (Sousa & Miguel De Sousa, 2019), as shown in Figure 1.14. This slab consists of concrete beams (ribs) with widths of approximately 100 mm or more. Interface connectors may extend from the beams. Concrete blocks are placed between the ribs; their cross-sections may include voids to reduce self-weight. Block dimensions depend on the beam spacing. After assembly, a cast-in-place concrete layer is added to form the completed slab. This system offers practical

advantages, such as easy installation without heavy lifting equipment due to the small size of individual components. As a result, block-and-beam slabs can be installed in existing buildings, and overall construction speed is increased. Despite the structural differences between the various layered concrete elements described, they all share a common mechanical feature: the interface between the pre-cast components and the newly cast layer exhibits only partial shear connection.

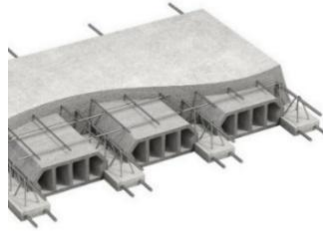


Fig. 1.14. Layered concrete block-beam structural system (Universal Slab, 2024)

1.3.2. Review of Experimental Studies of Layered Concrete Elements

Ibrahim (2019) conducted experimental tests on four one-way concrete slab types: a solid slab (SS), a slab with void formers (BS), a filigree slab with void formers (F.BS), and a filigree slab with void formers and interface connectors (F.BS.S). The experimental setup of the layered slab is presented in Figure 1.15.

Experimental results shown in Figure 1.16 indicate that three slabs, SS, BS, and F.BS.S, reached similar ultimate resistance values: 115 kN for SS, 110 kN for BS, and 113 kN for F.BS.S. Although the slabs incorporating void formers exhibited slightly lower capacity (1.7–4.4%), the results clearly demonstrate that removing concrete from the neutral bending zone does not substantially reduce flexural capacity. However, the reduced stiffness of the void-former slabs increased the yield deflection: 11.6 mm for SS, 13.0 mm for BS, and 12.8 mm for F.BS.S. These slabs failed in a flexural mode. In contrast, slab F.BS failed due to interface shear failure. It reached a significantly lower ultimate resistance of 35 kN and an ultimate deflection of 9.39 mm. As layer slip progressed, the initially composite behaviour gradually transitioned toward that of two independent layers. These findings show that layered concrete structural elements are particularly susceptible to interface shear failure. Nevertheless, introducing interface connectors in F.BS.S restored composite action, resulting in a flexural (and more ductile) failure mode and an ultimate capacity comparable to that of the solid slab.

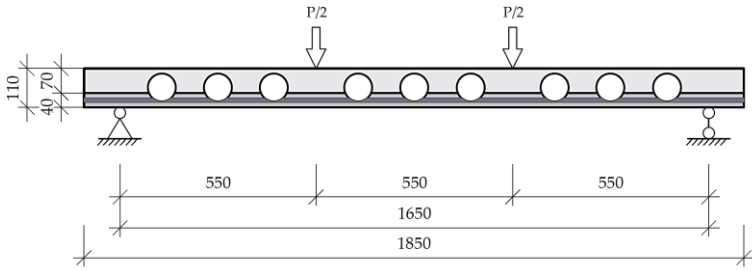


Fig. 1.15. Experimental test arrangement of layered specimen (M. Ibrahim, 2019)

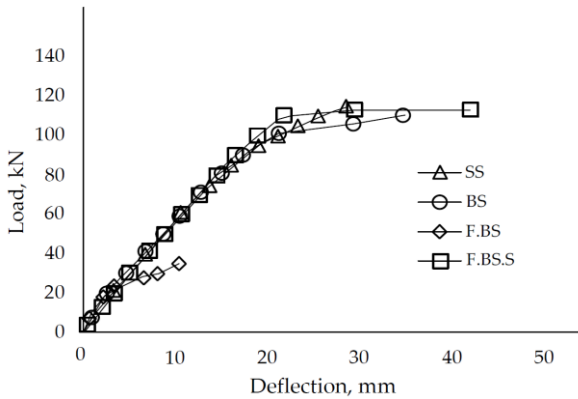


Fig. 1.16. Experimental load-deflection diagrams (M. Ibrahim, 2019)

Mohamed et al. (2020) conducted experimental tests on five one-way layered concrete slabs. Unlike the previous study, these specimens did not incorporate void formers. The first slab (S1) was a precast element without an added concrete layer. Its results showed markedly lower flexural capacity and deflection due to early failure, which is attributable to its significantly smaller cross-sectional height. Because S1 behaved substantially worse than the remaining slabs and does not represent a layered element, it is excluded from further discussion. The remaining four specimens were layered slabs. The first layer thickness was equal to the thickness of slab S1. After 14 days, the second layer was added. The interface conditions varied: S2 had an untreated left-as-casted surface, S3 had a deliberately roughened surface, S4 used an acrylic-based polymer bonding agent, and S5 incorporated steel shear keys. The compressive strengths of slab layers are provided in Table 1.1. Flexural reinforcement consisted of 12 mm bars. The slabs were tested under a four-point bending arrangement, shown in Figure 1.17.

Table 1.1. Concrete characteristics of experimental slabs

Slab	S2	S3	S4	S5
Concrete compressive strength of first layer, MPa	29.4	30.1	31.4	33.2
Concrete compressive strength of second layer, MPa	24.9	23.4	28.4	28.2

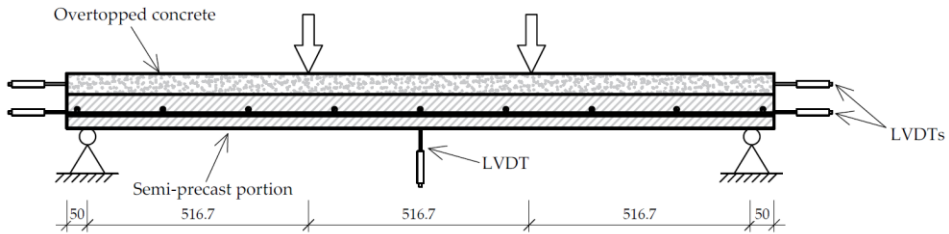


Fig. 1.17. Experimental specimen test arrangement (Mohamed et al., 2020)

S2 exhibited an interface debonding failure mode, reaching a maximum interface slip of 4.8 mm. The remaining slabs failed through flexural cracking and concrete crushing, typical failure modes of solid cross-section elements. The cracking pattern of S2 is shown in Figure 1.18. A comparison of all specimens indicates that appropriate interface surface treatment can enable a layered slab to perform similarly to a solid cross-section slab.

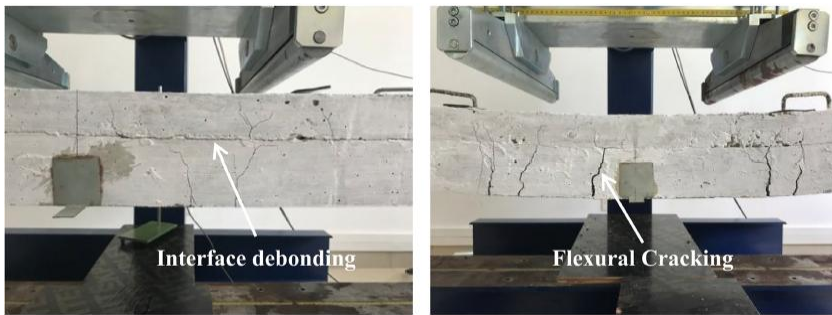


Fig. 1.18. Two types of slab failure modes (Mohamed et al., 2020)

Load–deflection curves in Figure 1.19 show that specimen S2 behaved similarly to the other slabs within the elastic stage. However, once its interface shear capacity was exceeded, the deflection increased rapidly, with the load at that point being 64% of the S5 capacity (43.5 kN). At this stage, interface slips and

deflection increased. The behaviour of the remaining slabs demonstrates that appropriate interface surface treatment can significantly enhance flexural capacity by ensuring full composite action. Among the treated specimens, S5 achieved the highest flexural resistance (68 kN), followed by S4 (64 kN) and S3 (63 kN). Although shear keys appeared to be the most effective solution, the slightly higher concrete strength of S5 (and S4) likely contributed to their increased capacities.

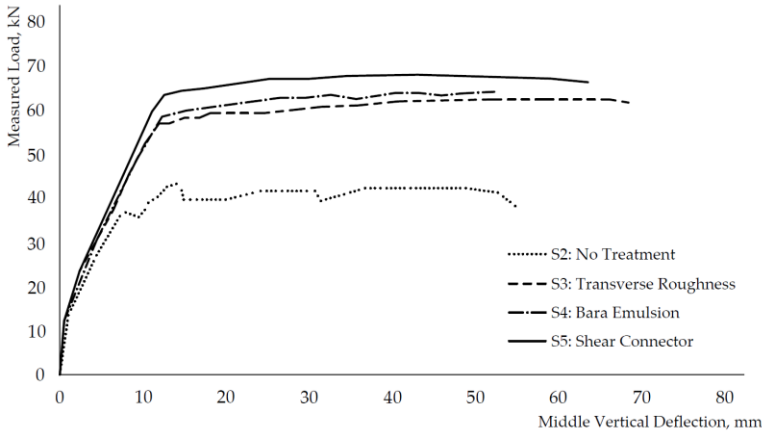


Fig. 1.19. Experimental load–deflection diagrams (Mohamed et al., 2020)

Ji and Liu (2020) conducted experimental tests on five beams. One beam had a solid concrete cross-section, while the remaining four were layered beams composed of the same concrete section supplemented with an ultra-high-performance fibre-reinforced concrete (UHPFRC) layer at the bottom. The solid beam (RC-2.7) had a height of 500 mm, whereas the layered beams had a total height of 550 mm (500 mm concrete + 50 mm UHPFRC). The specimens were identified as RC-2.7, RC-U-2.7, RC-RU-2.4, RC-RU-2.7 and RC-RU-3.1, where “R” denotes reinforcement in the UHPFRC layer, “C” denotes the concrete section, “U” denotes the UHPFRC layer, and the final number indicates the span. The cross-sections are shown in Figure 1.20. A three-point bending test setup was used. Table 1.2 presents the measured shear resistance values for all beams.

Table 1.2. Load capacities of experimental beams

Specimen	RC-2.7	RC-U-2.7	RC-RU-2.4	RC-RU-2.7	RC-RU-3.1
Shear capacity, kN	655	717	955	922	761

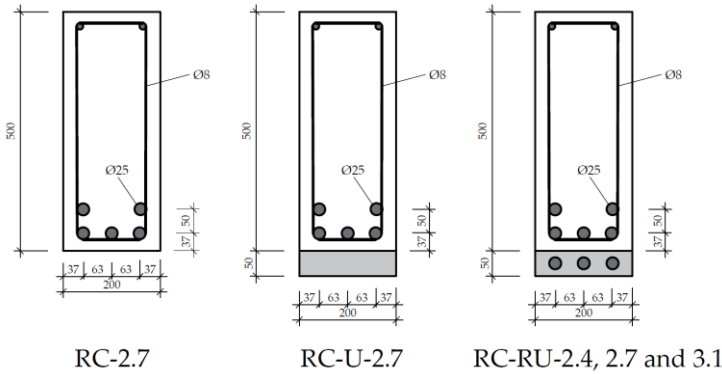


Fig. 1.20. Experimental beam specimen cross-sections (Ji & Liu, 2020)

The experimental results demonstrate that the addition of a UHPFRC layer significantly increases the beam’s capacity, as it not only raises the effective cross-sectional height but also enhances tensile performance. The inclusion of reinforcement within the UHPFRC layer further improves the load-bearing capacity. However, in comparison with specimen RC-U-2.7, this additional reinforcement reduces the ductility of beam failure (Fig. 1.21).

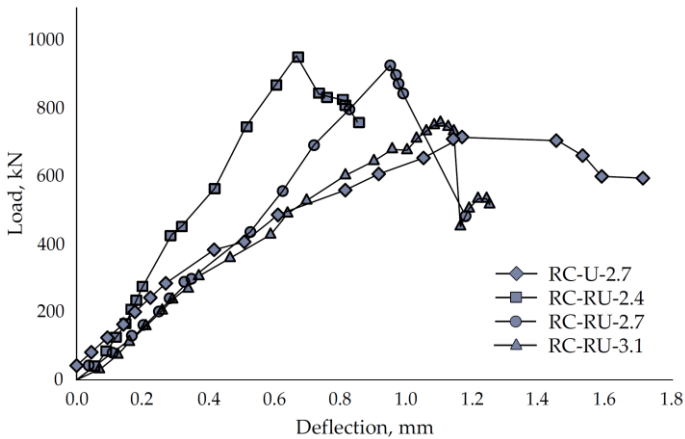


Fig. 1.21. Load–deflection curves of experimental beams (Ji & Liu, 2020)

The failure patterns of the beams are shown in Figure 1.22, where the cracking behaviour of the solid cross-section beam and two-layered beams is illustrated. The solid beam failed in a typical shear failure mode, whereas the layered beams exhibited a more complex failure. As the load increased, the number of

flexural cracks grew until diagonal cracks began to propagate toward the loading point. Once these diagonal cracks reached approximately mid-height of the section, flexural cracks initiated in the UHPFRC layer. With further loading, cracks in the concrete layer widened and extended, while the number of UHPFRC cracks increased. High shear stresses and diagonal cracking subsequently led to interface debonding at the point where the diagonal cracks initiated. This debonding was followed by the development of large cracks in the UHPFRC layer described by Ji and Liu as “hinges”, which marked the failure of the layered beam.

This represents one possible failure pattern of a layered concrete beam. In other cases, the first cracks may form in the bottom layer, or the interface may fail before any flexural cracks develop. These variations highlight the complexity of analysing layered concrete elements.

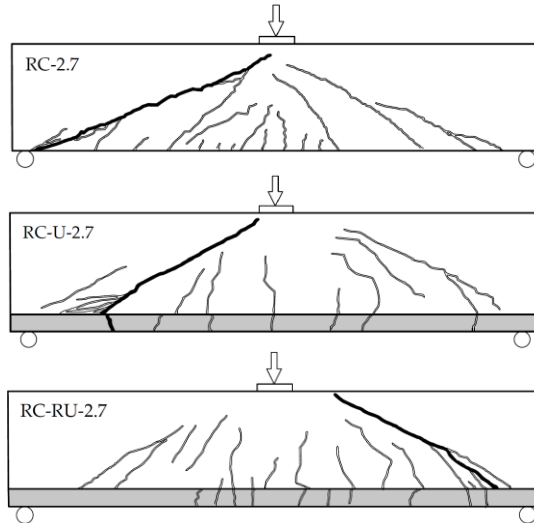


Fig. 1.22. Experimental beam cracking patterns (Ji & Liu, 2020)

Differential shrinkage is an important aspect of layered concrete element behaviour. It arises when the concrete layers are cast at different times or produced using different mixes, causing each layer to shrink at a different rate. The first layer completes most of its shrinkage before the second layer is cast, while the newly placed layer undergoes its initial, larger shrinkage deformation. Because the layers are bonded, this difference in deformation induces additional shear stresses at the interface. These stresses can substantially reduce the interface shear resistance and make the interface more susceptible to failure.

Lampropoulos et al. (2014) and Tsioulou et al. (2013) conducted experimental tests on layered concrete beams with explicit consideration of differential shrinkage. Three beam types were examined. The first type, O_1 , was a solid cross-

section beam with dimensions $250 \text{ mm} \times 150 \text{ mm} \times 2200 \text{ mm}$. The second type, T_1 , was a layered beam consisting of a first concrete layer identical to O_1 and an additional 50-mm concrete layer cast on the tensile side. The added layer was reinforced with $2\emptyset 12$ bars. The third type, MT_1 , was a solid cross-section beam with the same overall dimensions and reinforcement layout as the layered beam. For the differential shrinkage analysis, a concrete specimen matching the dimensions of the second layer in beam T_1 was cast separately. This specimen was used to measure the free shrinkage of the new concrete. Shrinkage was also recorded directly in the newly cast layer of the layered beams. The measured shrinkage values are presented in Figure 1.23.

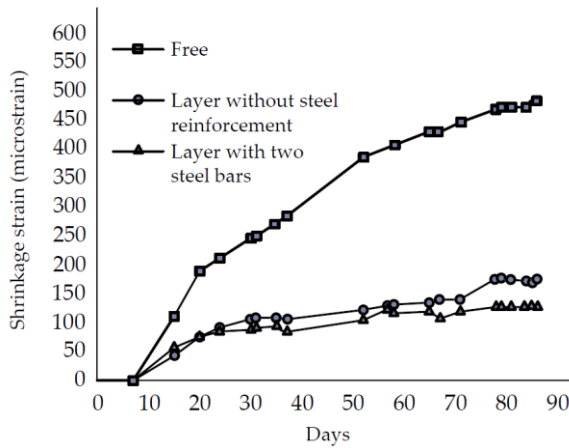


Fig. 1.23. Concrete shrinkage values in different concrete layers (Lampropoulos et al., 2014)

Free shrinkage of the 50 mm concrete element reached $480 \mu\epsilon$. In contrast, the concrete layer of the same thickness within the layered beams developed significantly lower shrinkage strains. This reduction resulted from the restraint provided by the hardened first concrete layer. The effect was even more pronounced in the reinforced second layer, where the steel bars introduced additional restraint. Shrinkage restriction increases shear stresses along the interface between the layers.

Flexural test results were used to assess the influence of differential shrinkage-induced interface stresses. Four-point bending tests were performed. As shown in Figure 1.24, beam O_1 failed at the lowest load of 78 kN due to its smaller cross-sectional height and lower reinforcement ratio. Beam T_1 , which incorporated an additional tensile-side layer, reached a substantially higher capacity of 167 kN, indicating that the second layer and its reinforcement markedly increased

structural performance. The highest capacity, 182 kN, was recorded for beam MT_1 , which had the same geometry and reinforcement layout as T_1 but without an interface. MT_1 also exhibited greater deformability, reaching a higher ultimate deflection. In contrast, beam T_1 demonstrated a more brittle failure. The reduced capacity and brittle failure of T_1 are attributed, at least in part, to interface shear stresses induced by differential shrinkage.

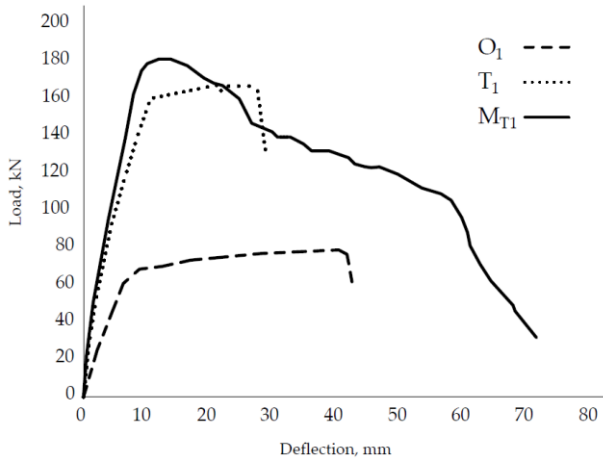


Fig. 1.24. Load–deflection curves of experimental beams (Tsioulou et al., 2013)

1.4. Methods for Calculating Flexural Stiffness of Layered Concrete Elements with Partial Shear Connection Interfaces

1.4.1. Magnucki et al. Model

Magnucki et al. (2020) proposed an analytical method for determining the flexural stiffness of layered concrete elements. The method is based on the nonlinear deformation hypothesis for planar cross-sections, the derivation and solution of the corresponding equilibrium equations. The model does not consider a slip between the layers; however, the distribution of stress at the composite section varies according to the properties of each layer. The theoretical cross-section used in the model is shown in Figure 1.25.

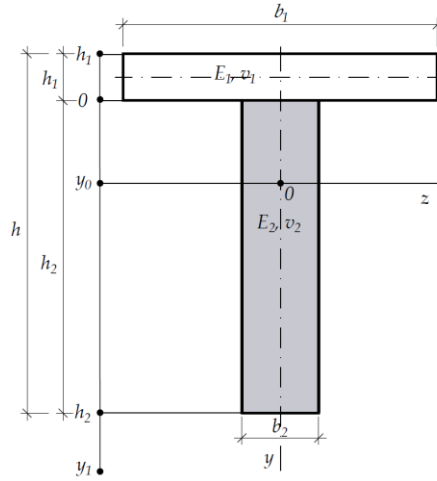


Fig. 1.25. Theoretical layered element cross-section (Magnucki et al., 2020)

Maximum deflection of the layered element is calculated as follows (Eq. 1.34):

$$v_a = L v_a, \tag{1.34}$$

here, L – the length of the layered element and v_a – relative maximum deflection. The latter value is determined accordingly (Eq. 1.35):

$$v_a = \frac{4}{\pi^5} \lambda^3 \beta_1 \overline{v_a} \frac{q}{E_2 b_1}, \tag{1.35}$$

here, $\lambda = \frac{L}{h}$ – relative length of the element, q – value of uniformly distributed load, E_1 and E_2 – elastic moduli of upper and lower concrete layers, respectively, b_1 and b_2 – widths of upper and lower layers, respectively, and $\beta_1 = \frac{b_1}{b_2}$, the value of $\overline{v_a}$ is determined as follows (Eq. 1.36):

$$\overline{v_a} = \frac{det_v}{det_0}. \tag{1.36}$$

Determinants are calculated accordingly (Eqs. 1.37–1.40):

$$det_v = \alpha_{u1}\alpha_{u2} - C_{u1u2}^2, \quad (1.37)$$

$$det_0 = C_{vv}\alpha_{u1}\alpha_{u2} + 2C_{vu1}C_{vu2}C_{u1u2} - (C_{vu2}^2\alpha_{u1} + C_{vu1}^2\alpha_{u2} + C_{u1u2}^2C_{vv}), \quad (1.38)$$

$$\alpha_{u1} = C_{u1u1} + \frac{\lambda^2}{\pi^2}C_{u10}, \quad (1.39)$$

$$\alpha_{u2} = C_{u2u2} + \frac{\lambda^2}{\pi^2}C_{u20}. \quad (1.40)$$

Coefficients, taken from the bending moment differential equation (Eqs. 1.41–1.43):

$$C_{vv} = \frac{1}{3} \left[(1 + 3\eta_{01} + 3\eta_{01}^2) e_1 \beta_1 \chi_1^3 + (1 + 3\eta_{02} + 3\eta_{02}^2) \chi_2^3 \right], \quad (1.41)$$

$$C_{vu1} = \frac{8 + 25\eta_{01} + 20\eta_{01}^2}{10(2 + 3\eta_{01})} e_1 \beta_1 \chi_1^2, \quad (1.42)$$

$$C_{vu2} = \frac{8 - 25\eta_{02} + 20\eta_{02}^2}{10(2 + 3\eta_{02})} \chi_2^2 - \frac{1}{2} \left[(1 + 2\eta_{02}) \chi_2^2 - (1 + 2\eta_{01}) e_1 \beta_1 \chi_1^2 \right] f_{d0}^{(2)}. \quad (1.43)$$

Coefficients, taken from the beam equilibrium differential equations, based on a rule of stationary total potential energy (Eqs. 1.44–1.48):

$$C_{u1u1} = \frac{136 + 427\eta_{01} + 336\eta_{01}^2}{70(2 + 3\eta_{01})^2} e_1 \beta_1 \chi_1^2, \quad (1.44)$$

$$C_{u1u2} = \frac{5 + 8\eta_{01}}{4(2 + 3\eta_{01})} e_1 \beta_1 \chi_1^2, \quad (1.45)$$

$$C_{u10} = \frac{3}{1 + \nu_1} \frac{8 + 25\eta_{01} + 20\eta_{01}^2}{10(2 + 3\eta_{01})^2} \frac{e_1 \beta_1}{\chi_1}, \quad (1.46)$$

$$C_{u20} = \frac{3}{1 + \nu_2} \frac{8 - 25\eta_{02} + 20\eta_{02}^2}{10(2 + 3\eta_{02})^2} \frac{1}{\chi_2}, \quad (1.47)$$

$$C_{u2u2} = \left[\frac{136 - 427\eta_{02} + 336\eta_{02}^2}{70(2 - 3\eta_{02})^2} - \frac{5 - 8\eta_{02}}{2(2 - 3\eta_{02})} f_{d0}^{(2)} \right] \chi_2 + (e_1 \beta_1 \chi_1^2) (f_{d0}^{(2)})^2. \quad (1.48)$$

Dimensionless parameters are determined as follows (Eqs. 1.49–1.53):

$$\eta_{01} = \frac{y_0}{h_1}, \quad (1.49)$$

$$\eta_{02} = \frac{y_0}{h_2}, \quad (1.50)$$

$$e_1 = \frac{E_1}{E_2}, \quad (1.51)$$

$$\beta_1 = \frac{b_1}{b_2}, \quad (1.52)$$

$$\chi_1 = \frac{h_1}{h}, \quad (1.53)$$

here, y_0 – distance from the interface to the neutral axis of the layered element and h_1 and h_2 – height of the upper and lower layers, respectively. Function, describing deformation of the lower layer (Eqs. 1.54, 1.55):

$$f_d^2(y_0) = f_{d0}^{(2)}, \quad (1.54)$$

$$f_d^2(y_0) = \frac{3 - 6\eta_{02} + 2\eta_{02}^2}{2 - 3\eta_{02}} \eta_{02}. \quad (1.55)$$

1.4.2. Foraboschi Model

Foraboschi (2009) developed a nonlinear analytical model for the behaviour of two-layer concrete elements subjected to bending. The model incorporates the slip between layers and represents the interface as an elastic-plastic, strain-softening element. It allows prediction of internal stresses and the load at which debonding initiates. The theoretical loading arrangement of the layered element is shown in Figure 1.26.

According to this method, the behaviour of a layered element subjected to bending is governed by the behaviour of the interface. The horizontal displacements of the upper and lower layers are denoted as z_A and z_B . The theoretical layer slip mechanism is shown in Figure 1.27. From this derives an interface slip expression (Eq. 1.56):

$$\xi = z_B - z_A. \tag{1.56}$$

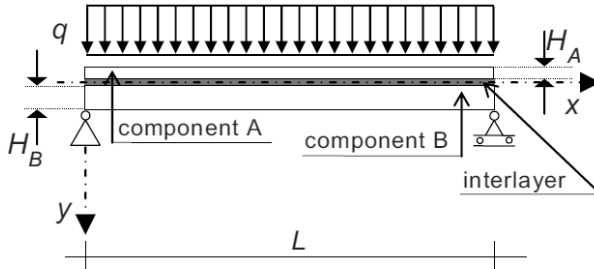


Fig. 1.26. Theoretical layered element loading arrangement (Foraboschi, 2009)

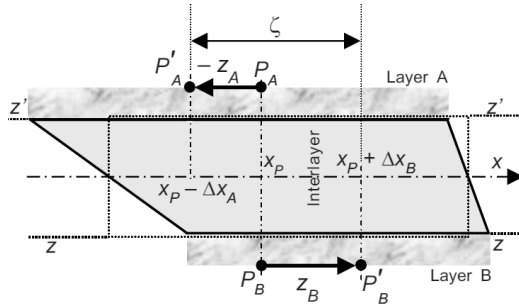


Fig. 1.27. Theoretical layered element loading arrangement (Foraboschi, 2009)

From this expression, two differential equations are formulated (Eqs. 1.57, 1.58):

$$\frac{d\xi}{dx} = \frac{dz_B}{dx} - \frac{dz_A}{dx}, \tag{1.57}$$

$$\frac{d^2\xi}{dx^2} = \frac{d^2z_B}{dx^2} - \frac{d^2z_A}{dx^2}. \tag{1.58}$$

Derivative of z relates to layer strain at the fibre, closest to the interface, as follows (Eqs. 1.59, 1.60):

$$\varepsilon_{iA} = \frac{dz_A}{dx}, \tag{1.59}$$

$$\varepsilon_{iB} = \frac{dz_B}{dx}. \tag{1.60}$$

The deformation state, internal forces and moments of the layered element are depicted in Figure 1.28. The latter two expressions can be moved to the second-order differential equation in Eq. 1.61:

$$\frac{d^2 \xi}{dx^2} = \frac{d\varepsilon_{iA}}{dx} - \frac{d\varepsilon_{iB}}{dx}. \tag{1.61}$$

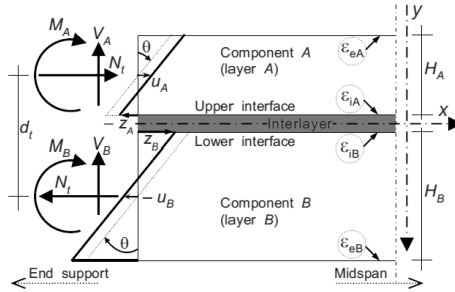


Fig. 1.28. Deformation, forces, and moments in layers of a layered element (Foraboschi, 2009)

The relationship between internal strains ε_i and layer axial forces and bending moments (Eqs. 1.62–1.65):

$$d\varepsilon_{iA-M} = \frac{dM_A}{E_A W_A}, \tag{1.62}$$

$$d\varepsilon_{iA-N} = -\frac{dN_t}{E_A A_A}, \tag{1.63}$$

$$d\varepsilon_{iB-M} = -\frac{dM_B}{E_B W_B}, \tag{1.64}$$

$$d\varepsilon_{iB-N} = \frac{dN_t}{E_B A_B}, \tag{1.65}$$

here, M and N – bending moment and axial force of the layer, respectively, E – elastic modulus of the layer, A – layer cross-section area, and W – layer cross-

section modulus. Using previous expressions, a relationship between interface slip and layer internal forces can be written (Eq. 1.66):

$$\frac{d^2\xi}{dx^2} = -\frac{dM_B}{E_B W_B} + \frac{dN_t}{E_B A_B} - \frac{dM_A}{E_A W_A} + \frac{dN_t}{E_A A_A}. \quad (1.66)$$

The bending stiffness of the individual layer and the layered element, respectively (Eqs. 1.67, 1.68):

$$\rho_B = \frac{E_B J_B}{E_A J_A + E_B J_B}, \quad (1.67)$$

$$\rho_B = \frac{E_A J_A}{E_B J_B}, \quad (1.68)$$

here, J – the second moment of area of the layer. When the shear component is negligible compared to the flexural component, it is assumed that the bending moment is proportional to the bending stiffness. Ultimately, a final form of layer slip, layered element stiffness and applied load relationship is presented (Eq. 1.69):

$$\frac{d^2\xi}{dx^2} = -\left(\frac{J_A}{E_B J_B W_A} + \frac{1}{E_B W_B}\right) \frac{dM_B}{E_B W_B} + \left(\frac{1}{E_A A_A} + \frac{1}{E_B A_B}\right) D\tau_i, \quad (1.69)$$

here, D – interface width and τ_i – interface shear stress. When the shear component in bending has to be considered, mostly in a composite element with significantly different (in terms of geometry or materials) layers, vertical deformation must be determined. Curvatures of each layer are equal along the beam length. The curvature of the layer is calculated as follows (Eq. 1.70):

$$\frac{1}{r_A} = -\frac{M_A}{E_A J_A} + \frac{\chi_A}{G_A A_A} \frac{d^2 M_A}{dx^2}, \quad (1.70)$$

here, χ – cross-section shear factor, G – shear modulus of the layer.

The model assumes the interface shear–slip curve, composed of two parts. As layers slip, the shear stress: 1) increases, reaching the highest interface shear capacity; and 2) decreases, eventually reaching a shear stress value equal to 0. It should be noted that the decrease in shear stress is not brittle but softened. The curve is given in Figure 1.29. The equations for interface behaviour and element flexural behaviour at the first and second parts of the curve, respectively (Eq. 1.72):

$$\frac{d^2\xi}{dx^2} = \left[\left(\frac{1}{E_A A_A} + \frac{1}{E_B A_B} \right) + \left(\frac{J_A}{E_B J_B W_A} + \frac{1}{E_B W_B} \right) \frac{H_B}{2} \right] \frac{D\tau_e}{\xi_e} \xi$$

$$+ \left(\frac{J_A}{E_B J_B W_A} + \frac{1}{E_B W_B} \right) \rho_B q x - \left(\frac{J_A}{E_B J_B W_A} + \frac{1}{E_B W_B} \right) \frac{qL}{2} \rho_B, \quad (1.71)$$

$$\frac{d^2\xi}{dx^2} = - \left[\left(\frac{1}{E_A A_A} + \frac{1}{E_B A_B} \right) + \left(\frac{J_A}{E_B J_B W_A} + \frac{1}{E_B W_B} \right) \frac{H_B}{2} \right] \frac{D\tau_e}{(\xi_u - \xi_e)} \xi$$

$$+ \left(\frac{J_A}{E_B J_B W_A} + \frac{1}{E_B W_B} \right) \rho_B q x - \left(\frac{J_A}{E_B J_B W_A} + \frac{1}{E_B W_B} \right) \frac{qL}{2} \rho_B \quad (1.72)$$

$$+ \left[\left(\frac{1}{E_A A_A} + \frac{1}{E_B A_B} \right) + \left(\frac{J_A}{E_B J_B W_A} + \frac{1}{E_B W_B} \right) \frac{H_B}{2} \right] \frac{D\tau_e}{(\xi_u - \xi_e)} \xi_u,$$

here, τ_e – the highest interface shear stress, ξ_e – the interface slip at the highest interface shear stress, q – uniformly applied load, and ξ_u – the final interface shear slip.

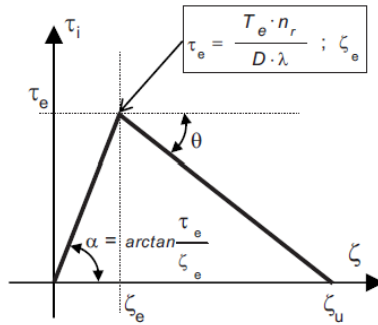


Fig. 1.29. Interface shear stress–layer slip relationship curve (Foraboschi, 2009)

1.4.3. Peng et al. Model

Peng et al. (2024) proposed an analytical method for evaluating the deflection of multilayered concrete elements comprising more than two layers. The method incorporates interface stiffness and interlayer slip but is limited to elements in which all layers have identical thickness and material properties. The geometry of the multilayered beam and its free-body diagram are shown in Figure 1.30. The following assumptions form the basis of the model:

1. All the deformations (layer and interface) are linearly elastic.

2. Due to the first assumption, the longitudinal shear force t is equal to $t = K\delta$. Here, δ is the slip between two layers and K is the interface shear stiffness.
3. The layered element is slender, and Euler–Bernoulli beam theory is applicable.
4. The interface layer is assumed to have negligible thickness, and normal deformation at the interface is neglected. As a result, only tangential deformation is considered, and all layers exhibit equal vertical deflection.

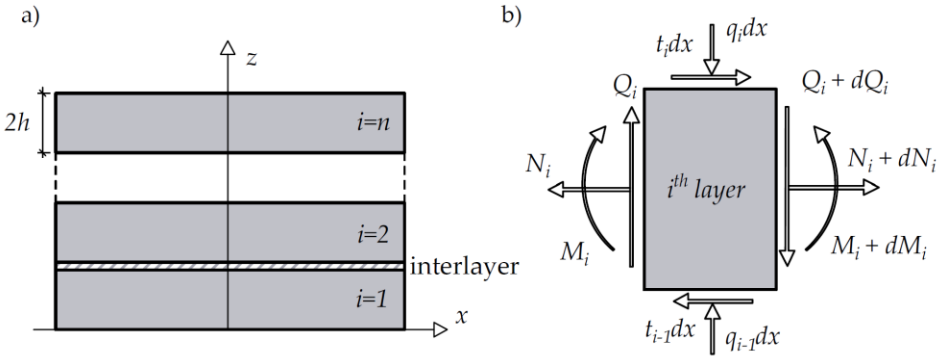


Fig. 1.30. Diagrams of layered element: a) geometry of multilayered beam; b) free-body diagram (Peng et al., 2024)

The general equation for the displacement of the i^{th} layer (Eq. 1.73):

$$u_i(x, z) = u_{i0} - [z - h(2i - 1)] \frac{dw}{dx}, \quad i = 1, 2, \dots, n, \quad (1.73)$$

here, u_{i0} – displacement of the middle plane of the i^{th} layer and w – deflection of the element, which is equal between all layers. The axial stresses of the layers can be determined as follows (Eq. 1.74):

$$\sigma_i(x, z) = E \left[\frac{du_{i0}}{dx} - (z - 2hi + h) \frac{d^2w}{dx^2} \right], \quad (1.74)$$

here, E – layer elastic modulus. The axial forces and the bending moment of the i^{th} layer can be determined as follows (Eqs. 1.75, 1.76):

$$N_i(x) = b \int_i \sigma_i dz = EAu'_{i0}, \quad (1.75)$$

$$M_i(x) = b \int_i \sigma_i z dz = EI w'', \quad (1.76)$$

here, b – element thickness, $A = 2bh$ – the area of the cross-section, and $I = \frac{2}{3}bh^3$ – the second moment of the area.

The interface shear force can be calculated from the following expression (Eq. 1.77):

$$T'' = \frac{K}{E} \left[\frac{2f(n)}{(n-1)A} + \frac{(n-1)(2h)^2}{nI} \right] T + \frac{(n-1)2hK}{nEI} Q, \quad (1.77)$$

here, n – the number of the layers and Q – the layered element transverse force. The deflection of the element $w(x)$ can be determined by substituting the result of $T(x)$ to the following equation (Eq. 1.78):

$$nEI w''' = 2hT + Q. \quad (1.78)$$

1.4.4. Marčiukaitis et al. Model

Marčiukaitis et al. (2006) proposed an analytical deflection model for composite members subjected to bending, based on the built-up bars theory. The study focused on concrete–steel sheeting composite elements. However, the method is also applicable to concrete–concrete layered elements. In the equations, properties of different materials are considered. The model accounts for a relative slip between layers through the interface shear stiffness. As the slip develops, the effective stiffness of the layered element decreases. The method can be applied from the fully composite stage when no interface slip is present up to failure caused by excessive interface deformation. The mathematical formulation begins with the expression for a relative slip (Eq. 1.79).

$$u = u_1 - u_2, \quad (1.79)$$

here, u_1 and u_2 – horizontal displacements of the first and second layers. By considering the geometric, material characteristics of the layers, the interface forces at the layers and at the interface, such an expression can be written (Eq. 1.80):

$$\frac{du}{dx} = T \left(\frac{1}{E_1 A_1} + \frac{1}{E_2 A_2} \right) - \frac{M_0 c}{E_1 I_1 + E_2 I_2} + \frac{T c^2}{E_1 I_1 + E_2 I_2}, \quad (1.80)$$

here, M_0 – the sum of bending moments not considering interface partial shear connection, T – interface shear force, c – distance between centroids of the layers, E – layer elastic modulus, A – layer cross-sectional area, and I – layer cross-section second moment of area. After further development of equations and addition of the coefficient $\lambda = \sqrt{\alpha\gamma}$, with which the model considers the stiffness of the interface, an equation for the deflection of the layered member can be written (Eq. 1.81):

$$\delta = M \left(\frac{l^2}{8E_{eff}I_{eff}} + \frac{1}{D} \left(\frac{ch(0.5\lambda) - 1}{\lambda^2 ch(0.5\lambda)} \right) \right), \quad (1.81)$$

here, M – the moment acting on the whole layered member, l – the span of the element subjected to bending, $E_{eff}I_{eff}$ – the cross-sectional stiffness of the layered element, and $\frac{1}{D}$ – another coefficient considering the layered element stiffness. One of the interface stiffness components is determined accordingly (Eq. 1.82):

$$\alpha = \frac{bG_w}{z_{eff}}, \quad (1.82)$$

here, b – width of the interface, z_{eff} – distance between neutral axis of the layers, and G_w – shear stiffness modulus. In the paper by Marčiukaitis et al. (2006), the latter coefficient was obtained experimentally from independent interface shear tests. The authors recommend this approach in the absence of analytical procedures for determining the shear stiffness modulus. Because interface deformation directly affects this coefficient, it can be used to account for interlayer slip. The flexural stiffness coefficients for the layered element are given in Eqs. (1.83)–(1.85):

$$\frac{1}{D} = \frac{1}{E_{c,eff}I_{c,eff} + E_pI_p} - \frac{1}{E_{eff}I_{eff}}, \quad (1.83)$$

$$E_{eff}I_{eff} = E_{c,eff}I_{c,eff} + E_pI_p + \frac{E_{c,eff}A_{c,eff}E_pA_pz_{eff}^2}{E_{c,eff}A_{c,eff} + E_pA_p}, \quad (1.84)$$

$$\gamma = \frac{1}{E_{c,eff} A_{eff}} + \frac{1}{E_p A_p} + \frac{z_{eff}^2}{E_{c,eff} I_{eff} + E_p I_p}. \quad (1.85)$$

1.4.5. Comparison of Flexural Stiffness Models

Comparing the analytical methods for evaluating the flexural stiffness of layered elements, several conclusions can be drawn. Although the method proposed by Magnucki et al. (2020) is derived from systems of differential equations, the authors provide convenient solutions that allow relatively straightforward algebraic analysis. This model considers stress and deformation of individual layers; however, it does not account for the interface stress–deformation state, partial interface shear connection, or slip. Thus, this model can only be used up to interface adhesive failure, and it overestimates the flexural stiffness of the layered element when used after adhesive failure. Foraboschi (2009) developed a more advanced model that explicitly links interface deformation, overall flexural stiffness, and the transmission of forces between layers. The approach also incorporates an interface shear resistance model that is consistent with these mechanisms. Despite its broad applicability, the model is comparatively complex and less suited for routine engineering use. The model developed by Peng et al. (2024) provides a suitable framework for estimating deflection, layer stresses, and internal forces in multi-layer concrete elements (two or more layers). The method incorporates the interface stiffness and an interlayer slip; however, it is restricted to systems in which all layers possess identical thicknesses and material properties. This assumption substantially limits the model’s applicability, as most layered concrete elements comprise layers with differing strengths and thicknesses. Averaging these parameters can significantly distort the predicted flexural stiffness. Moreover, since the study (Peng et al., 2024) does not present a procedure for determining interface stiffness, a monolithic shear stiffness value may need to be assumed. Consequently, the model’s validity may be confined only to interface adhesive failure. The final method, proposed by Marčiukaitis et al. (2006), incorporates the partial shear connection of the interface. Individual behaviours, geometries, and material characteristics of each layer are considered. By accounting for layer cracking and updating the interface shear stiffness parameter G_w , the model can be used to predict deflection before and after interface adhesive failure. However, similar to the study by Peng et al. (2024), Marčiukaitis et al. (2006) do not present an analytical procedure on how to determine the shear modulus G_w . This condition limits models’ applicability only up to the interface adhesive failure stage. Generally, the literature offers very few analytical approaches for determining G_w in concrete-to-concrete interfaces. As a result, the applicability of this model

is constrained by the need for experimentally obtained values of the interface shear stiffness.

1.5. Conclusions of the First Chapter and Formulation of the Dissertation Tasks

The following conclusions can be drawn after completing the literature review of layered concrete structural element research:

1. Layered concrete elements offer structural and environmental advantages, including greater flexibility in structural system design, strengthening of existing structural elements, and reduced material consumption.
2. Layered concrete element performance is governed by the characteristics of the interface. Interface failure is one of the most prominent failure modes for layered concrete elements. Therefore, both interface shear resistance and interface shear stiffness must be considered in the analysis of such elements.
3. Interface shear resistance and shear stress are governed by contributions of physical interface components – shear mechanisms. The effectiveness of shear mechanisms depends on concrete layer properties, interface surface roughness, connector characteristics, differential shrinkage between layers, and the applied loading.
4. Most interface behaviour models focus on predicting interface shear resistance. However, accurate analysis of the flexural stiffness of layered elements requires the determination of interface shear stiffness. Existing stiffness models for concrete-to-concrete interfaces are limited in number and scope, rarely accounting for multiple behaviour stages, changing contributions of shear mechanisms and differential shrinkage effect. Furthermore, most are restricted to specific interface conditions, such as defined roughness. These limitations highlight the need for a more comprehensive interface stiffness model.
5. When two layers of a layered concrete element are cast at different times, each layer experiences shrinkage at a different pace. This effect causes additional shear stress at the interface, decreasing adhesive interface resistance. This phenomenon is called differential shrinkage and should be considered during the analysis of layered concrete elements.
6. Several flexural stiffness models for layered concrete elements were reviewed. Some models do not consider interface shear stiffness or do not provide analytical expressions for its determination. Additionally, certain models inadequately represent individual layer properties. Therefore, the

analysis conducted in this dissertation requires a model that accounts for interface shear stiffness, as well as the material properties and geometries of the individual layers.

Based on the literature review and the identified research gaps, the following dissertation tasks were formulated:

1. To develop an analytical method for determining the shear stiffness of the concrete interface at different stages of interface behaviour.
2. To develop an analytical method for determining the deflection of layered concrete elements subjected to bending, considering the shear stiffness of the interface.
3. To develop a numerical model for simulating the flexural behaviour of a layered semi-precast concrete slab with plastic void formers.
4. To carry out experimental tests on layered concrete interfaces, layered concrete beams and layered concrete slabs with plastic void formers.
5. To validate the proposed analytical models by comparing the analytically obtained results with the experimental and numerical results.

2

Stiffness Models for Layered Concrete Interfaces and Layered Concrete Elements Under Bending

The Second Chapter introduces novel analytical models for predicting the behaviour of concrete interfaces, the effects of differential shrinkage, and the flexural stiffness of layered concrete elements with partial shear connection interfaces. In addition, a numerical model for a layered concrete slab incorporating plastic void formers is developed and presented. The contents of this chapter have also been published in the following works: (Masénas et al., 2021, 2023; Masénas & Valivonis, 2024a, 2025; Valivonis et al., 2026).

2.1. Shear Stiffness Model for Layered Concrete Interface

The previous chapter reviewed the existing interface behaviour models. Models addressing only shear resistance were found to be insufficient, as this dissertation requires a description of interface shear stiffness. Although several stiffness-rela-

ted models exist, they are limited in number and scope, rarely accounting for multiple interface behaviour stages, changing contributions of shear mechanisms and differential shrinkage effect. Furthermore, most are restricted to specific interface conditions, such as defined roughness. Consequently, a new interface stiffness model is developed and presented in this section.

The key parameter describing interface stiffness is the interface effective shear stiffness modulus G_{eff} , also referred to as the slip modulus. This parameter is typically obtained experimentally, and its value decreases as the slip between layers increases. When the interface shear stress–slip relationship is known for the full range of interface behaviour, the shear stiffness modulus can be calculated using Eq. 2.1 (Manojlovic & Kocetov-Misulic, 2016; Marčiukaitis et al., 2006):

$$G_{eff}(s) = \frac{\tau}{s}. \quad (2.1)$$

It should be noted that the value of G_{eff} must satisfy the condition $G_{eff} \leq 0.4E_{cm}$, where $0.4E_{cm}$ represents the shear stiffness of monolithic concrete. This indicates that, at the onset of slip, the initial interface shear stiffness is equal to the shear stiffness of a monolithic concrete section. This value decreases as the interface starts to crack and the layers start to slip. The subsequent step in evaluating interface stiffness is therefore the determination of shear stress and slip values over the full range of interface behaviour.

A theoretical model for interface shear behaviour was developed based on a comprehensive review of push-off test data available in the literature (Barbosa et al., 2017; Crane, 2010; Fang et al., 2020; Figueira et al., 2016; Júlio et al., 2010; Liu et al., 2019, 2021; Mohamad & Ibrahim, 2015; Scott, 2010; Semendary et al., 2020; Shaw & Sneed, 2014; Sneed et al., 2016), on recommendations from relevant design codes (European Committee for Standardization, 2023; International Federation for Structural Concrete (fib), 2020) and on studies of interface shear stress–layer slip relationships (Liu et al., 2019; Yang, 2016). The analysis of the presented literature identified several interface behaviour stages. A relationship was observed between interface stress and slip and various interface parameters, such as concrete strength, connector strength, connector ratio and others. Based on these relationships, regression analysis was performed, and corresponding equations were derived (Eqs. 2.2, 2.3, 2.5–2.8, 2.11–2.13). The results showed that the influence of interface parameters varies across different behaviour stages, indicating an evolving contribution of shear mechanisms. The variables reported to influence interface performance are summarised in Annex A.

The proposed model is based on a novel shear stress–slip relationship. The relationship curve, shown in Figure 2.1, is divided into four stages of interface

behaviour representing the principal novelty of the model. As mentioned earlier, the general shape and structure of this curve come from the analysis of experimental concrete interface test results, the recommendation of design codes, and relevant interface shear stress–layer slip relationship studies. Existing interface shear-resistance models typically address only a single behaviour stage, while available shear stress–slip models provide limited detail, particularly for smooth concrete-to-concrete interfaces. In contrast, the proposed model covers the full range of interface performance: from the onset of shear loading to the Stage where shear transfer is governed primarily by interface connectors after concrete-to-concrete bonding has been lost.

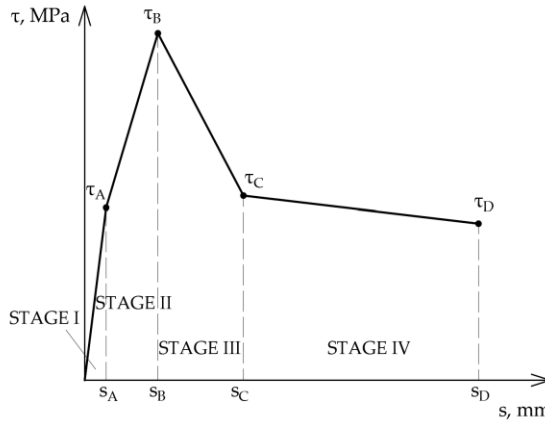


Fig. 2.1. Novel interface shear stress–layer slip relationship curve

At Stage 1, shear transfer at the concrete interface is governed solely by cohesive bonding between the layers. Initial interface cracking occurs at shear stress τ_A . According to Model Code 2010 (Fib Model Code for Concrete Structures 2010, 2013) and the referenced push-off studies (Barbosa et al., 2017; Crane, 2010; Fang et al., 2020; Figueira et al., 2016; Júlio et al., 2010; Liu et al., 2019, 2021; Mohamad & Ibrahim, 2015; Scott, 2010; Semendary et al., 2020; Shaw & Sneed, 2014; Sneed et al., 2016), this corresponds to slip values in the range of 0.01–0.05 mm. The shear stress–slip behaviour for this Stage is, therefore, defined by Eqs. 2.2–2.4:

$$\tau_A = 0.2\eta f_{ct}, \quad (2.2)$$

$$\eta = 11.2 \left(\frac{S_{L1}}{S_L} \right)^{1.59}, \quad (2.3)$$

$$s_A = 0.01 \div 0.05 \text{ mm}, \quad (2.4)$$

here, η – coefficient accounting for the influence of the interface location relative to the composite cross-section centroid. Under the pure shear condition (for example, in push-off test), it is equal to $\eta = 1.0$. f_{ct} – tensile concrete strength, S_{L1} – the first moment of the bottom layer area, and S_L – the first moment of the composite section area.

At the beginning of Stage 2, cohesive bonding at the interface begins to decrease, and other shear mechanisms join shear resistance. The following equations describe the interface behaviour at this Stage (Eqs. 2.5–2.7):

$$\tau_B = \eta \kappa (\tau_{fr} + 0.5 \tau_{dw}) - \sigma_{sh}, \quad (2.5)$$

$$\begin{cases} \kappa = 0.56 \left(\frac{f_y \rho}{f_c} \right)^{-0.32} \\ \kappa \geq 1.0 \end{cases}, \quad (2.6)$$

$$s_B = 106 f_c^{-2.08} + 18 \left(\frac{f_y \rho}{f_c} \right)^{2.08}. \quad (2.7)$$

At the end of Stage 2, at the point τ_B , the maximum combined cohesive and interlock resistance is reached. The analysis of experimental data indicates that τ_B is governed by the ratio $\frac{f_y \rho}{f_c}$, where f_y – connector yield stress, ρ – connector ratio, and f_c – weaker concrete compressive strength. This ratio reflects the relationship between connector-induced stresses and the concrete's compressive strength: higher concrete strength shifts τ_B towards cohesion and interlock, whereas lower strength increases the relative contribution of connectors. Coefficient κ directly depends on the value of this ratio. The term σ_{sh} in Eq. 2.5 represents the shear stress induced by differential shrinkage, which reduces τ_B . The components τ_{fr} and τ_{dw} correspond to shear friction and dowel action, respectively. The slip at this Stage, s_B , also depends on f_c and the ratio $\frac{f_y \rho}{f_c}$: higher concrete strength results in stiffer behaviour (lower s_B), while lower strength produces a more ductile behaviour (higher s_B).

At Stage 3, all cohesive and interlock mechanisms have failed. Shear transfer along the interface is provided solely by friction and dowel action. This Stage primarily represents the potential reduction in interface shear resistance following the peak. The expressions for Stage 3 shear stress and the corresponding slip are given in Eqs. 2.8 and 2.11. Eqs. 2.8–2.10 are based on recommendations by Eurocode 2 and Model Code 2020 (European Committee for Standardization, 2023; International Federation for Structural Concrete (fib), 2020). The shear stress components arising from friction and dowel action are defined in Eqs. 2.9 and 2.10:

$$\tau_C = \eta(\tau_{fr} + 0.5\tau_{dw}), \quad (2.8)$$

$$\tau_{fr} = \mu(\sigma_n + 0.005f_c) + f_y\rho(\mu\sin\alpha_c + \cos\alpha_c), \quad (2.9)$$

$$\tau_{dw} = \rho\sqrt{f_c f_y}, \quad (2.10)$$

$$s_C = 2.3f_c^{-0.28} - 0.00003A_s^{1.4}, \quad (2.11)$$

here, A_s – cross-sectional area of one interface connector in mm^2 , μ – interface surface friction coefficient, σ_n – compressive stress due to external loading, and α_c – interface connector inclination angle.

At Stage 4, the interface behaviour is governed solely by friction and dowel action. At this Stage, yielding of the interface connectors may occur. The corresponding expressions for shear stress and slip at Stage 4 are as follows (Eqs. 2.12–2.14):

$$\tau_D = \eta D(\tau_{fr} + 0.5\tau_{dw}), \quad (2.12)$$

$$D = 1.22(f_y\rho)^{-0.16}, \quad (2.13)$$

$$s_D = 6 \text{ mm}, \quad (2.14)$$

here, D – coefficient, which controls the magnitude of shear stress τ_D in relation to τ_C . In practical terms, the value of D determines whether the interface shear stress decreases, plateaus, or increases in Stage 4, depending on connector characteristics. When the connector diameter, the connector ratio, or the connector strength are low, the connectors tend to reach hardening or the kinking effect (Fib Model Code for Concrete Structures 2010, 2013) at relatively small slip values. Conversely, a larger value of the parameter $f_y\rho$ results in a delayed onset of

these effects. The slip value at Eq. 2.14 is equal to 6 mm. This constant limit was selected because the experimental push-off tests used to calibrate the model were, on average, conducted up to slip values of approximately 6 mm. In this model, all stresses (shear and normal), as well as all material strength parameters, shall be expressed in MPa, while interface slip shall be expressed in millimetres.

Another novelty of this dissertation is the incorporation of differential shrinkage when evaluating adhesive resistance at the interface. The term σ_{sh} in Eqs. 2.5 and 2.15 denotes the shear stress induced by differential shrinkage. The following equations (Eqs. 2.15–2.28) define the procedure for calculating differential shrinkage strains and the resulting stresses. The proposed model is based on the study by Elliott and Jolly (2014), with significant improvements, like the assumption that the interface is restrained (same deformation at the contact between layers). Also, the omission of the shrinkage strain value of the first layer, before the second layer casting, in the overall differential shrinkage effect, and other improvements. Differential shrinkage studies were also analysed for the refinement of the model (Abbasnia et al., 2005; Lampropoulos et al., 2014; Vinkler & Vitek, 2019). The distribution of shrinkage-induced forces and moments within the cross-section is shown in Figure 2.2, where layers 1 and 2 correspond to the precast and cast-in-place concretes, respectively. The assumed shrinkage strain distribution is presented in Figure 2.3.

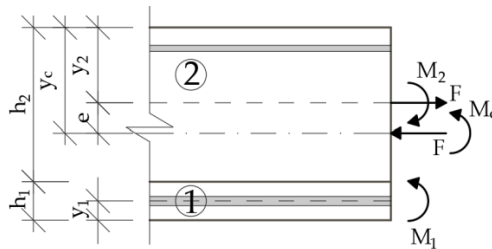


Fig. 2.2. Shrinkage-induced forces and moments at the layered element

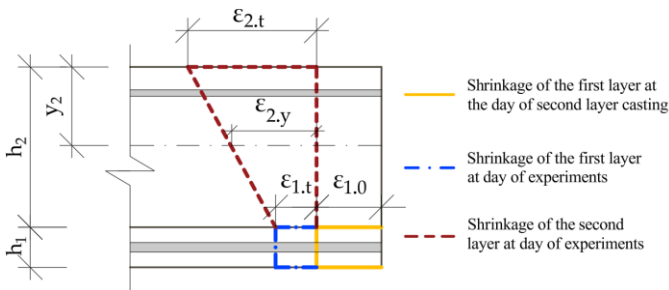


Fig. 2.3. Shrinkage strain distribution in the cross-section

Figures 2.2 and 2.3 illustrate that the first layer undergoes shrinkage both before and after the casting of the second layer. When the first layer reinforcement is positioned near the mid-depth, the shrinkage strain may be assumed uniform across its thickness. The bond at the interface between the layers is considered fully restrained and identical at both sides (Eq. 2.20). At the time of the second-layer casting, the concrete in the first layer is already hardened, while the concrete in the second layer remains formable. Consequently, the shrinkage deformation at the bottom of the second layer “follows” the shrinkage deformation at the top of the first layer. This is the physical explanation for the “restrained” interface. The concrete at the upper surface of the second layer does experience restriction due to contact with the first layer; however, since no direct contact between the layers occurs in this zone, shrinkage develops more independently than at the interface. It should be noted that flexural reinforcement restrains shrinkage regardless of the layer in which it is located (Eq. 2.23).

Differential shrinkage in a layered concrete element is defined as the difference between the shrinkage strain at the centroid of the second layer and at the top of the first layer (Eq. 2.19). The shrinkage strain at the centroid of the second layer is obtained geometrically (Eq. 2.22), using the shrinkage strains at the bottom and top surfaces of the layer (Eqs. 2.20 and 2.21). The shrinkage at the top of the second layer (and generally throughout all layer height) is reduced due to restraint from the bottom of the layer, the reinforcing bars, and the layer thickness itself (Eq. 2.21).

In Figure 2.2, the axial force F (Eq. 2.18) is theoretically applied at the centroid of the layered element and at the centroid of the second layer to reach an equilibrium, due to the strain difference between layers. Bending moments M_1 and M_2 (Eqs. 2.27, 2.28) around the centroids of the first and the second layers, respectively, form due to flexural reinforcement bending due to shrinkage. M_c (Eq. 2.17) is the resulting bending moment, combining all previously mentioned internal forces, acting around the centroid of the layered element.

$$\sigma_{sh} = \frac{F_v}{l_t b}, \quad (2.15)$$

$$F_v = F + M_c \frac{S_c}{I_c}, \quad (2.16)$$

$$M_c = Fe + M_1 - M_2, \quad (2.17)$$

$$F = \varepsilon_s E_c m A_2, \quad (2.18)$$

here, F_v – longitudinal force at the interface, resulting from differential shrinkage, l_i – interface length, b – interface width, F – axial force, applied to theoretically reach an equilibrium, due to the strain difference, M_c – composite cross-section bending moment, S – the first moment of one-layer area around the transformed composite cross-section, I_c – the second moment of the area of the transformed composite cross-section, e – distance between the centroids of the second layer and the composite cross-section, M_1 – the first layer bending moment, caused by bent reinforcement. M_2 – the same bending moment for the second concrete layer, ε_s – differential shrinkage strain, E_c – the first layer concrete modulus of elasticity, m – ratio between concrete elastic moduli of the second layer and the first layer, and A_2 – the second layer cross-sectional area.

$$\varepsilon_s = \varepsilon_{2,y} - \varepsilon_{1,t}, \quad (2.19)$$

$$\varepsilon_{1,t} = \varepsilon_1 - \varepsilon_{1,0}, \quad (2.20)$$

$$\varepsilon_{2,t} = \varepsilon_2 - \varepsilon_{2,c} - \varepsilon_{2,r} - \varepsilon_{2,s}, \quad (2.21)$$

$$\varepsilon_{2,y} = \frac{(\varepsilon_{2,t} - \varepsilon_{1,t})(h_2 - y_2)}{h_2} + \varepsilon_{1,t}, \quad (2.22)$$

here, $\varepsilon_{2,y}$ – shrinkage strain at the centroid of the second layer, $\varepsilon_{1,t}$ and $\varepsilon_{2,t}$ – shrinkage strain at the top of the first and the second layer, respectively, ε_1 and ε_2 – the first and the second layer free shrinkage, respectively, $\varepsilon_{1,0}$ – the first layer shrinkage, at the time of the second layer casting, $\varepsilon_{2,c}$ – concrete tensile strain, caused by compressed reinforcement (due to shrinkage), $\varepsilon_{2,r}$ – restrained shrinkage due to contact between concrete layers, $\varepsilon_{2,s}$ – restrained shrinkage due to size effect, h_1 – the first layer height, h_2 – the second layer height, y_1 – distance from the bottom of the first layer to the centroid of the layer, and y_2 – distance from the top of the second layer to the centroid of the layer. All shrinkage deformation values apart from ε_1 , ε_2 , and $\varepsilon_{1,0}$ are restrained shrinkage values due to contact between layers and reinforcement.

$$\varepsilon_{2,c} = \frac{\sigma_c}{E_{c,eff}}, \quad (2.23)$$

$$\varepsilon_{2,r} = R\varepsilon_2, \quad (2.24)$$

$$\varepsilon_{2,s} = \varepsilon_2(0.7h_2 + 0.03), \quad (2.25)$$

$$\sigma_c = \frac{\varepsilon_2 \rho E_s}{1 + \rho \frac{E_{c,eff}}{E_s}}, \quad (2.26)$$

$$M_1 = \varepsilon_1 E_s A_{s1} (y_1 - a_1), \quad (2.27)$$

$$M_2 = \varepsilon_2 E_s A_{s2} (y_2 - a_2), \quad (2.28)$$

here, σ_c – tensile stress in concrete, $E_{c,eff}$ – composite cross section concrete elastic modulus, R – shrinkage restraining coefficient (Abbasnia et al., 2005; Lampropoulos et al., 2014) (in a range of 0.10÷0.64), ρ – ratio of reinforcement in the area around the reinforcement, E_s – reinforcement elastic modulus, A_{s1} and A_{s2} – areas of reinforcement of the first and second layer, respectively, a_1 – distance from the bottom of the first layer to the centre of the reinforcement of the same layer, a_2 – distance from the top of the second layer to the centre of the reinforcement of the same layer, and y_c – distance from the top of the element to the composite centroid. Once the shear stress and slip values are defined for all four interface behaviour stages, the interface shear stiffness modulus G_{eff} can be computed for each stage.

2.2. Flexural Stiffness Model for Layered Concrete Beams with Partial Shear Connection Interfaces

An analytical deflection method for layered elements – the built-up layers method – is employed in this study. The method, originally used by Marčiukaitis et al. (2006) for concrete–steel sheeting composite members and introduced in the First Chapter, is adapted here for concrete-to-concrete layered elements. Its main advantage is the explicit consideration of interface shear stiffness, which enables the evaluation of the resulting flexural stiffness of the entire element. The internal force and moment distribution within the layered cross-section is illustrated in Figure 2.4. The corresponding deflection expression for a layered element subjected to bending is given in Eq. 2.29:

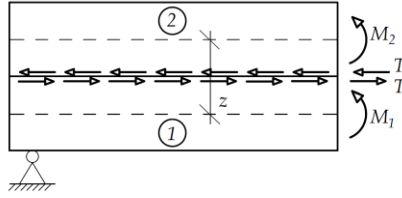


Fig. 2.4. Distribution of forces and moments in a layered element

$$w = M \left(\left(\frac{l^2}{8E_{eff}I_{eff}} \right) + \frac{1}{D} \left(\frac{\cosh(0,5\lambda l) - 1}{\lambda^2 \cosh(0,5\lambda l)} \right) \right), \quad (2.29)$$

$$\frac{1}{D} = \frac{1}{E_{c,eff,1}I_{eff,1,cr} + E_{c,eff,2}I_{eff,2,cr}} - \frac{1}{E_{eff}I_{eff}}, \quad (2.30)$$

$$\lambda = \sqrt{\alpha\gamma}, \quad (2.31)$$

$$E_{eff}I_{eff} = E_{c,eff,1}I_{eff,1,cr} + E_{c,eff,2}I_{eff,2,cr} + \frac{E_{c,eff,1}E_{c,eff,2}A_{eff,1,cr}A_{eff,2,cr}z_{eff}^2}{E_{c,eff,1}A_{eff,1,cr} + E_{c,eff,2}A_{eff,2,cr}}, \quad (2.32)$$

$$\gamma = \frac{1}{E_{c,eff,1}A_{eff,1,cr}} + \frac{1}{E_{c,eff,2}A_{eff,2,cr}} + \frac{z_{eff}^2}{E_{c,eff,1}I_{eff,1,cr} + E_{c,eff,2}I_{eff,2,cr}}, \quad (2.33)$$

$$\alpha = \frac{bG_{eff}}{z_{eff}}. \quad (2.34)$$

The values in the equations were explained in the First Chapter. In the present adaptation of the analytical method, the cross-sectional and material properties correspond to two concrete layers rather than a concrete–steel composite section. Geometric layer cross-section properties are determined as follows (Eqs. 2.35–2.36):

$$A_{eff,i,cr} = bx_{i,cr}, \quad (2.35)$$

$$I_{eff,i,cr} = \frac{bx_{i,cr}^3}{3} + \frac{E_s}{E_{c,eff}} A_{s,i} (d_i - x_{i,cr})^2. \quad (2.36)$$

The neutral axis of the cracked cross-section is determined according to Eq. 2.37:

$$A_{eff,i,cr} x_{cr} = S_{eff,i,cr} \rightarrow x_{cr}, \quad (2.37)$$

here, $S_{eff,i,cr}$ – the second moment of the layer cross-section area. By considering layer cracking and adjusting the interface shear stiffness value G_{eff} , the model can be used to determine deflection at different loading and deformation stages. Coefficient G_{eff} can be determined according to the method presented in Section 2.1. The interrelation between theoretically determined interface shear stress and applied transverse load is expressed in Eq. 2.38:

$$\tau = \frac{VS_{x,s}}{I_c b}, \quad (2.38)$$

here, V – transverse load, acting on the beam, $S_{x,s}$ – the first moment of area on one side of the interface, I_c – moment of inertia of the composite cross-section, and b – width of the interface. The bending moment at which the element subjected to bending starts cracking is determined according to Eq. 2.39:

$$M_{cr} = \frac{f_{ct} I_c}{y_c}. \quad (2.39)$$

2.3. Numerical Model of Layered Concrete Element with Partial Shear Connection Interface

In addition to the analytical analysis of layered element behaviour, a numerical analysis of a layered concrete slab was performed. A semi-precast slab with plastic void formers, tested under four-point bending (Fig. 2.5), was modelled. The slab contained no interface connectors. For the application of loads and supports, metal loading plates were modelled. The model was meshed into 3D quadrilateral finite elements, which were 20 mm in size. Model material properties are presented in Table 2.1. For concrete compression and tension, Thorenfeldt (TNO DIANA BV, 2015) and brittle curves (DIANA FEA BV, 2017) were used, respectively. Reinforcement was modelled with von Mises plasticity. Interface behaviour was modelled as purely elastic. The normal stiffness of the interface was taken as the elastic modulus of concrete. The shear stiffness was initially set to $0.4E_{cm}$, corresponding to monolithic behaviour, and was progressively reduced with increasing load. The final numerical model is shown in Figure 2.6. Nonlinear analysis was performed using the arc-length control method, and the model was

evaluated in discrete load steps. These load increments correspond to those marked on the experimental load–deflection curve in Figure 2.7.

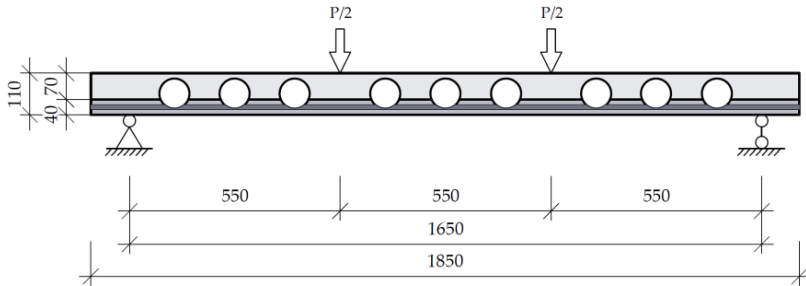


Fig. 2.5. Layered slab test arrangement

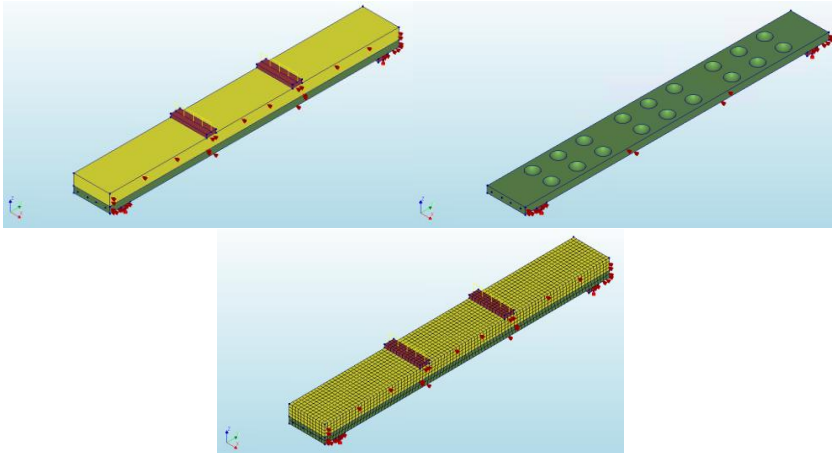


Fig. 2.6. Layered slab numerical model

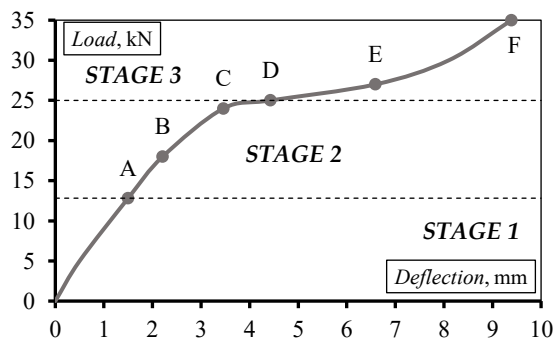


Fig. 2.7. Loading levels of layered concrete slab

Table 2.1. Numerical model material characteristics

Concrete	
Compressive strength, MPa	37.00
Tensile strength, MPa	2.83
Elastic modulus, GPa	32.58
Reinforcement	
Yield stress, MPa	470.00
Elastic modulus, GPa	199.00
Interface	
Normal stiffness, N/mm ³	33.00
Shear stiffness, N/mm ³	13.00±0.38

For calculating the deflection of layered concrete elements under bending, three flexural behaviour stages of the experimental specimen were identified (Fig. 2.7). In this figure, the horizontal axis represents deflection at midspan, and the vertical axis represents load P (Fig. 2.5). Stage 1 corresponds to elastic behaviour with a fully rigid (monolithic) interface. Stage 2 begins once flexural cracking occurs, the member exhibits nonlinear flexural behaviour while the interface remains fully bonded. Stage 3 starts when interface stiffness begins to decrease due to interface cracking, resulting in the interface exhibiting partial shear connection and increasing layer slip.

During the numerical analysis, the normal stress distribution in the cross-section and the shear stress distribution along the interface were evaluated. Normal stresses were examined at levels B, C, D, E, and F (Fig. 2.7), while interface shear stresses were assessed at levels A, C, D, E, and F. Up to level A, the slab exhibited elastic behaviour. Levels B and C corresponded to Stage 2, where the slab behaved in a more nonlinear way due to cracking. At level D, slip between layers initiated, marking the beginning of Stage 3. Continued layer slip was observed at level E, and flexural failure occurred at level F. Normal stress was determined in three sections (S_{YY1} , S_{YY2} , and S_{YY3}) and along the top fibre at the location of S_{YY3} , while interface shear stresses τ_{SY} were obtained along the layer interface. The locations of these sections are illustrated in Figure 2.8.

Under load level A, when the interface between the concrete layers remains intact, the shear stress at the slab end is equal to $\tau = 0.095$ MPa. At a distance of 300 mm from the edge, the stress increases to $\tau = 0.202$ MPa (Fig. 2.9). At load level C, the interface is still undamaged, and the shear stress distribution follows the same trend, with proportionally higher values. At load level D, the interface slip initiates, producing a sudden increase in shear stress at approximately 0.225 m from the slab edge. Here, $\tau = 0.270$ MPa is recorded at the edge and $\tau = 0.346$ MPa at 300 mm. At level E, shear stress becomes more uniform, and the local peak is

reduced. At level F, a continued slip produces a distribution similar to that at level E: $\tau = 0.420$ MPa at the slab end and $\tau = 0.461$ MPa at 300 mm. These results indicate that at load level D (25 kN), the interface transitions to a state of partial shear connection.

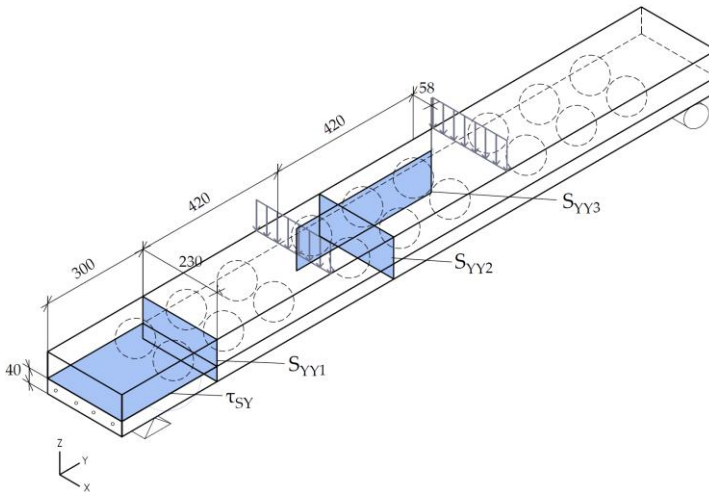


Fig. 2.8. Stress distribution analysis sections

The analysis of normal stress distribution in section S_{YY1} (Fig. 2.10) shows that under load B, the stress varies linearly with the section depth, and the layered slab behaves similarly to a solid member. Under load C, a local increase in normal stress appears at the interface level (the bottom layer depth is 40 mm). This stress concentration becomes more pronounced under load D. Under load E, the bottom layer begins to crack. Under load F, cracking in the bottom layer continues, while compressive stresses in the top layer increase. The analysis of stresses in section S_{YY2} (Fig. 2.11) shows that, at mid-span, normal stresses initially follow a linear distribution through the depth. Under load level B, the bottom layer and part of the upper layer already experience cracking. With increasing load, cracking propagates upward toward the compression zone. In section S_{YY3} , load level B initiates cracking in the bottom layer, and the layer appears fully cracked at a relatively low load. The top layer, however, continues to carry bending independently of the bottom layer. As shown in Figure 2.12, tensile stresses develop at the bottom and compressive stresses at the top, with tensile stress varying linearly and compressive stress following a parabolic distribution. As the load increases, tensile stresses in the top layer diminish due to progressive cracking, while compressive stresses increase accordingly.

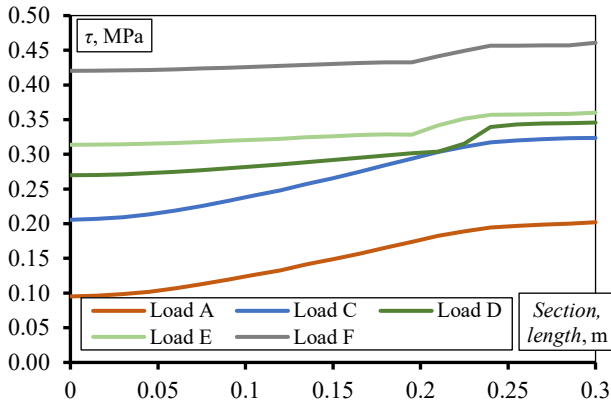


Fig. 2.9. Shear stress distribution at the interface

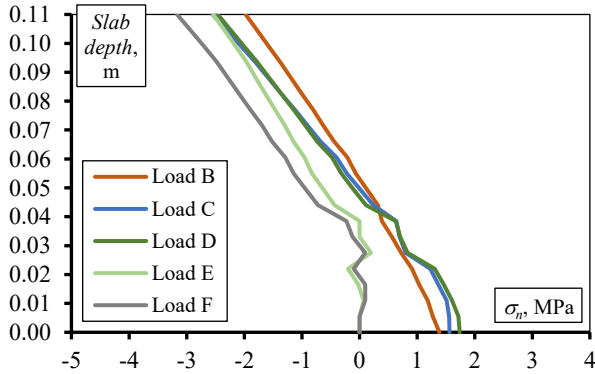


Fig. 2.10. Normal stress distribution at the section S_{Y1}

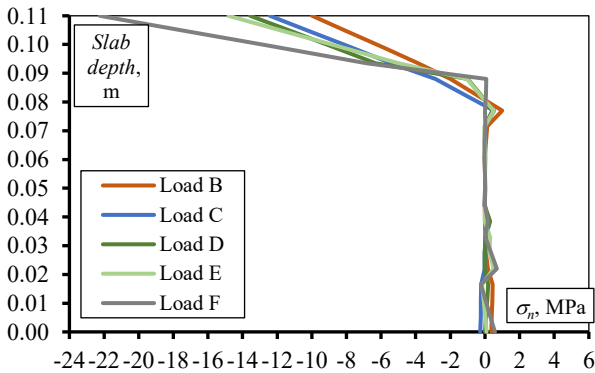


Fig. 2.11. Normal stress distribution at the section S_{Y2}

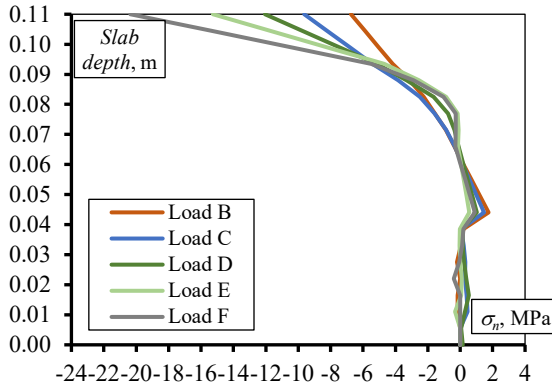


Fig. 2.12. Normal stress distribution at the section S_{YY3}

The numerical analysis has disclosed that normal cracks in the slab appear near the voids in the sections. Calculations have shown that higher stresses are concentrated near the voids and are significantly lower in concrete webs. The maximum compressive stress was observed in the areas of plastic inserts next to load application points. Stress distribution along the length of the slab is shown in Figure 2.13.

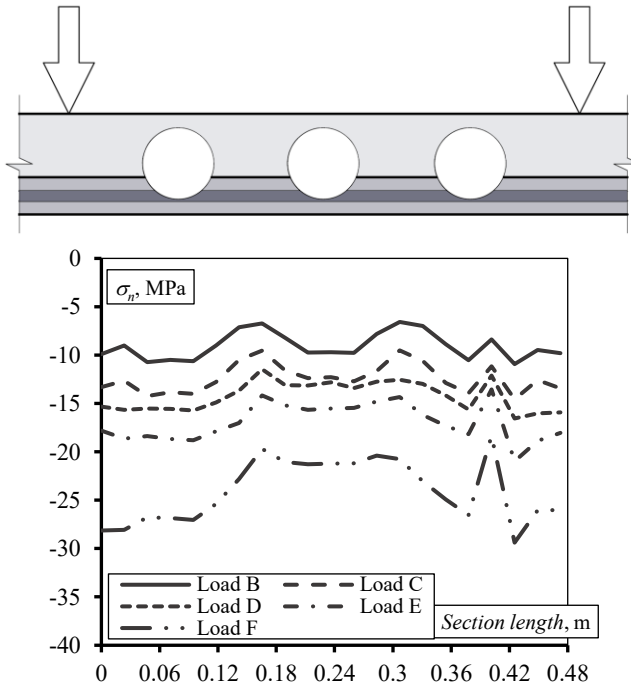


Fig. 2.13. Normal stress distribution at the top of the section S_{YY3}

The numerical results were compared with the experimental results obtained for a layered slab with the same geometry and material properties, tested by Ibrahim (2019). The comparison of numerical and experimental curves led to validation of the numerical model. The experimental slab failed in bending at a load of 35 kN, with interface failure occurring at approximately 25 kN. The experimental load–deflection curve is shown in Figure 2.14. This figure depicts slab deflection at midspan. During Stages 1 and 2, the numerical deflections closely matched the experimental results. In Stage 1, the load–deflection behaviour was linear, as the concrete remained elastic. In Stage 2, cracking initiated, producing a nonlinear behaviour; the precast bottom layer was the first to crack, as confirmed by stress distribution analysis. In Stage 3, some differences between numerical and experimental deflections could be observed. Despite deviations during the slip, numerical deflections remained close to experimental values at the beginning of interface degradation, indicating that the model adequately represents interface behaviour. Overall, the strong agreement between numerical and experimental results supports the validity of the numerical model.

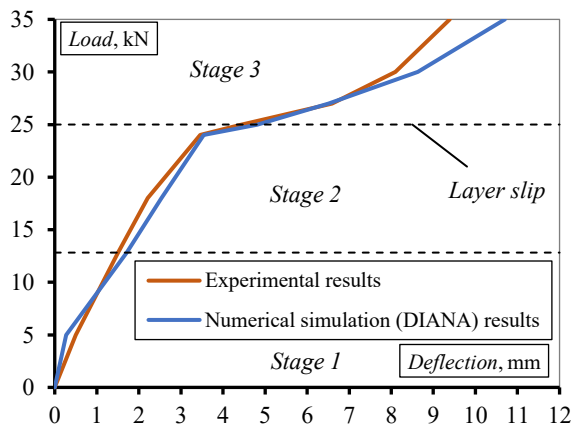


Fig. 2.14. Experimental and numerical slab load–deflection curves

2.3. Conclusions of the Second Chapter

The content of the chapter can be summarised by these conclusions:

1. A novel interface stiffness model has been developed. The model is based on the interface shear stress–slip relationship curve and distinguishes four stages of interface behaviour. Each stage reflects the involvement of new shear mechanisms and the combined shear mechanism action. Using the

identified shear stress and slip values at these stages, the interface shear stiffness can be determined accordingly.

2. One of the key novelties of the proposed interface stiffness model is the inclusion of the differential shrinkage effect. An additional model was developed to account for this phenomenon. It considers the shrinkage restraint at the interface, the influence of reinforcement and layer properties. Ultimately, the differential shrinkage stress value, which reduces the adhesive interface resistance, is determined.
3. A flexural stiffness model based on the built-up layers theory was adapted for layered concrete elements. This model enables the deflection of the layered element to be determined while accounting for the individual properties of the two layers and the varying interface shear stiffness. The corresponding values of interface stiffness can be obtained using the proposed interface stiffness model.
4. A numerical finite element model of a layered slab with void formers was developed. The analysis showed that interface deformation leads to a redistribution of normal and shear stresses, causing the layers to act more independently and contributing to intensified crack formation. In addition, higher concentrations of normal stress were observed in the regions adjacent to the voids created by the void formers, while lower stress levels occurred in the concrete webs.

3

Experimental Investigations of Layered Concrete Elements with Partial Shear Connection Interfaces

This chapter presents experimental tests of seventeen push-off specimens to improve the understanding of concrete interface behaviour and the influence of interface connectors. In addition, six layered concrete beams were tested to evaluate the behaviour of layered concrete elements under bending, including flexural capacity, interface behaviour, cracking patterns, and other relevant aspects. Finally, two semi-precast concrete slabs incorporating plastic void formers were tested. The results of all experimental investigations were used to validate the proposed analytical models. The material presented in this chapter has also been published in the following studies: (Masénas et al., 2021; Masénas & Valivonis, 2024a, 2025; Valivonis et al., 2026).

3.1. Experimental Investigation of Concrete Interface

Seventeen experimental push-off specimens were tested to investigate the behaviour of the concrete layer interface. In Figure 3.1a, a typical push-off specimen is presented. The lower layer is the first concrete layer, while the upper one is the

second concrete layer. In this research, alongside a typical specimen, with connectors perpendicular to the interface (Fig. 3.1a), as is commonly presented in the literature, several new types of experimental specimens were constructed. All types of specimens are summarised in Table 3.1.

Table 3.1. Types of push-off specimens

Specimen type	P	L1	L2	S
Interface type	Smooth	Smooth	Smooth	Shear keys
Connector arrangement	Perpendicular to the interface	Lattice girder type	Lattice girder type	Perpendicular to the interface

Specimens shown in Figures 3.1b and 3.1c had interface connectors inclined relative to the interface. These specimens were designed to simulate an interface reinforced by a lattice girder, as commonly found in typical filigree slabs. Notably, specimens P, L1, and L2 had smooth interfaces. The specimen depicted in Figure 3.1d was constructed to have its interface shaped in the form of shear keys (Fig. 3.1e). Similar interfaces are found in connections between precast concrete panel walls (Rizkalla et al., 1989; Sørensen et al., 2017). The experimental specimens were labelled as follows: P (perpendicular connectors), L1 (type 1 lattice girder connectors), L2 (type 2 lattice girder connectors), and S (shear key interface). Different specimens within the same category were numbered sequentially: L1-1, L1-2, L1-3, etc. The interface connector inclination angles of specimens P, L1 and L2 are depicted in Figure 3.2. Specimens S had identical connector inclination angles to specimens P.

Normal-weight concrete was used for all experimental specimens. The 28-day compressive strength of each layer was determined by testing $100 \times 100 \times 100$ mm cubes, converting the results to the standard $150 \times 150 \times 150$ mm cube strength, and subsequently to cylindrical strength (ACI Committee 318, 2014). The specimens consisted of two concrete layers with intentionally different properties: the first layer had higher compressive strength, reflecting typical filigree slab construction where the precast layer is stronger than the cast-in-place topping. Compressive strength on the day of testing was obtained from 150×300 mm cylinders, from which the elastic modulus was also derived. Flexural tensile strength was determined using three-point bending tests on prisms with a 100×100 mm cross-section and a 300 mm span. A summary of concrete properties is provided in Table 3.2.

The interface situated between the two concrete layers measured $240 \text{ mm} \times 120 \text{ mm}$. The interface was crossed by eight bars of 4 mm interface connectors. This diameter was selected to induce a more plastic behaviour at the interface and is commonly used by lattice girder manufacturers (*FILIGRAN, 2025*)(*AVI, 2025*). The resulting interface connector ratio was 0.35%. The stress–strain diagrams of the connectors are presented in Figure 3.3. Three tested bars exhibited similar yield stress values, with an average yield stress of 607 MPa and an average elastic modulus of 183 GPa. Ultimate stress value was calculated as the average and was equal to 675 MPa. The average ultimate strain was equal to $\varepsilon_u = 0.0317$. The remaining reinforcement consisted of S500 12 mm bars.

The specimens consisted of two concrete layers. The first layer was cast, and the second layer was placed 23 days later. The specimen construction process is depicted in Figure 3.4. Before casting the second layer, the substrate was not wetted, classifying it as a dry surface (*Elliott & Jolly, 2014*). All interfaces were cleaned thoroughly to remove dust, laitance, and other contaminants. Concrete prisms measuring $400 \text{ mm} \times 100 \text{ mm} \times 100 \text{ mm}$ were cast from the same batches as the experimental specimens and used to measure the shrinkage of both layers. Shrinkage was recorded using a mechanical strain gauge, and the results are presented in Section 3.4.

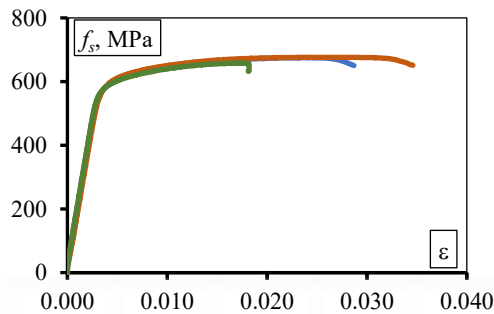


Fig. 3.3. Interface connector stress–strain curves



Fig. 3.4. Push-off shear specimen construction process

Displacement-controlled loading was used in the push-off tests to accurately capture the force–slip relationship. The load was applied at a rate of 0.5 mm/min. A typical test setup is shown in Figure 3.5. A spherical hinge was installed on the loading head to eliminate eccentricity. Displacements were recorded using LVDTs configured to measure both vertical slip of the upper concrete layer and horizontal opening of the interface. The vertical slip, representative of layer-slip measurements typically used in bending tests, was captured by transducer V, positioned at the bottom of the upper layer. Interface separation was measured by transducers H1 and H2, placed at the top and mid-height of the interface, respectively, as shown in Figure 3.5. All LVDTs had an accuracy of ± 0.001 mm.

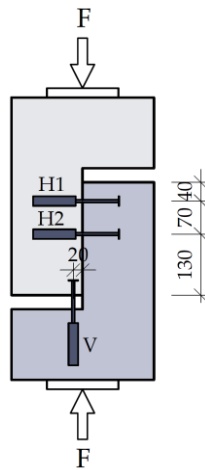


Fig. 3.5. Push-off shear specimen testing arrangement

Experimental specimens P, L1, and L2 failed due to interface shear, attributed to the smooth interface and differential shrinkage between layers. Specimens of type S exhibited shear key failure. Due to the different failure patterns, the experimental results (interface shear stress and slip) for specimens P, L1, and L2 are presented in Tables 3.3 and 3.4, while the results for specimens S are presented separately. Four interface behaviour stages, presented in the previous chapter (Fig. 2.1), are also evident in the experimental shear stress-layer slip diagrams presented in this paper. The points of initial crack formation, loss of adhesion (correlation between sudden shear stress drop and a noticeable crack formation at the interface), and failure of the first interface connector were determined by physically observing the tests and interpreting the experimental curves. Experimental investigations validated the proposed interface behaviour curve, presented in the Second Chapter.

Table 3.3. Shear stress values at the interfaces of experimental push-off specimens P, L1, and L2

Specimen	Shear stress at the first crack, MPa			Shear stress at the loss of adhesion, MPa			Shear stress at failure of the first connector, MPa			Failure Mode
	Individual	Average	SD	Individual	Average	SD	Individual	Average	SD	
P-1	0.66	0.59	0.10	1.15	1.08	0.11	1.93	1.84	0.11	Interface shear
P-2	0.47			0.96			1.86			Interface shear
P-3	0.63			1.14			1.72			Interface shear
L1-1	0.22	0.50	0.22	1.10	1.24	0.14	1.78	1.70	0.13	Interface shear
L1-2	0.28			1.39			1.55			Interface shear
L1-3	0.80			1.16			1.56			Interface shear
L1-4	0.60			1.42			1.69			Interface shear
L1-5	0.59			1.28			1.84			Interface shear
L1-6	0.51			1.11			1.80			Interface shear
L2-1	0.32	0.50	0.23	1.22	1.12	0.29	1.92	2.03	0.16	Interface shear
L2-2	0.84			1.55			2.24			Interface shear
L2-3	0.23			0.69			1.83			Interface shear
L2-4	0.40			1.15			2.19			Interface shear
L2-5	0.66			0.91			2.00			Interface shear
L2-6	0.57			1.21			2.01			Interface shear

Table 3.4. Layer slip values of experimental push-off specimens P, L1, and L2

Specimen	Slip at loss of adhesion, mm			Slip at failure of the first connector, mm		
	Individual	Average	SD	Individual	Average	SD
P-1	0.11	0.06	0.04	5.82	6.09	0.50
P-2	0.03			6.66		
P-3	0.05			5.78		
L1-1	0.10	0.08	0.02	4.55	5.10	0.46
L1-2	0.07			4.84		
L1-3	0.07			5.24		
L1-4	0.11			5.27		
L1-5	0.06			4.83		
L1-6	0.07			5.86		
L2-1	0.04	0.07	0.04	3.32	3.62	0.29
L2-2	0.07			3.33		
L2-3	0.03			4.08		
L2-4	0.09			3.51		
L2-5	0.04			3.79		
L2-6	0.12			3.70		

Three type P specimens were tested (Fig. 3.6a). For specimen P, the average shear stress at the loss of adhesion (end of Stage 2 in Fig. 2.1) was 1.08 MPa, corresponding to 59% of the peak interface shear stress and occurring at an average slip of 0.06 mm. Model Code 2020 (International Federation for Structural Concrete (fib), 2020) indicates that adhesion loss should occur at slips not exceeding 0.05 mm, meaning the measured slip was effectively consistent with the predicted range. Specimens L1 and L2 exhibited similar slip values at adhesion loss. A pronounced shear-stress drop followed the loss of adhesion (Fig. 3.6a), marking the transition to interface behaviour Stage 3 and. Thereafter, shear stress increased again, marking Stage 4. Shear stress increased until the first connector/connectors failed, after which the interface shear stress dropped. The average peak shear stress for type P specimens was 1.84 MPa, with the first connector failing at an average slip of 6.09 mm. Standard deviations in Table 3.3 reflect higher variability in stages governed by concrete surface characteristics and lower variability in stages governed by steel connector behaviour. Complete interface failure for specimens P, L1, and L2 is shown in Figure 3.7.

During testing, transducers H1 and H2 measured the interface crack width, as shown in Figure 3.5. Figure 3.6b presents the relationship between perpendicular interface opening and layer slip for specimens P. The crack width increased until a slip of approximately 2 mm and remained nearly constant while slip continued. This corresponds to the increase in shear stress observed in Figure 3.6a and is attributed to connector-induced clamping. At a slip of about 6 mm, the crack width began to rise sharply, indicating the onset of connector failure. For specimens P, the measured crack width was generally greater at the top of the interface, which is attributed to the bending-dominated deformation of the connectors.

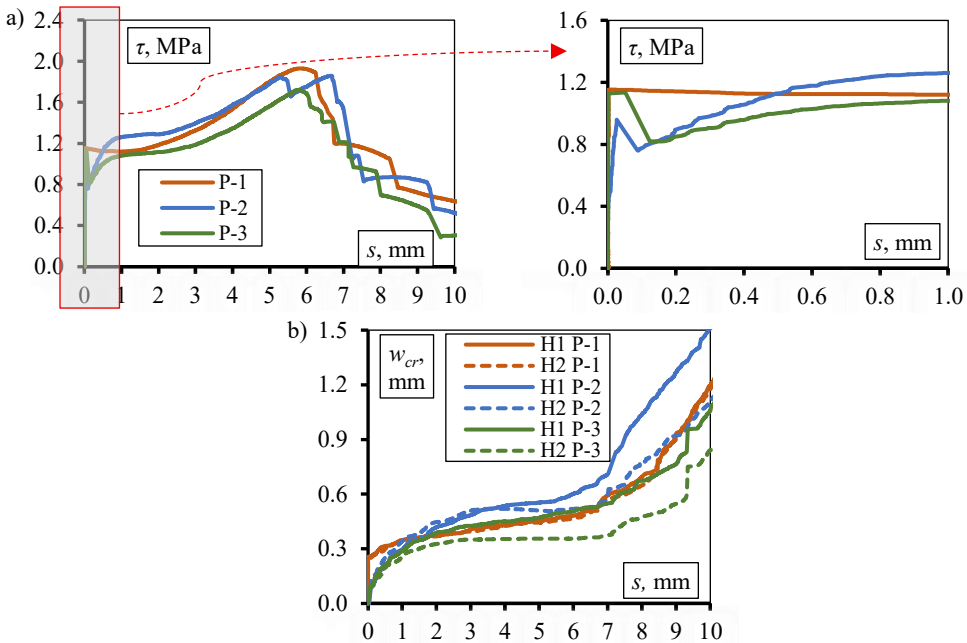


Fig. 3.6. Interface behaviour curves: a) shear stress–layer slip relationship and b) crack width–layer slip relationship of P specimens



Fig. 3.7. Complete specimen P, L1, and L2 interface failure

Six L1 specimens were tested (Fig. 3.8a). On average, adhesion was lost at a slip of 0.08 mm, corresponding to a shear stress of 1.24 MPa, or 73% of the peak interface shear stress. After this point, the shear stress dropped, indicating the onset of the third behaviour stage. In the fourth stage, the average peak shear stress reached 1.70 MPa. Connector shearing began at an average slip of 5.10 mm.

Figure 3.8b shows the development of the interface crack width for the L1 specimens. The crack widened rapidly up to a slip of approximately 1 mm, after which the rate of widening decreased substantially. Even when connectors began to fail (Fig. 3.8a), the crack width continued to increase gradually. At a slip of 10 mm, the crack remained narrower than that observed in the P specimens. This indicates that the L1 connector arrangement is more effective in limiting interface opening, likely due to reduced susceptibility to interface bending.

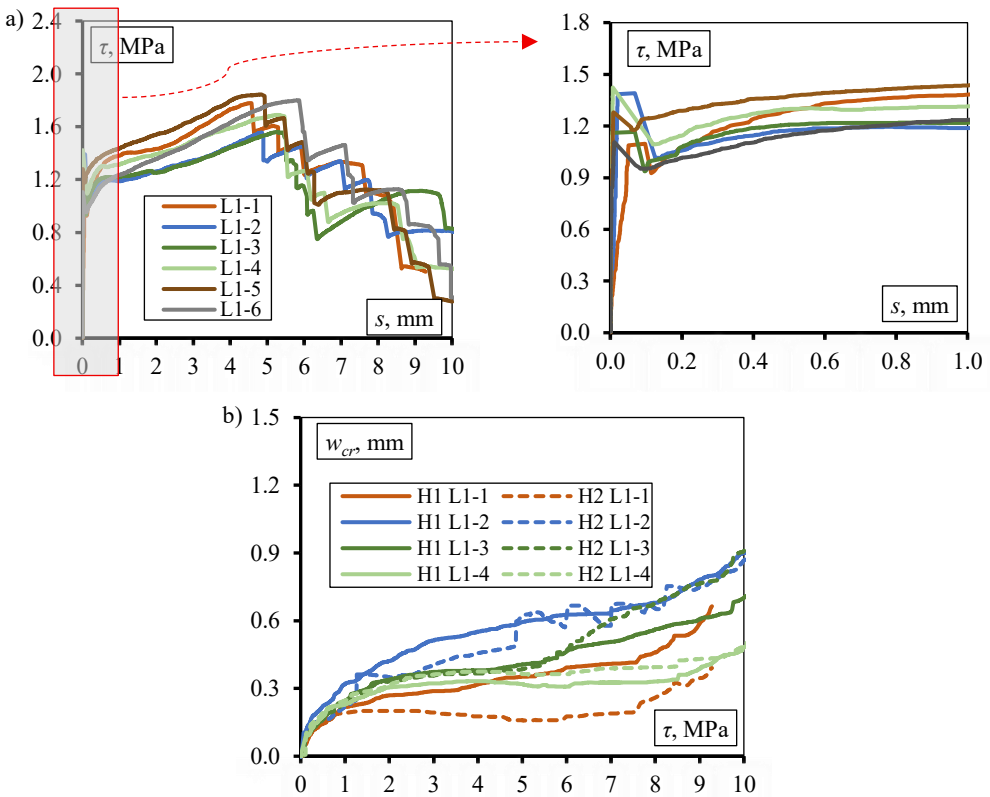


Fig. 3.8. Interface behaviour curves: a) shear stress–layer slip relationship and b) crack width–layer slip relationship of L1 specimens

Six L2 type specimens were tested (Fig. 3.9a). The shear stress at which adhesion was lost ranged from 0.69 MPa to 1.55 MPa, corresponding to 33–76% of the average maximum interface shear stress. The average shear stress at the loss of adhesion was 1.12 MPa. After a slight reduction, the shear stress increased rapidly. The average maximum shear stress for L2 specimens was 2.03 MPa, the highest among P, L1, and L2 specimens. The average slip at which the first connector failed was 3.62 mm, the lowest of the three specimen types. Transitions between interface behaviour stages were consistent with those observed in P and L1 specimens.

Unlike specimens P and L1, the crack width of the L2 specimens increased almost linearly from the start of loading until the last connectors were sheared (Fig. 3.9b). The largest final crack width at the largest slip (8 mm) was 78% greater than the widest crack in L1 specimens.

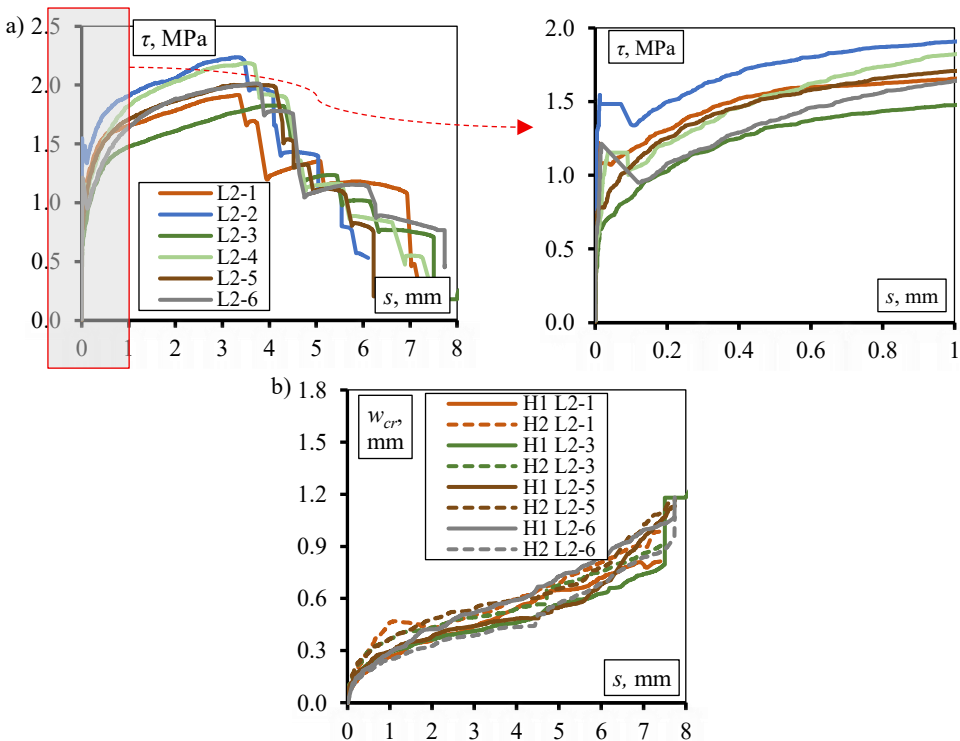


Fig. 3.9. Interface behaviour curves: a) shear stress–layer slip relationship and b) crack width–layer slip relationship of L2 specimens

Two specimens with interfaces shaped as shear keys were tested (Fig. 3.1d). The experimental results are summarised in Table 3.5. After the formation of the first cracks (end of the first behaviour stage), the interfaces began to slip rapidly (Fig. 3.10a). The shear stress increased and then dropped slightly when separation between the layers occurred, indicating the loss of adhesion. A crack developed between the interlocking shear keys along the interface, and an additional crack formed at the bottom of the upper shear key of the second layer. Both specimens exhibited the same cracking pattern, shown in Figure 3.11. Following separation, the shear stress continued to rise, reaching 3.65 MPa for specimen S-1 and 4.01 MPa for specimen S-2. After peak capacity was reached, all shear keys of the second layer were sheared off, causing a reduction in shear stress. This marked the end of interlock action and the completion of the second behaviour stage. The shear keys failed due to the lower concrete strength of the second layer. Once the keys had sheared off, the shear stress values at both interfaces became similar. After this point, distinguishing between the third and fourth behaviour stages is difficult, as only a decrease in shear stress is observed. The first connector in specimen S-1 failed at a shear stress of 1.77 MPa and a slip of 5.12 mm, while in specimen S-2 it failed at 1.90 MPa and 6.81 mm.

The crack widths of specimens S were the highest among all types of specimens (probably because of high interface roughness after shear key failure) and the growth of crack widths was almost linear (Fig. 3.10b). Similar to specimens P, due to the same connector arrangement, the crack width at the top of the interface was greater than at the middle.

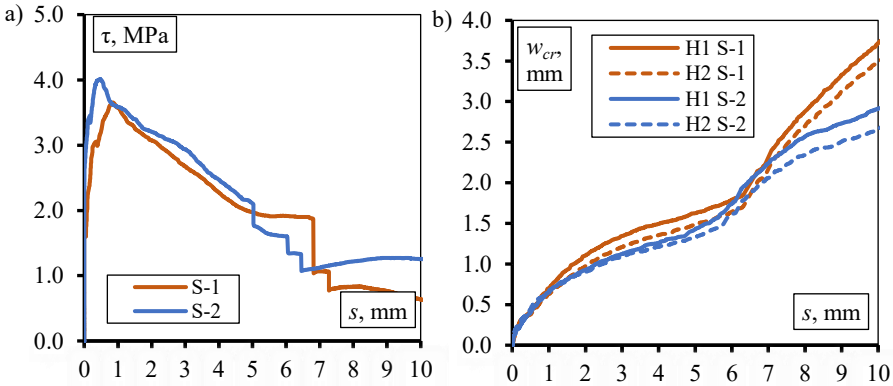


Fig. 3.10. Interface behaviour curves: a) shear stress–layer slip relationship and b) crack width–layer slip relationship of S specimens

Table 3.5. Interface shear stress and slip of experimental push-off specimens S

Specimen	τ_1 , MPa		τ_2 , MPa		τ_3 , MPa		s_2 , mm		s_3 , mm		Failure mode
S-1	1.72	2.15	3.05	3.25	3.65	3.83	0.37	0.27	0.85	0.66	Shear keys failure
S-2	2.57		3.44		4.01		0.16		0.47		Shear keys failure

In this table τ_1 – shear stress, at which the first crack formed; τ_2 – shear stress at the separation of the layers; τ_3 – shear stress at the failure of the shear keys; s_2 – slip at the separation of the layers; s_3 – slip at the failure of the shear keys.

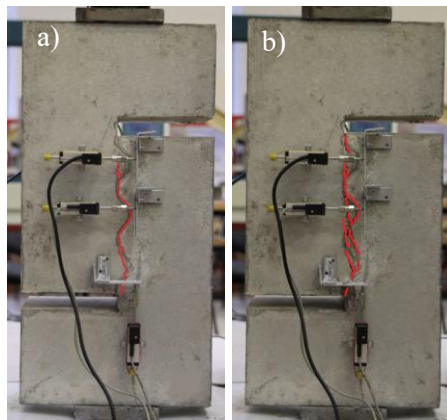


Fig. 3.11. Failure of the S specimen interface: a) appearance of the first crack and b) failure of shear keys

To properly compare the strengths and behaviours of each push-off specimen type, those exhibiting shear stress and slip values closest to the average within their category were selected (Tables 3.3 and 3.4). For this task, specimens P-2, L1-4, and L2-6 were selected. Out of two specimens with shear keys, specimen S-2 was chosen randomly. Figure 3.12 shows the interface behaviours of these specimens.

When comparing the diagrams, specimen S exhibited the highest interface shear capacity, which was approximately three times that of a smooth-interface specimen. Unlike specimens P, L1, and L2, specimen S reached its peak shear

capacity without any contribution from connectors, which is typical for rough or mechanically interlocked interfaces. The point at which the shear keys failed in specimen S corresponds to the point of adhesion loss in specimens P, L1, and L2, as in both cases, the concrete-to-concrete bond capacity is fully exhausted. At this stage, specimen S showed a notably more ductile behaviour, experiencing larger slip values than the other specimen types. Experimental results from this study and findings reported in the literature indicate that concrete bonds in non-smooth interfaces fail at higher slip values (Barbosa et al., 2017; Rizkalla et al., 1989; Semendary et al., 2020; Sørensen et al., 2017), whereas smooth interfaces typically lose cohesion at much smaller slips (Liu et al., 2019, 2021; Shaw & Sneed, 2014). The slip at which the first connector failed in specimen S was comparable to the other specimens, as the geometry of specimen S does not significantly alter connector-governed behaviour.

Despite some of its advantages, the shear-key interface geometry is not readily applicable to layered concrete beams or slabs and is more suited to precast wall connections. The shear-key configuration also introduces disadvantages, including less predictable crack development. In the present tests, the interface crack propagated into the surrounding concrete, causing local spalling, a behaviour not observed in specimens with smooth interfaces.

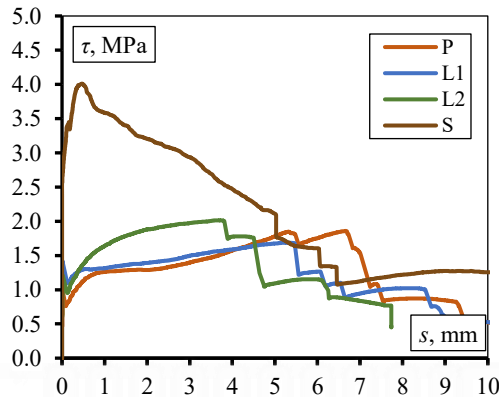


Fig. 3.12. Shear stress–layer slip relationship of every specimen type

The specimens P, L1, and L2 had similar geometries and behaviours, enabling a direct comparison. After adhesion failure and a slight drop, all three specimen types exhibited an increase in shear stress. This rapid post-adhesion increase is not commonly reported in the literature. In most published push-off tests (Barbosa et al., 2017; Fang et al., 2020; Figueira et al., 2016; Júlio et al., 2010; Liu et al., 2019, 2021; Shaw & Sneed, 2014), the shear-stress rise associated with the fourth behaviour stage typically occurs only at larger slip values or is absent. In

the present tests, the early increase in shear stress is attributable to the low connector ratio: the small-diameter connectors enter strain hardening at relatively small interface slips.

For a better understanding of the behaviours of interfaces P, L1, and L2 with different connector arrangements, it is essential to discuss the behaviours of the connectors themselves (Fig. 3.2). The horizontal connectors A of specimen P primarily resist bending. Connectors B of specimen L1 are under bending, but are also more under tension. Connectors C are not as effective as connectors A or B, making their contribution less significant. In the end, it could be said that the connectors of specimen L1 mainly resist tension. The connectors of specimen L2 are bent (A) and under tension (B).

Even though interface adhesion/interlock resistance is primarily governed by concrete properties, it is believed that the connector arrangements influenced the interface adhesion/interlock resistance. Specimens L1 and L2 demonstrated the highest interface adhesion/interlock resistances. These specimens had some connectors inclined in the direction of the shear force, placing them under tension. Connectors working in tension are therefore considered most effective during the adhesion/interlock stage. Connector configuration also affected crack-width development (Figs. 3.6b, 3.8b, 3.9b, 3.10b). In specimens P and S, most connectors were predominantly subjected to bending, which resulted in the largest crack widths. This configuration also caused the crack at the top of the interface to be wider than at mid-height. Specimen P exhibited the lowest adhesion resistance, consistent with its connector arrangement being highly susceptible to bending. Specimen L1 had connectors that were affected by bending the least and developed the smallest crack widths.

Specimen L2 experienced the most rapid increase in shear stress compared to specimens P and L1, ultimately reaching the highest value among the three (Fig. 3.12). However, the connectors of specimen L2 began to fail at the smallest slip values, leading to the soonest complete interface failure. Specimens P and L1 exhibited similar shear stress values at the stage when the connectors took over the shear transfer. Specimen P demonstrated a higher shear stress at which the connectors failed. Up to the point of connector failure, the shape of the P specimen curve resembled a “saddle”, while the shape of the L1 curve was more linear, and the L2 curve resembled a “hill”. These distinctions between the P, L1, and L2 specimens are attributed to the arrangement of their interface connectors. Figure 3.2 illustrates the angles with the interface plane that result from these specific arrangements. A Eurocode 2 equation (Eq. 3.1) is used for this analysis, since it considers connector inclination (European Committee for Standardization, 2023).

$$\tau_{Rdi} = c_v \sqrt{f_c} + \mu_v \sigma_n + \rho f_y (\mu_v \sin \alpha + \cos \alpha). \quad (3.1)$$

Although Eq. 3.1 contains several variables, only the term $\mu \sin \alpha + \cos \alpha$ is relevant here because concrete tensile strength, connector strength, and connector ratio were identical for all specimens. This term directly reflects the influence of connector inclination on the shear resistance when connectors govern the interface behaviour. Using the inclination angles from Figure 3.2 and a friction coefficient $\mu = 0.6$ (ECS, 2006) for the smooth interfaces of specimens P, L1, and L2, the corresponding multipliers were calculated as 1.20, 1.19, and 1.42, respectively. These values confirm that specimen L2 should exhibit the highest connector-governed shear resistance. They also show that greater connector inclination in the direction of the applied shear force increases the interface shear resistance in this stage. Model Code 2010 states that during dowel action, when the connector, due to bending, reaches significant inclination, an additional component resisting tensile forces is generated (Fib Model Code for Concrete Structures 2010, 2013). It appears that the L2 specimen is the most susceptible to this phenomenon, known as the kinking effect. This is clearly illustrated in Figure 3.12. The similar shear stress values of specimens P and L1 are likewise consistent with their nearly identical multiplier values. For specimen S, the response after adhesion loss is governed primarily by interface friction.

3.2. Experimental Investigation of Layered Concrete Beams

Six experimental layered concrete beams were constructed and tested for the analysis of layered concrete elements under bending and the validation of the proposed flexural stiffness approach, presented in the Second Chapter. Beam geometry is shown in Figure 3.13. The objective of the selected geometry was to evaluate the flexural behaviour at the lattice–girder region of filigree slabs, the interface zone crossed by connectors. This region is particularly relevant in semi-precast slabs incorporating void formers (Fig. 3.14). Each beam consisted of two concrete layers: the bottom layer (the first casting) and the upper layer (the second casting). The beams were categorised by interface connector arrangement: type P with connectors perpendicular to the interface, type L1 with connectors inclined relative to the interface, representing a lattice–girder configuration, and type L2 with an alternative lattice–girder arrangement. Figure 3.13 also indicates the longitudinal spacing of the connectors at the points where they intersect the interface. For each connector type, two-layer height subtypes were produced. The total height of all beams was 250 mm. All beam types are summarised in Table 3.6.

Table 3.6. Categorisation of layered concrete beams

Specimen	P-50	P-80	L1-50	L1-80	L2-50	L2-80
Connector arrangement	Perpendicular to the interface	Perpendicular to the interface	Lattice girder type	Lattice girder type	Lattice girder type	Lattice girder type
Height of concrete layers (mm)	50/200	80/170	50/200	80/170	50/200	80/170

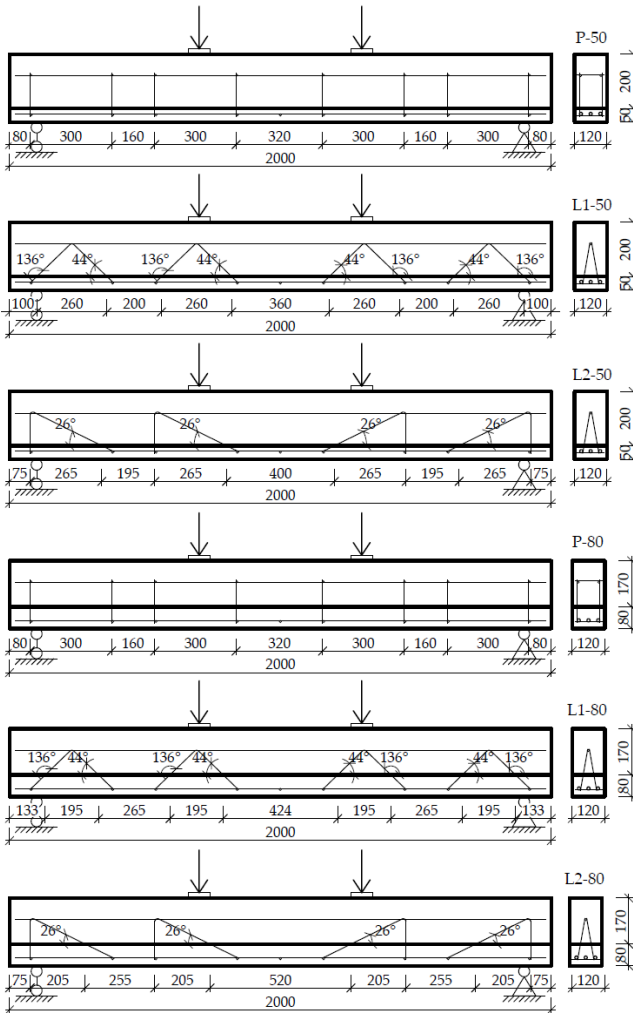


Fig. 3.13. Types and dimensions of the beams

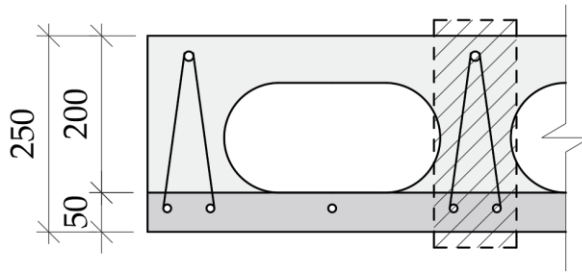


Fig. 3.14. Relevant section in the layered concrete slab

Typical normal-weight concrete was used for the layered beams. The concrete strengths of the two layers differed to reflect the conditions of semi-precast (filigree) slabs, where the first layer is factory-produced and typically stronger, and the second layer is cast on site and generally weaker. Concrete compressive strength and elastic modulus for each layer were determined at the time of beam testing using 150 mm × 300 mm cylinders. Flexural tensile strength was obtained from three-point bending tests on prisms with a cross-section of 100 mm × 100 mm, a length of 400 mm, and a span of 300 mm. Concrete consistency was evaluated using slump tests. The material properties of each layer are summarised in Table 3.7. Concrete prisms were also used to measure the shrinkage of both layers, using a mechanical strain gauge (Fig. 3.15). The measured shrinkage values are presented in Figure 3.15. The average temperature and humidity at which the prisms were stored were 19.8 °C and 58%, respectively.

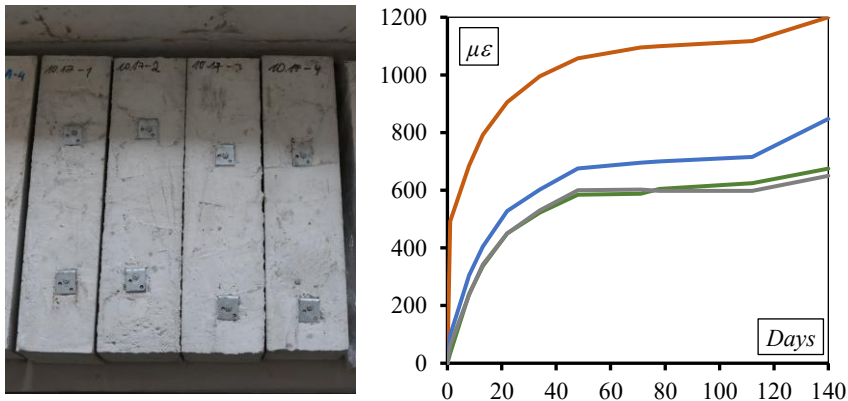


Fig. 3.15. Concrete prisms and the recorded free shrinkage values

Table 3.7. Concrete characteristics of the two concrete layers

Layer	Compressive strength on the day of tests, MPa	Flexural strength on the day of tests, MPa	Elastic modulus, GPa	Slump class
First layer	39.4	5.1	27.3	S3
Second layer	25.3	4.3	21.8	S3

The resulting interface between the layers had dimensions of 120 mm × 2000 mm. In all beams, the interface was reinforced by 16 connectors, each with a diameter of 3 mm. The interface connector ratio for half of the interface (from the highest shear stress to shear stress equal to zero) was equal to 0.047%. The layered beams were also reinforced by three flexural bars of 12 mm reinforcement at the lower (first) layer. The concrete cover was 25 mm. The upper (second) layer in beams P had two bars, and in beams L1 and L2, one bar of 8 mm flexural reinforcement. The average yield stress of the 3 mm bar was 251 MPa, the yield stress of the 12 mm bar was 591 MPa and for the 8 mm bar the declared 500 MPa was considered. Elastic modulus for the bars was 25 GPa for the 3 mm bar, 170 GPa for the 12 mm bar and 200 GPa for the 8 mm bar.

The casting interval between the two concrete layers was 78 days. The surface of the first layer was smoothed prior to hardening. During curing, the first layer was neither covered with a membrane nor intentionally moistened. This was done to accelerate shrinkage and to obtain a more pronounced differential shrinkage effect.

The beams were tested in a four-point bending setup, as shown in Figure 3.16. The displacement-controlled loading method was chosen to effectively capture the brittle failure of the beam, which was expected to result from interface failure. The displacement rate was 0.5 mm/min. Figure 3.16 presents the locations of displacement transducers. LVDT1 (resolution ∓ 0.01 mm) measured the mid-span beam deflection, LVDT2 and LVDT3 (resolution ∓ 0.001 mm) measured the deflection at the supports, and LVDT4 and LVDT5 (resolution ∓ 0.001 mm) measured the relative layer slip. Furthermore, for an additional deformation measurement, digital image correlation was used. The beams were painted white, marked with black dots and photographed throughout testing. The photos were uploaded to a dedicated software, Zeiss Correlate, and deformations were determined.

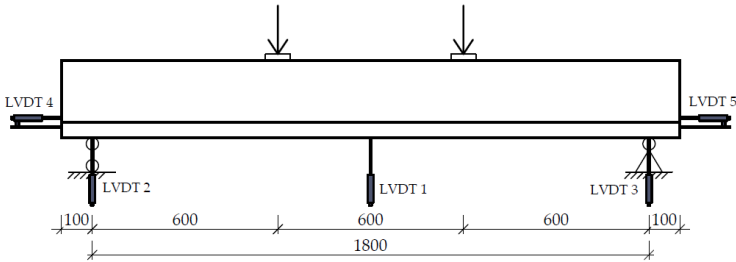


Fig. 3.16. Beam testing setup and deformation measurement

All six of the layered concrete beams failed due to interface failure, and layer slipping occurred. Generally, the beams failed in the following sequence: normal cracks developed at the first layer (the end of the first layered element behaviour stage and the beginning of the second one), a horizontal crack developed at the interface, and normal cracks developed at the second layer (these events mark the third behaviour stage). However, the intensity of each type of cracking varied among the three beam types. Figure 3.17 presents the load–deflection curves of all beams, showing deflection at beam midspan. In this figure, point A corresponds to the end of the first and the beginning of the second behaviour stage, and point B corresponds to the end of the second and the beginning of the third behaviour stage. Adhesion/interlock failure of the interface occurred at load levels between 25.1 kN and 44.3 kN. At this stage, high interface shear stresses caused failure of the adhesive and mechanical interlock mechanisms, resulting in a drop in applied load. In the third behaviour stage, as friction and dowel action began contributing to interface shear resistance, the load increased again.

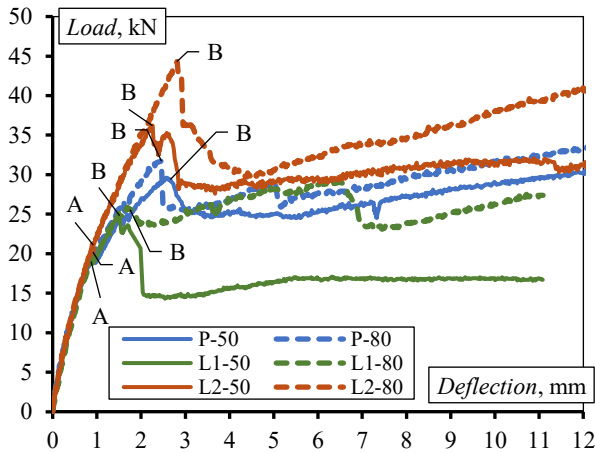


Fig. 3.17. Experimental load–deflection curves of layered concrete beams

The comparison of the experimental results for beam types P, L1, and L2 shows that beams L2 exhibited the highest flexural capacity up to the point of interface adhesive failure. These beams also maintained higher capacity after adhesion loss (with the exception of beam L2-50, which was slightly exceeded by beam P-80 at large deflections). Beams P demonstrated the second-highest flexural resistance up to adhesive failure. At the third behaviour stage, the flexural capacities of beams P, L1-80, and L2-50 were similar. The lowest adhesive interface capacity was observed in beams L1. The diagrams also show that beams L1-50 and L1-80 behaved differently at the third behaviour stage; beam L1-50 in particular exhibited notably lower load levels. This behaviour is explained in subsequent sections. It is believed that the highest flexural capacity of L2 beams is the result of their interface connector arrangement. The experimental results of the other two beam types are also affected by their respective interface connector arrangements. High adhesive interface resistance and high resistance after adhesive failure for specimen L2 were determined in the author's previous study of experimental push-off specimens in Section 3.1. The difference between experimental P and L1 beam results and push-off specimen results might have been derived from significantly different connector inclination angles, comparing current beam specimens and push-off specimens, presented in Section 3.1. In the previous section of this dissertation, a part of an equation from Eurocode 2 (European Committee for Standardization, 2023) was used to investigate the influence of connector angle inclination on interface shear resistance. The relevant segment of the equation is $\mu \sin \alpha + \cos \alpha$, where μ represents the friction coefficient, taken as 0.6 for smooth interfaces, and α – connector inclination angle (Fig. 3.13). When this expression is used over half of the beam length, the resulting values for beams P, L1, and L2 are 4.80, 3.34, and 7.05, respectively. These values are consistent with the experimental results, confirming that beam L2 had the highest interface shear capacity, followed by beams P and L1. The earlier conclusion applies: a greater connector inclination in the direction of shear force increases the contribution of the connectors to interface shear resistance.

A comparison between beams with thinner and thicker bottom layers (P-50, L1-50, and L2-50 versus P-80, L1-80, and L2-80) shows that beams with a thicker first layer achieved higher capacity before interface adhesive/interlock failure. This increase is attributed to the higher flexural stiffness of the composite cross-section: the first layer had greater compressive strength than the second layer, and in the beams with first layers of 80 mm, it occupied a larger proportion of the total section depth. At the third behaviour stage, beams with thicker first layers again demonstrated higher capacity. Once the layers began to slip and behave more individually, the deeper and stronger first layer of the 80 mm beams contributed more significantly to flexural resistance than the thinner first layers of the 50 mm beams.

The cracking patterns provide essential information on beam behaviour. In beams L2, due to the latest interface failure, initial flexural cracks propagated through both layers. Once the interface cracked, crack growth in the first layer reduced, while crack development in the second layer increased. In beams P, flexural cracks formed in the first layer but did not significantly extend into the second layer until interface cracking occurred. In beams L1, where interface failure occurred the earliest, flexural cracking in the first layer was the least developed. All these differences are attributed to different interface connector arrangements.

The interface crack in beams P-50, L1-50, L2-50, and L2-80 did not propagate along the full interface length. In contrast, beams P-80 and L1-80 exhibited interface cracking along the entire interface. The load and deflection at which the crack reached the second end of the beam were 29.0 kN (5.03 mm) for P-80 and 29.1 kN (6.49 mm) for L1-80 (Fig. 3.17). Once full-length cracking occurred, the load dropped. The primary cause was the increased interface shear stress resulting from the interface being located closer to the centroid of the composite section. However, this behaviour was not observed in beam L2-80. To explain this difference, the connector–interface crossing points in beams with thicker (80 mm) and thinner (50 mm) first layers within the same beam category were compared. In beam L2-80, the interface shifted upward by 30 mm relative to beam L2-50, causing the crossing points to move further toward the beam ends, where shear stresses are highest, thereby enhancing reinforcement in this region. In contrast, the crossing point locations in beams P-80 and L1-80 remained essentially unchanged. In beam L1-80, half of the crossing points shifted toward the beam ends while the other half moved away, resulting in no net positional change. All these aspects can be seen in Figure 3.13. An additional anomaly was observed in beam L1-50, which showed a significant load drop after adhesive failure and a notably low capacity in the third behaviour stage. This resulted from the sudden formation of a wide diagonal crack (0.77 mm near the interface) in the second layer immediately after adhesive failure. This crack propagated rapidly toward the loading point and did not occur in other beams. Crack widths near the interface were 0.66 mm for P-50 and 0.56 mm for L2-50. Examination of beam drawings and digital image correlation analysis results indicated that cracks in beams L1-50 and P-50 did not cross interface connectors, explaining the larger crack widths compared with L2-50. Figure 3.18 presents the cracking patterns after adhesive failure for all beams.

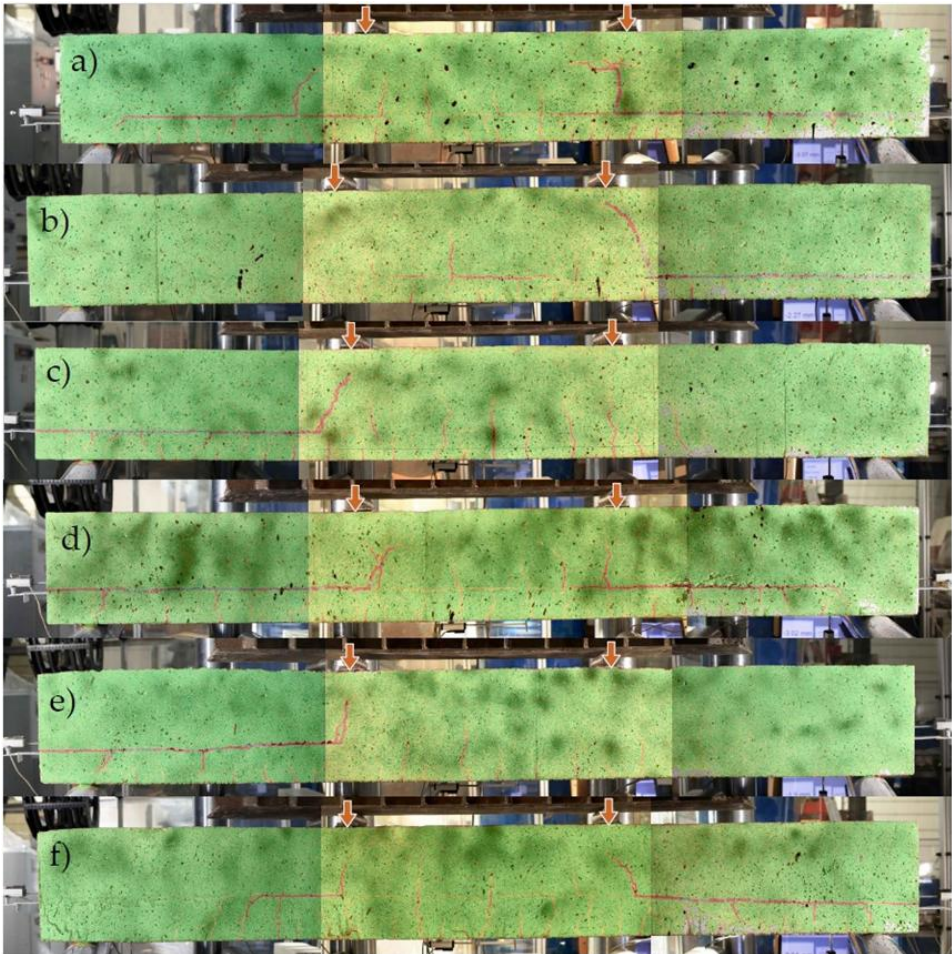


Fig. 3.18. Cracking patterns of (a) P-50, (b) L1-50, (c) L2-50, (d) P-80, (e) L1-80 and (f) L2-80 beams at the beginning of the third behaviour stage

The interface behaviour was identified as the primary factor governing the flexural behaviour of the layered concrete beams. Interface shear stress–slip curves are presented in Figure 3.19. The L2 interfaces exhibited the highest adhesive shear resistance (0.66 MPa and 1.02 MPa), followed by P (0.56 MPa and 0.74 MPa) and L1 (0.47 MPa and 0.59 MPa). The same hierarchy remained after adhesion was lost. As previously discussed, this behaviour is attributed to the connector inclination angles. The connector arrangement directly affects the interface shear stress–slip relationship: greater inclination in the direction of shear increases connector contribution and overall interface capacity. Layer separation

at the second end of the beam for P-80 and L1-80 can be seen at slips 0.99 mm and 2.11 mm, respectively (Fig. 3.19). At these points, a drop in shear stress can be observed. It can be concluded that the L2 interface connector arrangement causes the highest interface shear resistance and stiffness and as a result the overall highest flexural capacity and stiffness of the layered concrete beam.

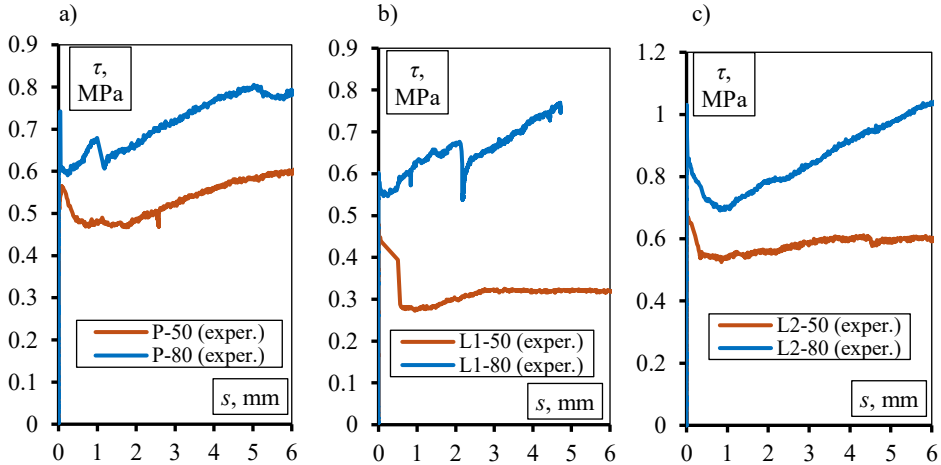


Fig. 3.19. Interface shear stress-slip relationship curves: of a) P beams; b) L1 beams; and c) L2 beams

3.3. Experimental Investigation of Semi-Precast Concrete Slabs with Plastic Void Formers

Layered concrete (filigree) slabs were produced for experimental analysis. Each slab consisted of two concrete layers cast at different times. The first layer was a 50 mm precast concrete slab manufactured at a factory. The second layer was a 210 mm cast-in-place concrete layer. Plastic void formers were used to create internal voids within the upper layer. Each void former was 140 mm in height and 315 mm in diameter. The cross-sectional dimensions of the slabs were 1.20 m × 0.26 m. Slabs of two different lengths were produced: a span of 4.98 m (S-1 slab) and a span of 2.70 m (S-2 slab) (Fig. 3.20). The corresponding quantities of plastic void formers were 39 and 21 units. The incorporation of void formers reduced the self-weight of S-1 by 0.90 t (22%) and of S-2 by 0.48 t (21%). The concrete volume was reduced by 0.36 m³ and 0.19 m³ for S-1 and S-2, respectively.

Normal-weight concrete was used for both layers. The mechanical properties of the concretes are summarised in Table 3.8. Compressive strength was determined using standard cylinder tests (300 mm × 150 mm) and cube tests (100 mm ×

100 mm × 100 mm). The elastic modulus was obtained from cylinder tests. Tensile strength was calculated following the recommendations of Eurocode 2 (ECS, 2006).

Table 3.8. Concrete characteristics of the two concrete layers

Layer	Compressive strength on the day of experiments, MPa	Tensile strength on the day of tests, MPa	Elastic modulus, GPa	Slump class
First layer	51.4	3.7	36.0	S3
Second layer	44.3	3.3	35.3	S3

Diameters and locations of the reinforcement and interface connectors are provided in Figure 3.20. The interface between the two concrete layers was crossed by 5 mm diameter interface connectors. The experimentally determined average yield stress of the connectors was 582 MPa, and the average elastic modulus was 167 GPa. The average yield stress and elastic modulus of the 10 mm flexural reinforcement were 561 MPa and 186 GPa, respectively. The corresponding values for the 12 mm reinforcement were 558 MPa and 182 GPa. The interface connector ratio, calculated for half of the interface (from the point of maximum shear to the point of zero shear), was 0.131%.

The second concrete layer was cast 82 days after the first. A large casting interval was intentionally selected to generate a pronounced differential shrinkage effect. The surface of the first layer was smoothed, producing a smooth concrete interface. The first layer was stored under relatively dry conditions and was not protected with a curing membrane, which accelerated moisture loss and shrinkage. The construction process of layered concrete slabs is shown in Figure 3.21. It was assumed that the first layer had completed its shrinkage by the time the second layer was cast. Application of the proposed differential shrinkage model (Section 2.1) shows that the shrinkage strain of the first layer does not need to be considered if its shrinkage process has finished before casting of the second layer. Therefore, only the shrinkage of the second layer was measured. This was carried out by monitoring the free shrinkage of prisms cast from the same concrete used in the second layer.

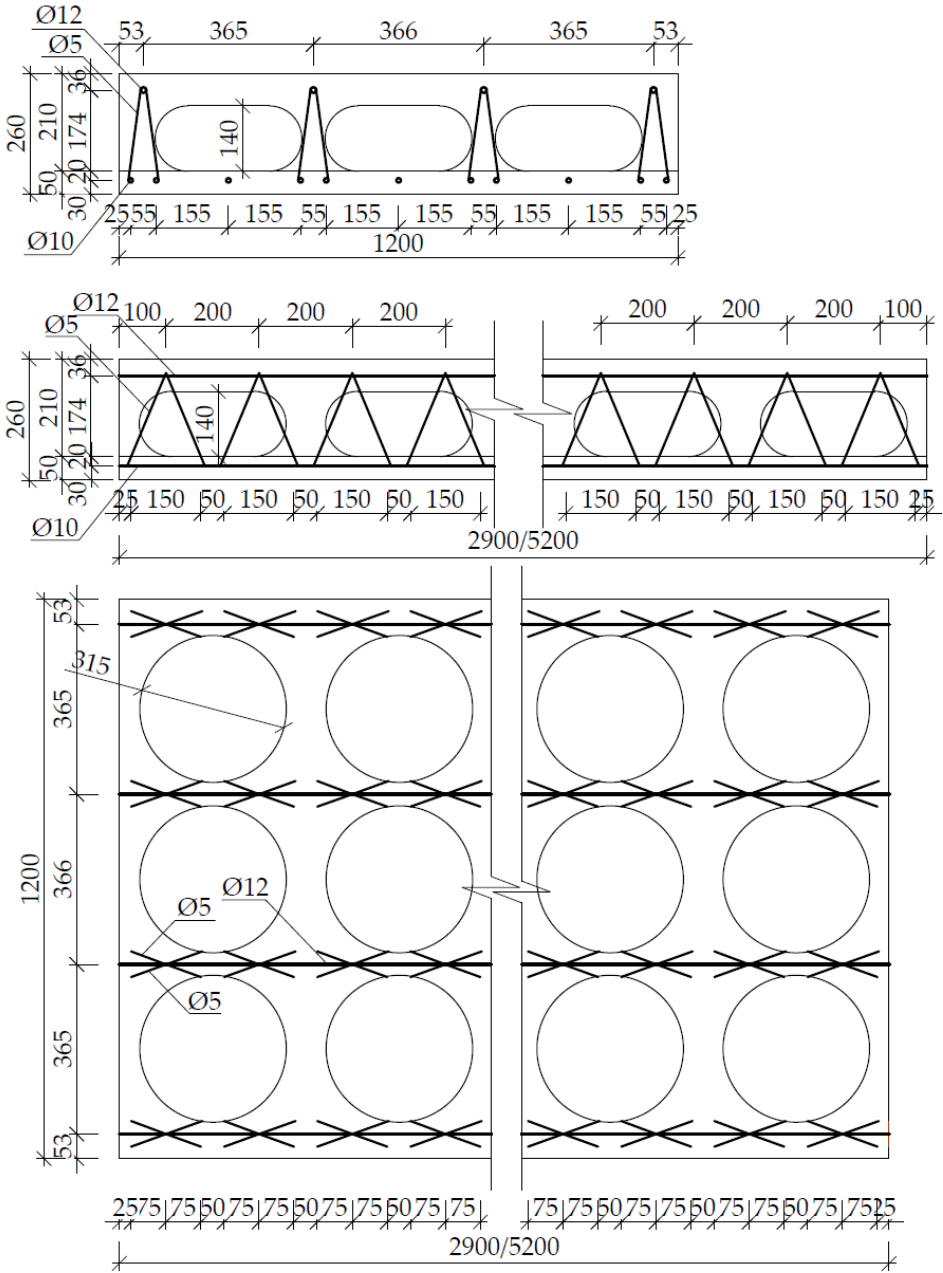


Fig. 3.20. Geometry of layered concrete slabs



Fig. 3.21. Construction process of layered concrete slabs

Layered concrete slabs were tested under a four-point bending configuration, as shown in Figure 3.22. Displacement-controlled loading was applied at a rate of 1.5 mm/min. The locations of the displacement transducers are presented in Figure 3.22. LVDTs were installed on both sides of the slabs, except for LVDTs 15 and 16, which were placed only on one side. LVDTs 1 and 2 measured mid-span deflection; LVDTs 3–6 measured deflection under the loading points; LVDTs 7–10 measured support displacements; LVDTs 11–14 measured layer slip at both slab ends; LVDTs 15 and 16 measured layer slip 560 mm from the supports. LVDTs 7–16 had a resolution of ± 0.001 mm, and LVDTs 1–6 had a resolution of ± 0.01 mm. Digital image correlation (DIC) was additionally used to measure deflection, layer slip, and cracking. The slabs were photographed during testing, and the photos were imported into dedicated software Zeiss Correlate, where the DIC analysis was performed.

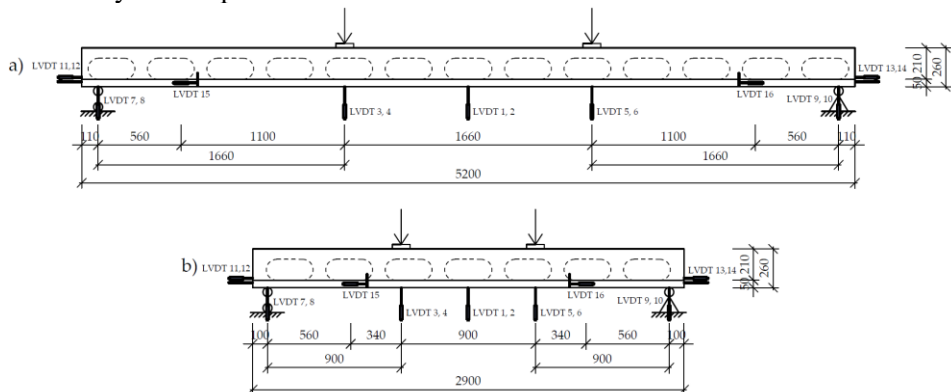


Fig. 3.22. Layered slab testing arrangements: a) slab S-1; and b) slab S-2

The test of the longer slab (S-1) was terminated at a load of 142.8 kN due to excessive deflection (152.8 mm). The load–deflection curves of both slabs are presented in Figure 3.23, showing deflection at slab midspan. The test of slab S-1 was terminated during the yielding of the flexural reinforcement. As the load increased, vertical normal cracks formed. Figure 3.24 shows the cracking pattern of the slab at a load of 141.1 kN. Since cracking beyond the loading points was negligible, only the region of the highest bending moment is presented.

For both slabs, layer slip was recorded at a distance of 560 mm from the supports using LVDTs 15 and 16 (Fig. 3.22). No slip was recorded by LVDTs 11–14; therefore, their data are not shown. The reason why layer slipping might be measured by LVDTs 15 and 16 and not recorded by LDVTs at the end of the slab can be explained by the following progression: once the shear stress exceeds the adhesive resistance of the interface, an initial interface crack forms near the location of LVDTs 15 and 16 (between the supports and the loading points). Only after further development of the interface crack toward the slab ends would layer slip be measurable by LVDTs 11–14. The displacement transducers recorded almost negligible slip between the layers for slab S-1 (up to 0.05 mm). The corresponding layer slip diagrams for both slabs are presented in Figure 3.25.

The test of the shorter slab (S-2) was terminated after failure occurred in the compressive zone. The failure point was located near one of the concentrated load points. The maximum load-bearing capacity of the slab was 335.4 kN, corresponding to a deflection of 137.8 mm. The load–deflection curve for this slab is presented in Figure 3.23.

During testing, the overall behaviour of slabs S-1 and S-2 resembled that of one-way solid cross-section slabs, as both failed in a normal section. However, several characteristics typical of layered elements were observed for slab S-2. As the load increased, a wider variety of cracks developed, including vertical and inclined normal cracks, as well as small horizontal cracks along the layer interface. The cracking pattern at a load of 322.9 kN is shown in Figure 3.26. In this figure, several normal cracks are observed to change their trajectory after crossing the interface between the two layers. Additionally, interface cracks can be seen linking separate normal cracks at different layers, which is a typical feature of layered concrete behaviour. For slab S-2, a more significant layer slip was recorded, despite the crack not propagating to the slab ends. The higher slip values and a flexural behaviour more characteristic of a layered element (compared to slab S-1) resulted from the larger shear forces acting at the interface, which in turn were caused by the shorter span length of 2.7 m. A similar span (1.8 m) can be seen in layered beams (Fig. 3.13).

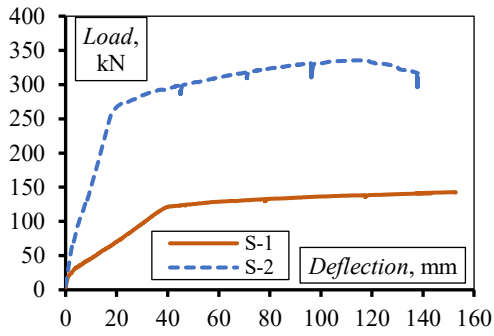


Fig. 3.23 Load-deflection curves of both slabs



Fig. 3.24. Cracking pattern of slab S-1

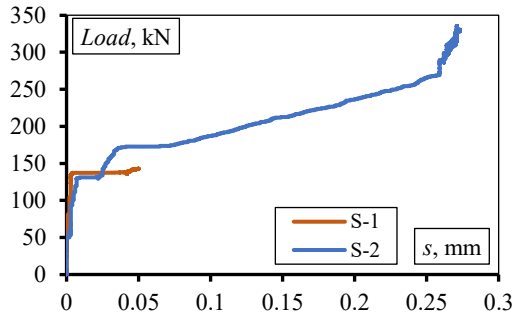


Fig. 3.25. Layer slip diagrams of both layered slabs



Fig. 3.26. Cracking pattern of slab S-2

3.4. Comparative Analysis of Theoretical and Experimental Results

3.4.1. Theoretical Interface Behaviour Model Validation

The analytical interface shear–slip model and the differential shrinkage model developed in this study were used to predict the interface behaviour of the tested push-off specimens. The shrinkage strain distribution assumed in the model is shown schematically in Figure 2.3. At the time the second layer was cast, on average, the free shrinkage strain of the first layer was $\varepsilon_{1,0} = 235 \mu\varepsilon$. By the day of testing, the free shrinkage of the first layer on average had increased to $\varepsilon_1 = 355 \mu\varepsilon$, meaning that during the interval between castings, the first layer shrank by $\varepsilon_{1,diff} = 120 \mu\varepsilon$. Over the same period, on average, the free shrinkage measured for the second layer was $\varepsilon_2 = 253 \mu\varepsilon$. The analytical procedure aims to determine the resulting differential shrinkage shear stress σ_{sh} at the interface. Using the adopted shrinkage distribution, the shrinkage strain at the centroid of the second layer was calculated as $\varepsilon_{2,y} = 406$. Differential shrinkage was therefore equal to $\varepsilon_{2,y} - \varepsilon_{1,diff} = 286 \mu\varepsilon$. Using Eq. 2.15, the resulting shrinkage shear stress was determined and was equal to $\sigma_{sh} = 1.09$ MPa. This relatively high value may be attributed to the relatively dry environment in which the layers cured, accelerating their shrinkage, and a relatively low first-layer residual shrinkage $\varepsilon_{1,diff}$, causing a higher differential shrinkage.

The proposed interface behaviour model was applied to predict the interface behaviour of push-off specimens P, L1, and L2. Specimen S was not analysed, as the model is intended for smooth or slightly rough interfaces. Figs. 3.27a, 3.27b, and 3.27c present the experimental curves together with the theoretical curves obtained using the proposed model (Eqs. 2.1–2.28). For comparison, theoretical curves excluding differential shrinkage effects are also shown. In addition, interface behaviour predictions generated using other available models (Birkeland & Birkeland, 1966; Committee for the Model Code 1990, 1993; ECS, 2006; European Committee for Standardization, 2023; International Federation for Structural Concrete (fib), 2020; Xu et al., 2015; Yang, 2016) are included to illustrate differences between existing approaches and the proposed analytical model.

Starting with the proposed interface behaviour model, the closest agreement with experimental results at the initial stages of interface behaviour (points A and B) was obtained for specimens P (Fig. 3.27a) and L2 (Fig. 3.27c). For specimen L1 (Fig. 3.27b), the theoretical predictions were

slightly less accurate at these stages. Generally, shear resistance at the adhesive resistance stage is more difficult to estimate due to less predictable chemical concrete and interface surface conditions. At later stages, the predicted shear stress values were close to the experimental results for specimens L1 and L2, and less accurate for specimen P. The model does not capture connector shearing, which must be evaluated separately; therefore, although the analytical curve matched the experimental one at point D for specimen P, significant discrepancies remained for specimens L1 and L2. At point B (adhesion failure), two theoretical values are shown: the continuous line represents calculations including shrinkage stress, and the dashed line represents calculations without differential shrinkage. For specimen P, adhesion resistance was reduced from 2.02 MPa to 0.93 MPa (54%) when shrinkage was considered; for L1, from 2.00 MPa to 0.91 MPa (55%); and for L2, from 2.32 MPa to 1.23 MPa (47%). Theoretical results indicate that differential shrinkage stress decreased the interface adhesion resistance by 47–55%. The results indicate that differential shrinkage reduced adhesion resistance by 47–55%. Point C (shear stress increase after adhesion failure) was predicted most accurately for specimen L2, which exhibited higher interface shear stiffness.

There is a notable lack of interface behaviour models describing the interface shear stress–slip relationship, which defines interface shear stiffness. Among the reviewed models, only those by Yang (2016), Xu et al. (2015), and the Model Code 1990 (Committee for the Model Code 1990, 1993) explicitly address this relationship. Other models presented in this section (Birkeland & Birkeland, 1966; ECS, 2006; European Committee for Standardization, 2023; International Federation for Structural Concrete (fib), 2020) provide only interface shear resistance values without considering interface deformation.

The shear stress–slip model by Yang (2016) was used for comparison (Fig. 3.27). Although Yang’s model achieved the highest accuracy among interface stiffness models of other authors, it was less accurate than the proposed model. The predicted adhesive resistance was close to that obtained using the proposed model when differential shrinkage was not considered, indicating that Yang’s model lacks consideration of differential shrinkage. The model also accounts for connector inclination, enabling distinct shear stress values for specimens P, L1, and L2. After adhesive failure, a drop in shear stress occurs. Yang’s model assumes that the shear stress decreases monotonically beyond this point and therefore fails to capture the subsequent stress increase observed in the fourth stage of the interface behaviour curve, likely due to the neglect of the dowel action.

An interface stiffness model from the Model Code 1990 for smooth interfaces was also tested. The predicted interface shear resistance was close to the experimental shear stress in specimen P after adhesive failure. For other specimens,

however, the accuracy was lower. Despite this, the predicted slip values were similar to the experimental measurements across all specimens. The main limitation of this model lies in its lack of detail regarding shear stress parameters and the different stages of interface behaviour.

The shear stress–slip models by Xu et al. (2015) and the Model Code 1990 (Committee for the Model Code 1990, 1993) were also evaluated. However, they produced significantly inaccurate interface behaviour predictions and were therefore plotted separately (Fig. 3.27d) to avoid distorting the scale of comparative figures. This inaccuracy arises because these models were not developed for smooth interfaces: Xu et al. applies to monolithic interfaces, while the Model Code 1990 applies to rough interfaces. These limitations reinforce the lack of reliable models capable of describing the shear stiffness of smooth concrete interfaces.

The remaining models describe only interface shear resistance, neglecting the interface slip. The Birkeland and Birkeland, based solely on clamping friction, reproduced part of the experimental behaviour of specimen P and matched portions of the L1 curve. The second-generation Eurocode 2 and the Model Code 2020 yielded identical shear resistance values for all specimens, as they neglect connector inclination for smooth interfaces. These values were nevertheless close to the adhesive resistance predicted by the proposed model. The first-generation Eurocode 2, which considers connector inclination, provided different resistance values for various connector angles; however, these were considerably higher than experimental results.

In summary, only models that account for both shear stress and slip are suitable for studying interface shear stiffness, among which the proposed model demonstrated the highest accuracy. The coefficient of determination (R^2) and root mean square error (RMSE) for all tested interface models are presented in Table 3.9. It can be observed that the proposed model demonstrated the highest R^2 and the lowest RMSE values.

The proposed analytical approach for determining the flexural stiffness of layered concrete elements was validated against experimental data reported by other authors. The interface behaviour of push-off specimens presented by Sneed et al. (2016) was predicted using the proposed interface shear stiffness model as well as other models from the literature (Fig. 3.28). Two stiffness models – the Model Code 90 (Committee for the Model Code 1990, 1993) for rough interfaces and the model by Xu et al. (2015) for monolithic interfaces greatly overestimate shear stress (as discussed in previous analysis). For this reason, they were excluded from the current interface analysis.

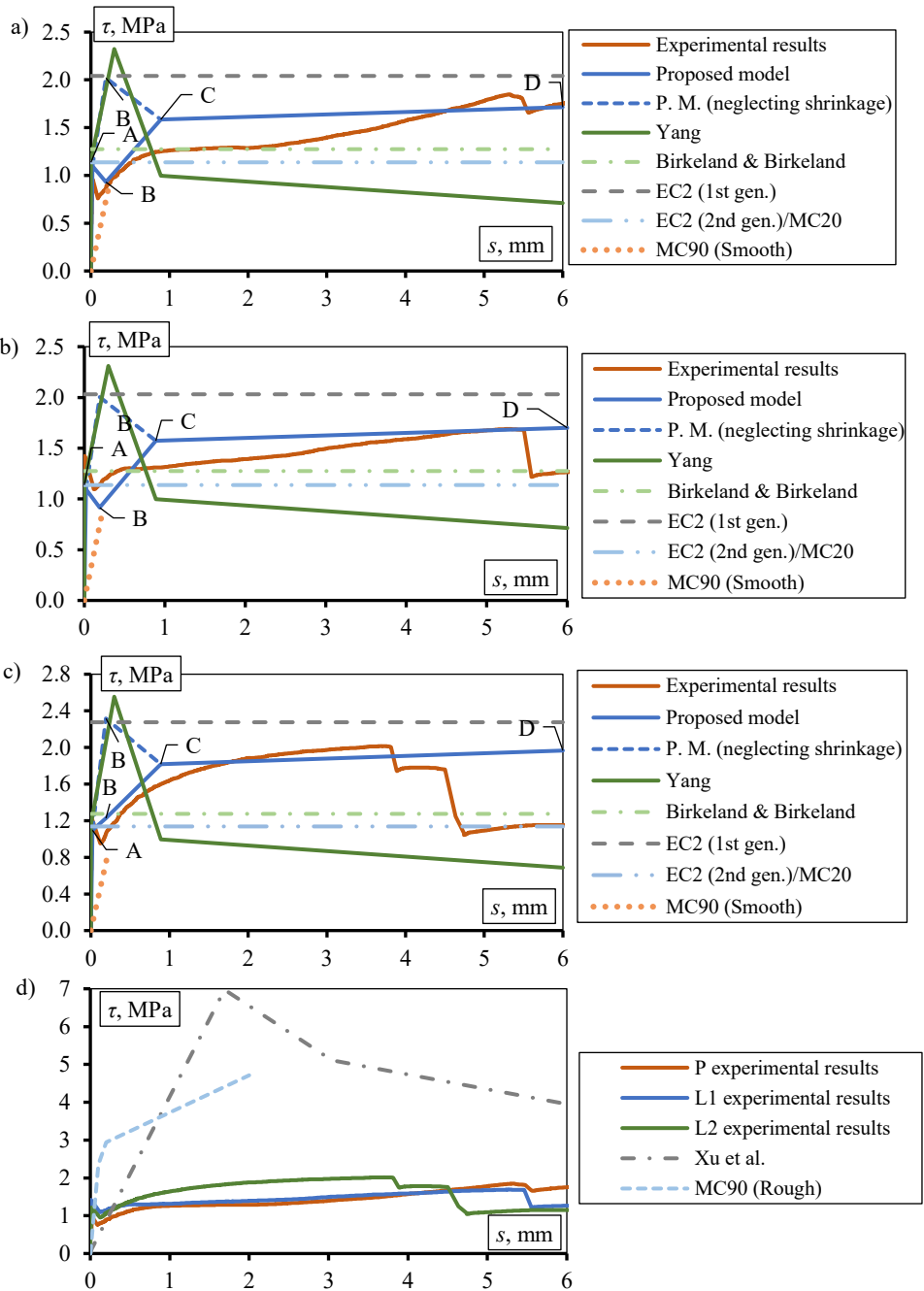


Fig. 3.27. Shear stress–layer slip relationship curves: a) of specimen P, b) of specimen L1, c) of specimen L2, and d) of all specimens and remaining interface stiffness models

Table 3.9. Error statistics for analytical vs experimental interface behaviour

Model	Error statistics	P	L1	L2
Proposed	R ²	0.94	0.86	0.80
	RMSE, MPa	0.19	0.25	0.39
Yang	R ²	0.15	0.44	0.28
	RMSE, MPa	1.10	0.60	0.76
MC90 (smooth)	R ²	0.38	0.35	0.24
	RMSE, MPa	0.44	0.95	1.02
Xu et al.	R ²	0.15	0.31	0.51
	RMSE, MPa	2.64	2.54	2.34
MC90 (rough)	R ²	0.70	0.59	0.68
	RMSE, MPa	2.10	2.00	1.80
Birkeland & Birkeland	R ²	Not defined	Not defined	Not defined
	RMSE, MPa	0.66	0.55	0.60
Eurocode 2 (1st gen.)	R ²	Not defined	Not defined	Not defined
	RMSE, MPa	1.23	1.08	1.18
Eurocode 2 (2nd gen.)/ MC20	R ²	Not defined	Not defined	Not defined
	RMSE, MPa	0.60	0.52	0.61

While many existing models achieved reasonable accuracy in describing interface behaviour, the proposed model demonstrated both close agreement with the experimental results and a higher level of detail in representing the interface behaviour. The error statistics for all tested interface stiffness models are presented in Table 3.10.

Table 3.10. Error statistics for analytical vs experimental interface behaviour

Model	Error statistics	S-CL-CJ-R-9-1	S-SL-CJ-S-13-2	S-SL-CJ-S-9-2
Proposed	R ²	0.85	0.98	0.90
	RMSE, MPa	0.78	0.39	0.73
Yang	R ²	0.50	0.32	0.17
	RMSE, MPa	1.78	2.11	1.94
MC90 (smooth)	R ²	0.81	0.84	0.84
	RMSE, MPa	2.62	2.29	2.09
Birkeland & Birkeland	R ²	Undefined	Undefined	Undefined
	RMSE, MPa	2.06	2.42	1.57

End of Table 3.10

Model	Error statistics	S-CL-CJ-R-9-1	S-SL-CJ-S-13-2	S-SL-CJ-S-9-2
Eurocode 2 (1st gen.)	R ²	Undefined	Undefined	Undefined
	RMSE, MPa	2.34	2.92	2.02
Eurocode 2 (2nd gen.) / MC20	R ²	Undefined	Undefined	Undefined
	RMSE, MPa	2.02	2.43	1.57

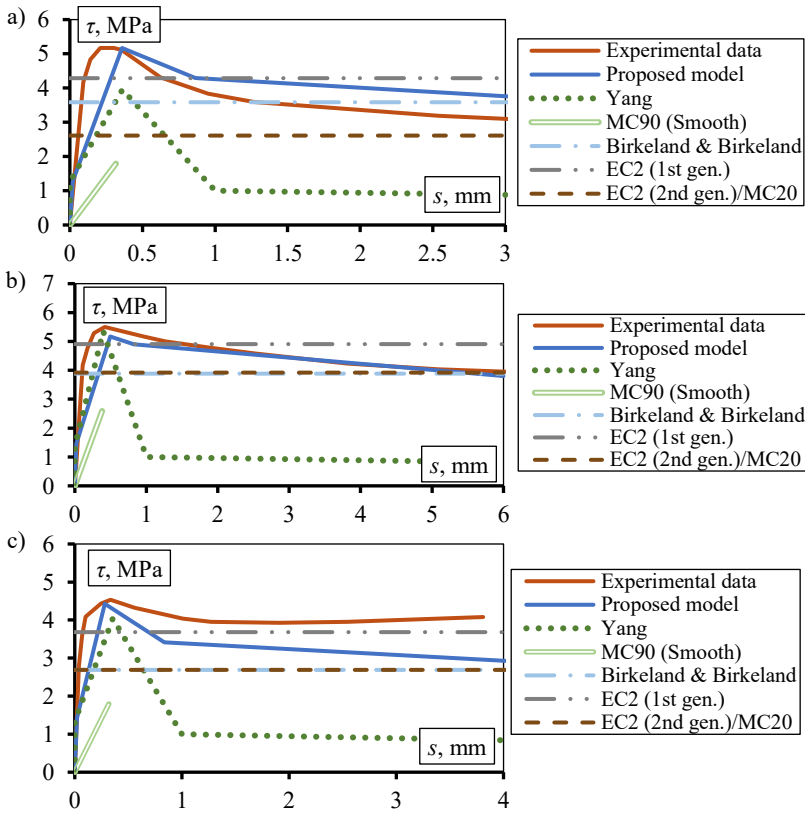


Fig. 3.28. Interface shear stress–layer slip relationship experimental and analytical curves of a) S-CL-CJ-R-9-1; b) S-SL-CJ-S-13-2, and c) S-SL-CJ-S-9-2

3.4.2. Layered Concrete Element Flexural Stiffness Model Validation

Additionally, the flexural behaviour of the layered beams was predicted using the proposed interface shear stress–slip model, the differential shrinkage model, and

the built-up layers deflection model. To obtain the deflection of each beam, the interface behaviour was first determined. Figure 3.29 compares the experimental and analytical interface shear stress–slip curves. The analytical predictions showed good agreement with the experimental results in the adhesive stage and after adhesion loss. The curves were generated using the proposed interface model (Eqs. 2.1–2.28). However, the model slightly overestimated the adhesive resistance for beams P-80, L1-80, and L2-80. For most beams, the predicted post-adhesion stress drop was larger than that observed experimentally. Additionally, because the model evaluates the interface behaviour at one end only, the reduction in shear stress caused by interface failure at the opposite end was not captured. Moreover, the model predicted an increase in shear stress in the post-adhesion stage for all beams, whereas this increase was less pronounced in beams L1-50 and L2-50. Due to the low connector ratio, the model assumes that the connectors in all specimens reach the strain-hardening stage, resulting in an increase in shear stress for all specimens.

Shear stress due to differential shrinkage was included in the calculations. Using the measured free-shrinkage values and Eqs. 2.15–2.28, the shrinkage strain components and the resulting interface shear stress were determined (Table 3.11). The shrinkage strain types referenced correspond to those defined in Section 2.1. When comparing beams with thinner first layers (P-50, L1-50, and L2-50) to beams with thicker first layers (P-80, L1-80, and L2-80), it is evident that beams with thicker first layers develop higher differential shrinkage ε_s and consequently higher interface shear stress σ_{sh} . The primary cause is the larger shrinkage of the second layer in these beams, as the lower height of this layer leads to higher shrinkage values ($\varepsilon_{2,y}$ or $\varepsilon_{2,t}$). In addition, the internal force distribution produced by differential shrinkage results in larger shear stress when the interface lies closer to the centroid of the composite section. Similarly, the values of L1 and L2 were derived from their identical flexural reinforcement (three reinforcement bars at the bottom and one at the top). This also explains the differences relative to beams P, which contain two bars in the upper layer.

When the analytical shear stress and corresponding slip values are known for all interface behaviour stages, the interface shear stiffness modulus G_{eff} is obtained directly from Eq. 2.1. The analytical values of G_{eff} are presented in Table 3.12. In this table, interface behaviour stages are represented by points 0, A, B, C, and D (Fig. 2.1). Lastly, using Eqs. 2.29–2.37, load-deflection curves of layered concrete beams were determined (Fig. 3.30).

Table 3.11. Concrete shrinkage strain and interface shrinkage shear stress

Specimen	ε_1 , $\mu\varepsilon$	ε_2 , $\mu\varepsilon$	$\varepsilon_{1.0}$, $\mu\varepsilon$	$\varepsilon_{2.s}$, $\mu\varepsilon$	$\varepsilon_{2.r}$, $\mu\varepsilon$	$\varepsilon_{2.c}$, $\mu\varepsilon$	$\varepsilon_{2.t}$, $\mu\varepsilon$	$\varepsilon_{2.y}$, $\mu\varepsilon$	$\varepsilon_{1.t}$, $\mu\varepsilon$	ε_s , $\mu\varepsilon$	σ_{sh} , MPa
P-50	843	753	751	128	286	24	315	206	93	113	0.56
P-80	843	753	751	112	286	24	331	214	93	121	0.60
L1-50	843	753	751	128	286	12	326	211	93	118	0.59
L1-80	843	753	751	112	286	12	342	219	93	126	0.62
L2-50	843	753	751	128	286	12	326	211	93	118	0.59
L2-80	843	753	751	112	286	12	342	219	93	126	0.62

Table 3.12. Relationship between interface shear stress, slip, and shear stiffness modulus

Interface characteristics	Interface behaviour points	Specimens					
		P-50	P-80	L1-50	L1-80	L2-50	L2-80
τ , MPa	0	0	0	0	0	0	0
	A	0.40	0.54	0.40	0.54	0.40	0.54
	B	0.52	0.86	0.38	0.69	0.65	1.05
	C	0.41	0.55	0.37	0.49	0.47	0.63
	D	0.64	0.87	0.58	0.78	0.74	1.00
S , mm	0	0	0	0	0	0	0
	A	0.02	0.02	0.02	0.02	0.02	0.02
	B	0.13	0.13	0.13	0.13	0.13	0.13
	C	0.92	0.92	0.92	0.92	0.92	0.92
	D	6.00	6.00	6.00	6.00	6.00	6.00
G_{eff} , GPa	0	8.70	8.70	8.70	8.70	8.70	8.70
	A	8.70	8.70	8.70	8.70	8.70	8.70
	B	4.01	6.67	2.95	5.36	5.06	8.18
	C	0.44	0.59	0.40	0.53	0.51	0.68
	D	0.11	0.14	0.10	0.13	0.12	0.17

Alongside the proposed interface stiffness model, several existing models were used to predict interface behaviour. All calculations were performed without considering beam layer thickness, as none of these models accounts for the interface location relative to the section height. Consequently, only one curve per model was generated for each beam type (P, L1, and L2) (Fig. 3.29).

The interface stiffness model by Yang (2016) substantially overestimated the interface shear stress. While incorporating differential shrinkage effects might

yield more accurate adhesive resistance values, the predicted shear stresses remained excessively high even after adhesive failure.

The smooth interface stiffness model from the Model Code 90 (Committee for the Model Code 1990, 1993) produced significantly lower shear stress values. This is likely due to the neglect of adhesive resistance, as the model considers only clamping and external compression friction at the interface. The remaining models describe only shear resistance and do not consider slip behaviour.

The model by Birkeland and Birkeland (1966), which only accounts for clamping, predicted very low shear resistance. In contrast, the first-generation Eurocode 2 (ECS, 2006) overestimated shear stress, likely due to superimposing adhesion and clamping friction mechanisms that do not act simultaneously. Among the shear resistance models, the second-generation Eurocode 2 (European Committee for Standardization, 2023) and the Model Code 2020 (International Federation for Structural Concrete (fib), 2020) produced the most accurate shear stress values. These codes recommend neglecting adhesive resistance for smooth interfaces, which resulted in analytical values that were closer to the experimental data in the post-adhesive failure stage.

In summary, the proposed interface stiffness model achieved the highest accuracy in predicting interface shear stress and slip, while also capturing multiple stages of interface behaviour. The coefficient of determination (R^2) and root mean square error (RMSE) for all tested interface stiffness models are presented in Table 3.13. The proposed model achieved the highest R^2 and the lowest RMSE values.

Table 3.13 Error statistics for analytical vs experimental interface behaviour

Model	Error statistics	P-50	P-80	L1-50	L1-80	L2-50	L2-80
Proposed	R^2	0.94	0.75	0.62	0.89	0.74	0.78
	RMSE, MPa	0.07	0.16	0.13	0.09	0.14	0.18
Yang	R^2	0.13	0.20	0.03	0.36	0.02	0.05
	RMSE, MPa	0.77	0.69	0.87	0.72	0.75	0.67
MC90 (smooth)	R^2	0.46	0.23	0.39	0.37	0.36	0.34
	RMSE, MPa	0.33	0.45	0.27	0.37	0.41	0.55
Birkeland & Birke- land	R^2	Unde- fined	Unde- fined	Unde- fined	Unde- fined	Unde- fined	Unde- fined
	RMSE, MPa	0.38	0.53	0.24	0.46	0.45	0.67
Eurocode 2 (1st gen.)	R^2	Unde- fined	Unde- fined	Unde- fined	Unde- fined	Unde- fined	Unde- fined
	RMSE, MPa	0.64	0.55	0.67	0.52	0.67	0.56

End of Table 3.13

Model	Error statistics	P-50	P-80	L1-50	L1-80	L2-50	L2-80
Eurocode 2 (2nd gen.)/MC20	R ²	Undefined	Undefined	Undefined	Undefined	Undefined	Undefined
	RMSE, MPa	0.24	0.36	0.16	0.33	0.27	0.47

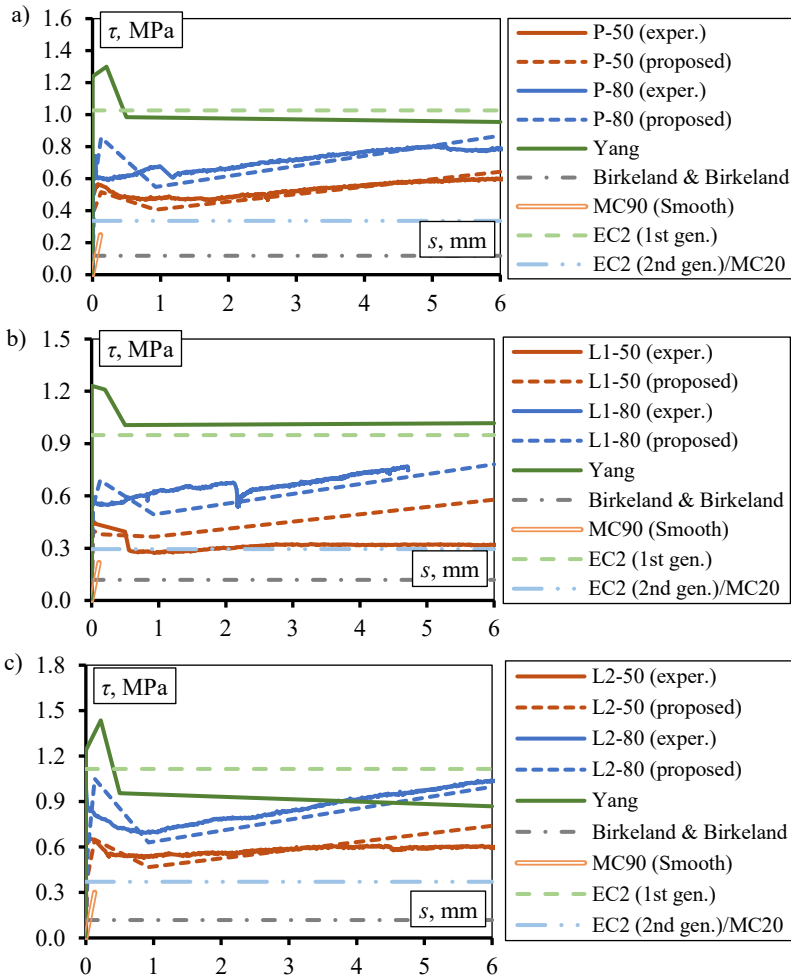


Fig. 3.29. Interface shear stress–layer slip relationship experimental and analytical curves of a) P beams; b) L1 beams, and c) L2 beams

The deflection values of a layered beam depend on the load, shear stiffness coefficient (Table 3.12) and geometrical characteristics of the layers, which in turn are affected by cracking. The analytically determined cracking moment M_{cr} (Eq. 2.39) of the composite section was lower than the bending moment, at which the interface adhesive failure occurs (determined from Fig. 3.29). This indicates that flexural cracking in the bottom layer initiated before the loss of interface adhesion. Across all beams, M_{cr} ranged from 3.91 kNm to 4.01 kNm, whereas adhesive failure occurred at bending moments from 6.94 kNm to 7.68 kNm. Following adhesive failure, the layers began to deform independently, and cracking developed in the second layer. These changes in section properties were included in the analytical deflection calculations.

The analytically determined deflection curves were generally in good agreement with the experimental results, though some deviations were observed. The analytically predicted flexural stiffness of slab P-80 was lower than the experimentally measured stiffness up to the point of interface adhesive failure. In addition, the analytical model did not capture the severe premature cracking observed in beam L1-50, which resulted in higher experimental deflections during the third flexural stage. Finally, the calculations assumed interface failure at only one beam end; therefore, the load drop recorded experimentally at 29.1 kN (6.49 mm) for L1-80 was not reproduced, and a linear load–deflection response was assumed after adhesive failure.

Models proposed by other authors (Magnucki et al., 2020; Peng et al., 2024) were also employed to predict deflection values of layered concrete beams. These models were selected to assess whether variable interfacial stiffness must be incorporated into the flexural analysis of layered concrete elements and to determine which formulation most appropriately accounts for the mechanical and geometric characteristics of the individual layers. A deflection estimation model developed by Magnucki et al. (2020) does not account for interface failure; deflections were calculated only up to the experimental load corresponding to adhesive failure. As shown in Figure 3.30, for beams L1-50 and L2-50, the predicted deflections from both the proposed model and that of Magnucki et al. were in close agreement. For beams P-50, P-80, L1-80, and L2-80, however, the proposed model produced higher deflection values (more accurate predictions), likely because it accounts for partial interface shear connection and plasticity, which is not included in the model by Magnucki et al.

The model by Peng et al. (2024) accounts for variable interface stiffness through different shear stiffness K values, referred to as G_{eff} in this study, but does not provide a procedure for determining these values. Consequently, a constant monolithic shear stiffness was assumed, and interface failure was not considered. Another limitation of Peng et al.'s model is the assumption that the layers

have identical heights and material properties. To comply with this assumption, the beams were calculated as having two 125 mm layers with averaged material properties, which resulted in overlapping analytical curves for P-50, L1-50, and L2-50 with those for P-80, L1-80, and L2-80 in Figure 3.30. This overlap illustrates the model's neglect of layer thickness effects. The resulting load–deflection curves were similar to those of Magnucki et al., determined for beams P-80, L1-80, and L2-80. It should be noted that the assumption of monolithic interface stiffness in the models by Magnucki et al. and Peng et al. resulted in lower deflection values at the interface adhesive failure stage. This demonstrates the necessity of accounting for partial interface stiffness in layered concrete elements under bending.

The coefficient of determination (R^2) and root mean square error (RMSE) for all tested flexural stiffness models are presented in Table 3.14. Since other authors' models are applicable only up to adhesive failure, the statistics for the proposed model were provided up to adhesive failure and for the whole deflection curve. At the stage up to adhesive failure, all models achieved decent R^2 values; however, the RMSE values of the proposed model were the lowest. Comparing the experimental and analytical deflection (and error statistics) values, it can be concluded that while the models by Magnucki et al. and Peng et al. are suitable for estimating layered element deflection, the proposed model offers high accuracy, a more novel approach by accounting for additional factors influencing layered element behaviour and considers element performance even after adhesive interface failure.

Table 3.14. Error statistics for analytical vs experimental flexural beam behaviour

Model	Error statistics	P-50	P-80	L1-50	L1-80	L2-50	L2-80
Proposed (up to adhesive failure)	R^2	0.99	1.00	0.95	0.96	0.97	0.97
	RMSE, mm	0.12	0.24	0.12	0.14	0.18	0.19
Mag- nucki et al.	R^2	0.95	0.92	0.93	0.93	0.96	0.97
	RMSE, mm	0.52	0.48	0.14	0.25	0.19	0.32
Peng et al.	R^2	0.98	0.97	0.99	0.99	0.99	0.99
	RMSE, mm	0.66	0.53	0.18	0.29	0.31	0.39
Proposed (entire curve)	R^2	0.97	0.98	0.99	0.73	1.00	1.00
	RMSE, mm	0.82	0.99	1.97	2.12	0.50	0.37

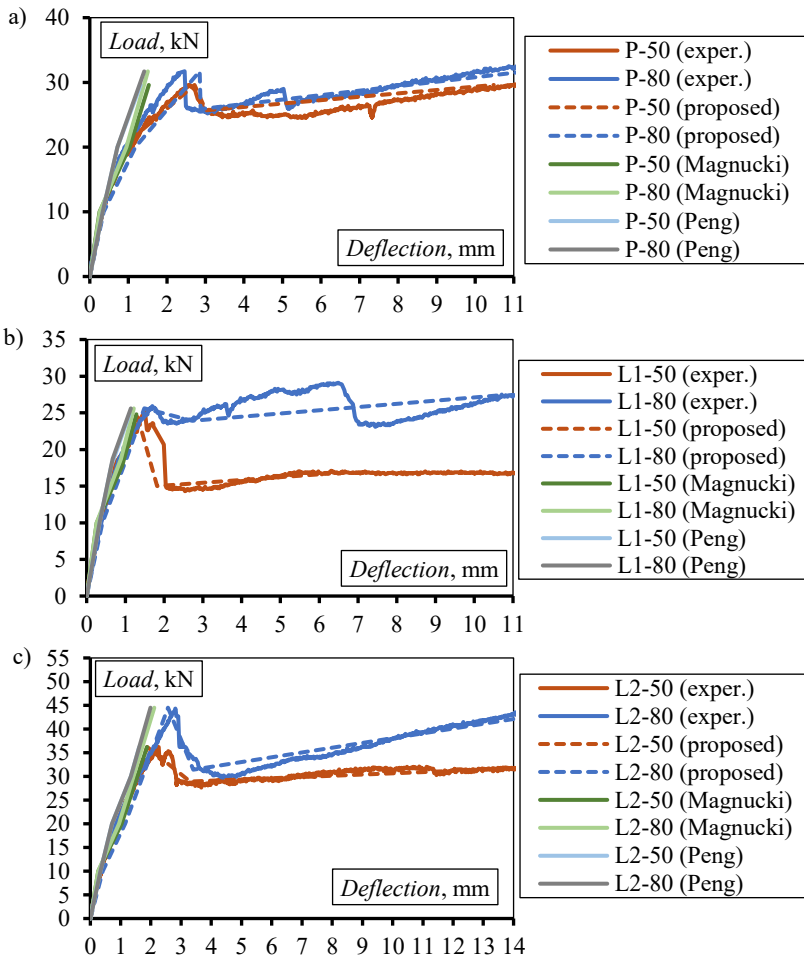


Fig. 3.30. Load–deflection experimental and analytical curves of a) P beams, b) L1 beams, and c) L2 beams

Using the proposed layered concrete element stiffness method, the interface shear behaviour and deflection of the slabs S-1 and S-2 were also evaluated. In Figure 3.31, it is shown that slab S-1 exhibited minor layer slip. The measured slippage values were likely influenced by the sensitivity of the LVDTs to slab bending. The analytical interface behaviour results indicated that S-1 did not undergo interface cracking, as the calculated adhesive resistance (0.89 MPa) exceeded the maximum experimental stress (0.55 MPa), and observed layer slip was negligible.

Slab S-1 primarily experienced significant flexural cracking, which redirected stress concentration away from the interface and into the flexural zone. In contrast, slab S-2 showed signs of interface cracking. The analytically determined adhesive failure stress for S-2 (0.70 MPa) was close to the experimental value (0.66 MPa), indicating that the analytical prediction may accurately represent the actual adhesive resistance. Beyond this point, the analytical shear stress remained nearly constant, whereas the experimentally obtained shear stress increased by approximately a factor of two. Given the relatively low connector ratio combined with the high concrete strength, the proposed model assumed that no substantial increase in shear stress should occur after adhesive failure.

The analytically determined differential shrinkage-induced interface shear stress was 0.52 MPa and 0.93 MPa for slabs S-1 and S-2, respectively. Notably, slab S-2 experienced a higher shrinkage shear stress due to its smaller interface area. The higher differential shrinkage shear stress, which reduces the adhesive resistance, is also reflected in the analytical shear stress–slip curves, where lower shear stress values were predicted for slab S-2.

Models by other authors (Birkeland & Birkeland, 1966; Committee for the Model Code 1990, 1993; ECS, 2006; European Committee for Standardization, 2023; International Federation for Structural Concrete (fib), 2020; Yang, 2016) were also used to predict the interface behaviour. Yang’s model overestimated both the interface stress and slip. The first-generation EC2 model captured the highest experimental shear stress values, whereas the second-generation EC2, MC20, and Birkeland and Birkeland models more closely matched the shear stress of initial cracking. In contrast, the MC90 model predicted significantly lower shear stress values. Based on the comparison of analytical results (Fig. 3.31) and error statistics (Table 3.15), the proposed interface stiffness model offered the most suitable combination of accuracy and detail. The model error for slab S-1 was not determined, since it did not experience interface cracking.

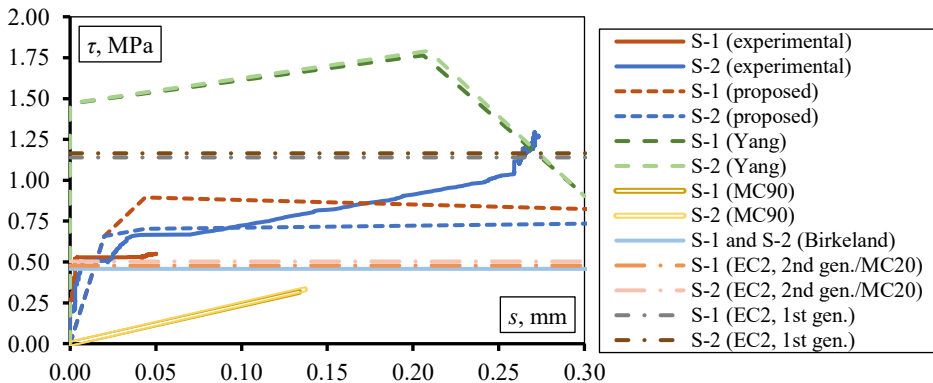


Fig. 3.31. Experimental and analytical interface behaviour curves

Table 3.15. Error statistics for analytical vs experimental interface behaviour

Error statistics	Model					
	Proposed	Yang	MC90 (smooth)	Birkeland & Birkeland	Eurocode 2 (1st gen.)	Eurocode 2 (2nd gen.)
R ²	0.70	0.53	0.60	Undefined	Undefined	Undefined
RMSE, MPa	0.26	0.98	0.43	0.46	0.71	0.45

Throughout all stages of testing, the interface of slab S-1 maintained its structural integrity. Consequently, when applying the proposed flexural stiffness model, a constant effective shear stiffness of $G_{eff} = 14.12$ GPa was used in the deflection calculations. The corresponding deflection results are shown in Figure 3.32. Based on both analytical and experimental observations, slab S-2 was expected to develop interface cracking. At the onset of interface cracking, the effective shear stiffness was analytically determined to decrease to 10.15 GPa, and this value was adopted for the stage corresponding to the slab’s highest flexural capacity. The analytical results obtained using the proposed model were in close agreement with the experimental measurements.

Table 3.16. Error statistics for analytical vs experimental flexural slab behaviour

Model	Error statistics	S-1	S-2
Proposed	R ²	0.99	1.00
	RMSE, mm	6.42	4.92
Magnucki et al.	R ²	0.82	1.00
	RMSE, mm	26.41	13.56
Peng et al.	R ²	0.80	0.99
	RMSE, mm	57.50	13.63

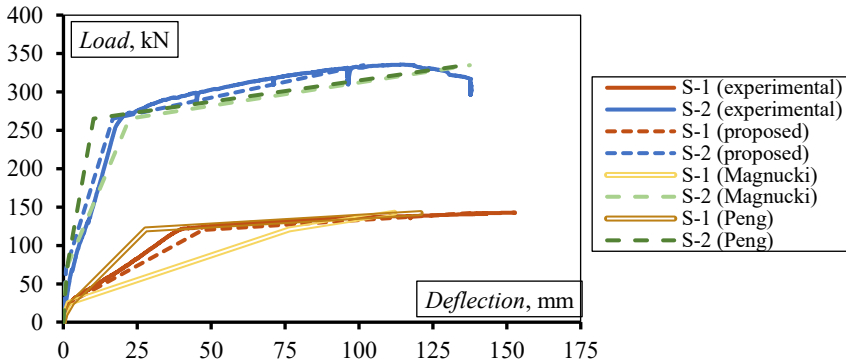


Fig. 3.32. Experimental and analytical layered slab deflection curves

Models by Magnucki et al. (2020) and Peng et al. (2024) were also used for the deflection analysis. For slab S-1, both models showed lower accuracy: the Magnucki et al. model predicted deflections that were too large after full cracking of the bottom layer and too small at the highest load, whereas the Peng et al. model underestimated slab deflection at all stages of flexural behaviour. For slab S-2, both models performed better overall, although each still produced much higher (25–26% higher) deflection values at the highest load level. The main discrepancies between these analytical predictions and the experimental results arise from the difficulty of representing layer geometry after cracking. Both models describe the general flexural behaviour of layered elements rather than focusing specifically on layered concrete elements. Additionally, Peng et al.'s model considers that a layered element is composed of layers of identical geometries and mechanical characteristics. The averaging of layer properties causes additional inaccuracy in analytical calculations. The Magnucki et al. model does not incorporate interface stiffness, while the Peng et al. model, although it does include it, requires the use of a monolithic G_{eff} due to the absence of an analytical procedure for interface stiffness. Despite these limitations, the influence of interface behaviour was less critical in these deflection calculations, as failure ultimately occurred in the normal section. The error statistics for all tested flexural stiffness models are presented in Table 3.16. Ultimately, it can be stated that the proposed flexural model was more accurate and more suitable for the analysis of layered concrete slabs.

The proposed flexural stiffness model was also tested against experimental results for a layered slab tested by other authors, i.e., Ibrahim et al. (2019) (Fig. 3.33). The presented deflection values were measured and calculated at the slab midspan. At all 3 flexural behaviour stages, the flexural model was able to reproduce a similar flexural behaviour to the experimental one and numerical analysis behaviour, determined in the dissertation's Section 2.3. At a load level of 25 kN, an interlayer slip occurred, which was explicitly accounted for in the proposed model. Throughout the test, the interface shear stiffness modulus varied from 13.03 GPa to 0.65 GPa. Models by Magnucki et al. (2020) and Peng et al. (2024) were employed up to a load of 25 kN, at which the interface adhesive failure occurs. As these models do not consider variable interface shear stiffness, the predicted deflections at this stage were lower than the experimental values. Furthermore, post-adhesive failure behaviour could not be evaluated using these models, as they do not provide solutions for interface behaviour at the following stage. It can be stated that the proposed model was more capable for this analysis. The error statistics for these models are provided in Table 3.17.

Table 3.17. Error statistics for analytical vs experimental flexural slab behaviour

Error statistics	Model			
	Proposed (up to adhesive failure)	Magnucki et al.	Peng et al.	Proposed (entire curve)
R ²	0.94	0.94	0.94	0.97
RMSE, mm	0.91	0.54	0.91	0.86

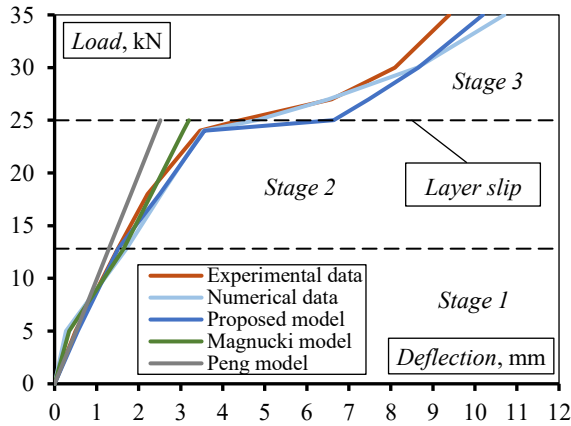


Fig. 3.33. Load–deflection experimental, numerical and analytical curves of Ibrahim et al. specimen

In the future, improvements of the proposed analytical layered concrete element flexural stiffness approach are foreseen, including the evaluation of the influence of cyclic loading, layers composed of other types of concrete, and interface connectors made of alternative materials.

3.5. Conclusions of the Third Chapter

The experimental and analytical research of layered concrete elements can be concluded by the following points:

1. The experimental push-off specimen results showed that the connector arrangement consisting of one perpendicular connector and one connector inclined in the direction of the shear force provided the highest interface shear resistance and stiffness, confirming that greater connector inclination toward the direction of shear enhances these properties.

2. The connector arrangement with two connectors inclined toward each other resulted in the smallest interface crack width, likely due to the restraint it provides against interface bending. Interfaces formed with shear keys achieved shear resistance values 3.1–3.5 times higher than those of smooth interfaces.
3. The experimental results of layered beams showed that beams with the interface connector arrangement consisting of one perpendicular connector and one connector inclined in the direction of the shear force exhibited the highest interface shear resistance (as in the push-off specimens) and, consequently, the highest flexural capacity. This confirms the same connector inclination principle observed in the push-off tests.
4. Layered beam tests determined that the connector arrangement also influenced the cracking pattern. Beams with stronger interfaces (resulting from their connector configuration) developed more pronounced flexural cracking prior to interface failure, whereas beams with weaker interfaces exhibited the opposite pattern.
5. Beams with a thicker bottom layer demonstrated higher interface resistance and greater flexural capacity. This resulted from the increased flexural stiffness of such beams, as the bottom layer had higher concrete strength and occupied a larger portion of the cross-section.
6. Layered concrete slabs with void formers failed in the normal section; however, interface cracking and interlayer slip were also observed.
7. The proposed analytical approach was validated against experimental and numerical analysis results and showed better agreement than existing models from the literature. The predicted interface shear stress–slip relationships and load–deflection curves closely matched the tests, demonstrating the approach to be effective for analysing layered concrete elements under bending. The statistical evaluation of the interface stiffness model yielded R^2 values of 0.62–0.98 and RMSE values of 0.07–0.78 MPa, while for the flexural stiffness model, R^2 ranged from 0.73–1.00 and RMSE from 0.37–6.42 mm.

General Conclusions

The research presented in this dissertation can be summarised by the following conclusions:

1. This dissertation emphasises that interface shear stiffness must be considered when analysing layered concrete elements under bending. Existing interface shear stiffness models are limited in number, do not account for multiple interface behaviour stages or differential shrinkage. Furthermore, many flexural stiffness models neglect the partial interface shear connection.
2. A novel interface shear stiffness model has been developed. The model describes the interface shear stress–slip relationship across four stages of interface behaviour, considers differential shrinkage effect and many interface properties like concrete strength, connector strength and ratio, interface roughness and more. For additional shrinkage-induced interface shear stress, a dedicated differential shrinkage model was also developed.
3. A novel flexural stiffness model, based on the built-up layers theory, was created for layered elements under bending. Its main advantages include the ability to account for interface shear stiffness. The varying interface shear stiffness values required in the model are determined using the proposed interface shear stiffness model.

4. A numerical finite element model of a layered slab with void formers was developed. The results indicated that deformation at the interface alters the distribution of normal and shear stresses in the element, reducing composite action between layers and promoting cracking. Stress concentrations were found to be higher near the void regions and lower in the concrete webs.
5. The experimental test results of push-off specimens concluded that connector inclination and interface roughness (geometry) have a significant impact on interface shear resistance and stiffness. A general rule for concrete interfaces regarding connector arrangement was established: the greater the connector inclination in the direction of the interface shear force, the higher the resulting interface shear resistance and stiffness.
6. Experimental results of layered concrete beam tests showed that, similarly to push-off specimens, interfaces with connectors most inclined in the direction of the shear force achieved the highest interface shear resistance and stiffness. This resulted in the greatest beam flexural capacity and stiffness. Beams with stronger interfaces exhibited more pronounced flexural cracking, whereas beams with weaker interfaces showed less cracking. Additionally, beams with thicker bottom layers demonstrated greater flexural capacity and stiffness.
7. It was determined, that experimental layered concrete slabs with void formers failed in a normal section. However, during the tests, interface cracking and layer slip were also observed.
8. The proposed analytical approach was verified through comparison with experimental and numerical analysis results and demonstrated closer agreement than the existing models available in the literature. The predicted interface shear stress–slip relationships and deflection values closely reflected the experimental behaviour, confirming that the approach is effective for analysing layered concrete elements subjected to bending.

References

- Abbasnia, R., Godossi, P., & Ahmadi, J. (2005). Prediction of restrained shrinkage based on restraint factors in patching repair mortar. *Cement and Concrete Research*, 35(10), 1909–1913. <https://doi.org/10.1016/j.cemconres.2004.11.020>
- Abu-Abailch, A., & Soltani, M. (2026). Nonlinear finite element analysis of interface shear transfer in various testing methods. *ACI Structural Journal*, 123(1), 61–74. <https://doi.org/10.14359/51746757>
- ACI Committee 318. (2014). *Building code requirements for structural concrete (ACI 318-14): An ACI standard; commentary on building code requirements for structural concrete (ACI 318R-14)*. American Concrete Institute.
- Anderson, A. R. (1960). Composite designs in precast and cast-in-place concrete. *Progressive Architecture*, 41(9), 172–179.
- Andrew, R. M. (2019). Global CO2 emissions from cement production, 1928-2018. *Earth System Science Data*, 11(4), 1675–1710. <https://doi.org/10.5194/essd-11-1675-2019>
- AVI. (2025). *Lattice girders GT*. <https://avi.at/en/products/lattice-girders-gt/>
- Barbosa, A. R., Trejo, D., & Nielson, D. (2017). Effect of high-strength reinforcement steel on shear friction behavior. *Journal of Bridge Engineering*, 22(8), 04017038. [https://doi.org/10.1061/\(asce\)be.1943-5592.0001015](https://doi.org/10.1061/(asce)be.1943-5592.0001015)
- Beushausen, H., & Alexander, M. G. (2007). Localised strain and stress in bonded concrete overlays subjected to differential shrinkage. *Materials and Structures*, 40(2), 189–199. <https://doi.org/10.1617/s11527-006-9130-z>

- Birkeland, P. W., & Birkeland, H. W. (1966). Connections in precast concrete construction. *ACI Journal Proceedings*, 63(3), 345–368. <https://doi.org/10.14359/7627>
- Cao, C., Hu, Z. P., Chai, Y. K., Li, Q. Y., Li, W. L., Pan, H., & Li, Y. F. (2024). Investigations on interface shear-stress transfer behavior of concrete composite slabs with lattice girders. *KSCE Journal of Civil Engineering*, 28(10), 4457–4472. <https://doi.org/10.1007/s12205-024-2165-2>
- Cavaco, E., & Camara, J. (2017). Experimental research on the behaviour of concrete-to-concrete interfaces subjected to a combination of shear and bending moment. *Engineering Structures*, 132, 278–287. <https://doi.org/10.1016/j.engstruct.2016.11.041>
- Cheng, D., Reiner, D. M., Yang, F., Cui, C., Meng, J., Shan, Y., Liu, Y., Tao, S., & Guan, D. (2023). Projecting future carbon emissions from cement production in developing countries. *Nature Communications*, 14(1), 8213. <https://doi.org/10.1038/s41467-023-43660-x>
- Comité Euro-International du Béton & Fédération Internationale de la Précontrainte. (1993). *CEB-FIP Model Code 90: Design code* (Bulletin No. 213/214). Thomas Telford.
- Crane, C. K. (2010). *Shear and shear friction of ultra-high performance concrete bridge girders* [Doctoral dissertation], Georgia Institute of Technology.
- Daneshvar, D., Behnood, A., & Robisson, A. (2022). Interfacial bond in concrete-to-concrete composites: A review. In *Construction and Building Materials*, 359, 129195. <https://doi.org/10.1016/j.conbuildmat.2022.129195>
- Davaadorj, O., Calvi, P. M., & Stanton, J. F. (2020). Shear stress transfer across concrete-to-concrete interfaces: Experimental evidence and available strength models. *PCI Journal*, 65(4), 87–111. <https://doi.org/10.15554/pcij65.4-04>
- DIANA FEA BV. (2017). Tensile Behaviour. *DIANA 10.1 user's manual*. <https://manuals.dianafea.com/d101/MatLib/node89.html>
- European Committee for Standardization. (2004). *EN 1992-1-1:2004 Eurocode 2: Design of concrete structures—Part 1-1: General rules and rules for buildings*. CEN.
- Elliott, K. S., & Jolly, C. K. (2014). *Multi-storey precast concrete framed structures* (2nd ed.). Wiley-Blackwell. <https://doi.org/10.1002/9781118587379>
- European Committee for Standardization. (2023). *Eurocode 2: Design of concrete structures – Part 1: General rules and rules for buildings* (2nd ed.). CEN.
- Bond, E. (2016). *BubbleDeck: Replacing concrete with air*. J.H. Findorff & Son Inc. <https://www.findorff.com/bubbledeck-replacing-concrete-with-air>
- Fang, Y., Mao, J., Zhang, Y., Jin, W., Tang, D., & Zhang, J. (2021). Calculation of deflection and stress of assembled concrete composite beams under shrinkage and creep and its application in member design optimization. *KSCE Journal of Civil Engineering*, 25(9), 3458–3476. <https://doi.org/10.1007/s12205-021-2092-4>
- Fang, Z., Jiang, H., Liu, A., Feng, J., & Li, Y. (2020). Shear-friction behaviour on smooth interface between high-strength and lightweight concrete. *Magazine of Concrete Research*, 72(2), 68–87. <https://doi.org/10.1680/jmacr.17.00393>

- Fasching, S. J., Huber, T., Rath, M., & Kollegger, J. (2021). Semi-precast segmental bridge construction method: Experimental investigation on the shear transfer in longitudinal and transverse direction. *Applied Sciences*, *11*(12), 5502. <https://doi.org/10.3390/app11125502>
- Fédération Internationale de la Précontrainte. (1998). *Composite floor structures: Guide to good practice*. Fédération Internationale de la Précontrainte.
- fib (2013). *fib Model Code for Concrete Structures 2010*. <https://doi.org/10.1002/9783433604090>
- Figueira, D., Sousa, C., Calçada, R., & Neves, A. S. (2016). Push-off tests in the study of cyclic behavior of interfaces between concretes cast at different times. *Journal of Structural Engineering*, *142*(1), 04015101. [https://doi.org/10.1061/\(asce\)st.1943-541x.0001364](https://doi.org/10.1061/(asce)st.1943-541x.0001364)
- FILIGRAN Trägersysteme GmbH & Co. KG. (2025). *FILIGRAN lattice girders*. <https://www.filigran.de/de/produkte/gittertraeger>.
- Foraboschi, P. (2009). Analytical solution of two-layer beam taking into account nonlinear interlayer slip. *Journal of Engineering Mechanics*, *135*(10), 1129–1146 [https://doi.org/10.1061/\(asce\)em.1943-7889.0000043](https://doi.org/10.1061/(asce)em.1943-7889.0000043)
- Gaston, J. R., & Kriz, L. B. (1964). Connections in precast concrete structures-scarf joints. *PCI Journal*, *9*(3), 37–59. <https://doi.org/10.15554/pcij.06011964.37.59>
- Gołdyn, M. (2022). Shear capacity of the interface between concretes cast at different time in the light of experimental investigations and codes of practice. *Archives of Civil Engineering*, *68*(1), 275–298. <https://doi.org/10.24425/ace.2022.140168>
- Guo, B., Liu, X., & Tan, X. (2017). Hydraulic fracturing. *Petroleum production engineering* (2nd ed., pp. 389–501). Gulf Professional Publishing.
- Haber, Z. B., Graybeal, B. A., & Nakashoji, B. (2020). Ultimate behavior of deck-to-girder composite connection details using uhpc. *Journal of Bridge Engineering*, *25*(7), 04020058. [https://doi.org/10.1061/\(asce\)be.1943-5592.0001574](https://doi.org/10.1061/(asce)be.1943-5592.0001574)
- Hanson, N. W. (1960). Precast-prestressed concrete bridges. 2. Horizontal shear connections. *Journal of the PCA Research and Development Laboratories*, *2*(2), 38–58.
- Hillebrand, M., & Hegger, J. (2023). Shear and interface shear of semi-precast slabs with lattice girders under monotonic loading. *Structural Concrete*, *24*(2), 3055–3076. <https://doi.org/10.1002/suco.202200423>
- Hillebrand, M., Schmidt, M., Wieneke, K., Classen, M., & Hegger, J. (2021). Investigations on interface shear fatigue of semi-precast slabs with lattice girders. *Applied Sciences*, *11*(23), 11196. <https://doi.org/10.3390/app112311196>
- Hossain, K. M. A., Hasib, S., & Manzur, T. (2020). Shear behavior of novel hybrid composite beams made of self-consolidating concrete and engineered cementitious composites. *Engineering Structures*, *202*, 109856. <https://doi.org/10.1016/j.engstruct.2019.109856>
- InBet Sp. z o.o. (n.d.). *Filigree slabs*. <https://www.inbet.com.pl/en/filigree-slabs>

- Ingeli, R., Čekon, M., & Paulovičová, L. (2025). Enhancement of the thermal performance of voided concrete slabs filled with expanded polystyrene. *Case Studies in Construction Materials*, 22, e04567. <https://doi.org/10.1016/j.cscm.2025.e04567>
- International Federation for Structural Concrete. (2023). *fib Model Code for Concrete Structures (2020)*.
- Ji, H., & Liu, C. (2020). Ultimate shear resistance of ultra-high performance fiber reinforced concrete-normal strength concrete beam. *Engineering Structures*, 203, 109825. <https://doi.org/10.1016/j.engstruct.2019.109825>
- Júlio, E. N. B. S., Dias-da-Costa, D., Branco, F. A. B., & Alfaiate, J. M. V. (2010). Accuracy of design code expressions for estimating longitudinal shear strength of strengthening concrete overlays. *Engineering Structures*, 32(8), 2387–2393. <https://doi.org/10.1016/j.engstruct.2010.04.013>
- Jung, D. S., Park, S. H., Han, J. W., & Kim, C. Y. (2024). Evaluation of horizontal shear performance of composite girders using separable shear connectors. *Applied Sciences*, 14(23), 10982. <https://doi.org/10.3390/app142310982>
- Khouzani, M. A., Zeynalian, M., Hashemi, M., Mostofinejad, D., Farahbod, F., & Shahadifar, M. (2021). A numerical study on flexural behavior of biaxial voided slabs containing steel cages. *Journal of Building Engineering*, 44, 103382. <https://doi.org/10.1016/j.jobe.2021.103382>
- Lam, S. S. E., Wong, V., & Lee, R. S. M. (2019). Bonding assessment of semi-precast slabs subjected to flexural load and differential shrinkage. *Engineering Structures*, 187, 25–33. <https://doi.org/10.1016/j.engstruct.2019.02.029>
- Lampropoulos, A., Tsioulou, O., & Dritsos, S. (2014). Shrinkage effect on beams strengthened with additional concrete layers. In *LABSE Symposium Report* (Vol. 102, No. 20, pp. 1520–1527). <https://doi.org/10.2749/222137814814067996>
- Li, C., Yang, Y., Su, J., Meng, H., Pan, L., & Zhao, S. (2021). Experimental research on interfacial bonding strength between vertical cast-in-situ joint and precast concrete walls. *Crystals*, 11(5), 494. <https://doi.org/10.3390/cryst11050494>
- Lin, I., & Chen, Y. (1989). Shear transfer across a crack in reinforced high-strength concrete. In *Proceedings of the Second East Asia-Pacific Conference on Structural Engineering and Construction* (pp. 505–510). Chiang Mai, Thailand.
- Ling, J. H., Lau, J. W., & Lim, Y. T. (2024). Behaviour of reinforced concrete slabs with embedded polystyrene spheres. *Civil and Sustainable Urban Engineering*, 4(1), 1–19. <https://doi.org/10.53623/csue.v4i1.391>
- Liu, J., Bu, Y., Chen, J., & Wang, Q. (2021). Contribution of shear reinforcements and concrete to the shear capacity of interfaces between concretes cast at different times. *KSCE Journal of Civil Engineering*, 25(6), 2065–2077. <https://doi.org/10.1007/s12205-021-0791-5>
- Liu, J., Fang, J.-X., Chen, J.-J., & Xu, G. (2019). Evaluation of design provisions for interface shear transfer between concretes cast at different times. *Journal of Bridge Engineering*, 24(6), 06019002. [https://doi.org/10.1061/\(asce\)be.1943-5592.0001393](https://doi.org/10.1061/(asce)be.1943-5592.0001393)

- Loov, R. E. (1978, September 25-27). *Design of precast connections* [Paper presentation]. Seminar organized by Compa International Pte, Ltd., Singapore.
- Ibrahim, A. M., Ismael, M. A., & Hussein, H. A. A. (2019). Effect of construction type on structural behaviour of r.c bubbled one-way slab. *Diyala Journal of Engineering Sciences*, 12(1), 73–79. <https://doi.org/10.24237/djes.2019.12109>
- Magnucki, K., Lewinski, J., & Magnucka-Blandzi, E. (2020). Bending of two-layer beams under uniformly distributed load – Analytical and numerical FEM studies. *Composite Structures*, 235, 111777. <https://doi.org/10.1016/j.compstruct.2019.111777>
- Soltani, M. (2016). *Interface shear transfer in reinforced concrete members: Code evaluation, modeling, and testing* (Doctoral dissertation, Clemson University). Clemson Open. https://open.clemson.edu/all_dissertations/1819/
- Manawadu, A., Qiao, P., & Wen, H. (2023). Characterization of substrate-to-overlay interface bond in concrete repairs: A review. In *Construction and Building Materials* 373, 130828. <https://doi.org/10.1016/j.conbuildmat.2023.130828>
- Manojlovic, D., & Kocetov-Misulic, T. (2016). Analysis and modelling composite timber-concrete systems: Design of bridge structure according to EN. *Gradjevinski Materijali i Konstrukcije*, 59(4), 47–74. <https://doi.org/10.5937/grmk1604047m>
- Mansour, F. R., Bakar, S. A., Vafaei, M., & Alih, S. C. (2017). Effect of substrate surface roughness on the flexural performance of concrete slabs strengthened with a steel-fiber-reinforced concrete layer. *PCI Journal*, 62(1), 78–89. <https://doi.org/10.15554/pcij62.1-02>
- Marčiukaitis, G., Jonaitis, B., & Valivonis, J. (2006). Analysis of deflections of composite slabs with profiled sheeting up to the ultimate moment. *Journal of Constructional Steel Research*, 62(8), 820–830. <https://doi.org/10.1016/j.jcsr.2005.11.022>
- Mattock, A. H. (1988). Reader comments on “Influence of concrete strength and load history on the shear friction capacity of concrete members” [Comment on the article “Influence of concrete strength and load history on the shear friction capacity of concrete members”]. *PCI Journal*, 33(1), 165–166.
- Mattock, A. H., & Kaar, P. H. (1961). Precast-prestressed concrete bridges. 4. Shear tests of continuous girders. *Journal of the PCA Research and Development Laboratories*, 3(1), 19–46.
- Mohamad, M. E., & Ibrahim, I. S. (2015). Interface shear strength of concrete-to concrete bond with and without projecting steel reinforcement. *Jurnal Teknologi*, 75(1), 169–182. <https://doi.org/10.11113/jt.v75.3707>
- Mohamed, M. S., Thamboo, J. A., & Jeyakaran, T. (2020). Experimental and numerical assessment of the flexural behaviour of semi-precast-reinforced concrete slabs. *Advances in Structural Engineering*, 23(9), 1865–1879. <https://doi.org/10.1177/1369433220904011>
- Mokhtari, S., & Hassan, M. (2024). Performance of bond between old and new concrete layers: The effective factors, durability and measurement tests—A review. *Infrastructures* 9(10), 171. <https://doi.org/10.3390/infrastructures9100171>

- Molkens, T., & Van Gysel, A. (2021). Structural behavior of floor systems made by floor plates—mechanical model based on test results. *Applied Sciences*, *11*(2), 730. <https://doi.org/10.3390/app11020730>
- Mones, R. M., & Breña, S. F. (2013). Hollow-core slabs with cast-in-place concrete toppings: A study of interfacial shear strength. *PCI Journal*, *58*(3), 124–141. <https://doi.org/10.15554/pcij.06012013.124.141>
- Newell, S., & Goggins, J. (2019). Experimental study of hybrid precast concrete lattice girder floor at construction stage. *Structures*, *20*, 866–885. <https://doi.org/10.1016/j.istruc.2019.06.022>
- Paik, I., Na, S., & Yoon, S. (2019). Assessment of CO₂ emissions by replacing an ordinary reinforced concrete slab with the void slab system in a high-rise commercial residential complex building in South Korea. *Sustainability*, *11*(1), 82. <https://doi.org/10.3390/su11010082>
- Peng, S., Zhu, Z., & Wei, Y. (2024). An analytic solution for bending of multilayered structures with interlayer-slip. *International Journal of Mechanical Sciences*, *282*, 109642. <https://doi.org/10.1016/j.ijmecsci.2024.109642>
- Rahman, M. K., Baluch, M. H., & Al-Gadhib, A. H. (1999). Modeling of shrinkage and creep stresses in concrete repair. *ACI Materials Journal*, *96*(5), 542–550. <https://doi.org/10.14359/656>
- Randl, N. (1997). *Investigations on transfer of forces between old and new concrete at different joint roughness* [Doctoral dissertation], University of Innsbruck.
- Rizkalla, S. H., Serrette, R. L., Heuvel, J. S., & Attiogbe, E. K. (1989). Multiple shear key connections for precast shear wall panels. *PCI Journal*, *34*(2), 104–120. <https://doi.org/10.15554/pcij.03011989.104.120>
- Saemann, J. C., & Washa, G. W. (1964). Horizontal shear connections between precast beams and cast-in-place slabs. *ACI Journal Proceedings*, *61*(11), 1383–1410
- Sagadevan, R., & Rao, B. N. (2019). Effect of void former shapes on one-way flexural behaviour of biaxial hollow slabs. *International Journal of Advanced Structural Engineering*, *11*(3), 297–307. <https://doi.org/10.1007/s40091-019-0231-7>
- Sasaki, K. K., Paret, T., Araiza, J. C., & Hals, P. (2010). Failure of concrete T-beam and box-girder highway bridges subjected to cyclic loading from traffic. *Engineering Structures*, *32*(7), 1838–1845. <https://doi.org/10.1016/j.engstruct.2010.01.006>
- Scott, J. (2010). *Interface shear strength in lightweight concrete bridge girders* [Master's thesis], Virginia Polytechnic Institute and State University.
- Semendary, A. A., Hamid, W. K., Steinberg, E. P., & Khoury, I. (2020). Shear friction performance between high strength concrete (HSC) and ultra high performance concrete (UHPC) for bridge connection applications. *Engineering Structures*, *205*, 110122. <https://doi.org/10.1016/j.engstruct.2019.110122>
- Shah, I. H., Miller, S. A., Jiang, D., & Myers, R. J. (2022). Cement substitution with secondary materials can reduce annual global CO₂ emissions by up to 1.3 gigatons. *Nature Communications*, *13*(1), 5758. <https://doi.org/10.1038/s41467-022-33289-7>

- Shaw, D. M., & Sneed, L. H. (2014). Interface shear transfer of lightweight-aggregate concretes cast at different times. *PCI Journal*, 59(3), 130–144. <https://doi.org/10.15554/pcij.06012014.130.144>
- Silfwerbrand, J. (1997). Stresses and strains in composite concrete beams subjected to differential shrinkage. *ACI Structural Journal*, 94(4), 347–353. <https://doi.org/10.14359/485>
- Silfwerbrand, J. (2009). Bonded concrete overlays for repairing concrete structures. In N. Delatte (Ed.), *Failure, distress and repair of concrete structures* (pp. 208–243). Woodhead Publishing. <https://doi.org/10.1533/9781845697037.2.208>
- Sneed, L. H., Krc, K., Wermager, S., & Meinheit, D. (2016). Interface shear transfer of lightweight-aggregate concretes with different lightweight aggregates. *PCI Journal*, 61(2), 38–55. <https://doi.org/10.15554/pcij.03012016.38.55>
- Sørensen, J. H., Hoang, L. C., Olesen, J. F., & Fischer, G. (2017). Test and analysis of a new ductile shear connection design for RC shear walls. *Structural Concrete*, 18(1), 189–204. <https://doi.org/10.1002/suco.201600056>
- de Sousa, H., & de Sousa, R. M. (2019, June 16–19). *Evaluation of construction provisions to avoid cracking in masonry partitions affected by structural deformations of concrete slabs* [Paper presentation]. 13th North American Masonry Conference, Salt Lake City, UT, United States.
- Stehle, J., Kanellopoulos, A., & Karihaloo, B. L. (2011). Performance of joints in reinforced concrete slabs for two-way spanning action. *Proceedings of the Institution of Civil Engineers: Structures and Buildings*, 164(3), 197–209. <https://doi.org/10.1680/stbu.9.00038>
- TNO DIANA BV. (2015). *User's Manual - Material Library*. <https://manuals.dianafea.com/d100/MatLib/node328.html>
- Tsioulou, O. T., Lampropoulos, A. P., & Dritsos, S. E. (2013). Experimental investigation of interface behaviour of RC beams strengthened with concrete layers. *Construction and Building Materials*, 40, 50–59. <https://doi.org/10.1016/j.conbuildmat.2012.09.093>
- Universal Slab. (2024). *Rib and block slab system*. <https://www.universalslab.co.za/product/rib-and-block-slab-system/>
- Valivonis, J., Popov, V., Jonaitis, B., & Daugevičius, M. (2015). The analysis of concreting process impacts on the behaviour of residual liners of cast-in-situ voided slabs. *Archives of Civil and Mechanical Engineering*, 15(4), 997–1006. <https://doi.org/10.1016/j.acme.2015.06.007>
- Vecchio, F. J., & Collins, M. P. (1986). Modified compression-field theory for reinforced concrete elements subjected to shear. *Journal of the American Concrete Institute*, 83(2), 219–231. <https://doi.org/10.14359/10416>
- Vinkler, M., & Vitek, J. L. (2019). Drying and shrinkage of massive concrete wall segments—3 years experiment and analytical observations. *Materials and Structures*, 52(2), 29. <https://doi.org/10.1617/s11527-019-1329-x>
- Volaity, S. S., Aylas-Paredes, B. K., Han, T., Huang, J., Sridhar, S., Sant, G., Kumar, A., & Neithalath, N. (2025). Towards decarbonization of cement industry: a critical review of

- electrification technologies for sustainable cement production. *Npj Materials Sustainability*, 3, 23. <https://doi.org/10.1038/s44296-025-00068-6>
- Wang, J., Xiao, Z., Zhu, C., Feng, C., & Liu, J. (2021). Experiment on the bonding performance of the lightweight aggregate and normal weight concrete composite beams. *Case Studies in Construction Materials*, 15, e00565. <https://doi.org/10.1016/j.cscm.2021.e00565>
- Widodo, S. (2017). Bond strength between hybrid fiber-reinforced lightweight aggregate concrete substrate and self-compacting concrete as topping layer. *Advances in Civil Engineering*, 2017, 7015254. <https://doi.org/10.1155/2017/7015254>
- Xu, J., Wu, C., Li, Z. X., & Ng, C. T. (2015). Numerical analysis of shear transfer across an initially uncrack reinforced concrete member. *Engineering Structures*, 102, 296–309. <https://doi.org/10.1016/j.engstruct.2015.08.022>
- Yang, K. H. (2016). Shear stress-relative slip relationship at concrete interfaces. *Advances in Materials Science and Engineering*, 2016, 6475161. <https://doi.org/10.1155/2016/6475161>
- Yuan, Q., Chen, R., Zuo, S., Huang, T., Zhang, K., & Mei, D. (2023). Bonding performance between distinct layers of cast-in-situ self-compacting concrete and ordinary concrete. *Construction and Building Materials*, 373, 130892. <https://doi.org/10.1016/j.conbuildmat.2023.130892>
- Zajac, J., Drobiec, Ł., Jasiński, R., Wieczorek, M., Mazur, W., Grzyb, K., & Kisiołek, A. (2021). The behaviour of half-slabs and hollow-core slab in four-edge supported conditions. *Applied Sciences*, 11(21), 10354. <https://doi.org/10.3390/app112110354>
- Zhang, B., Kang, J., Li, J., Liang, J., & Wang, J. (2022). Evaluation of interface rapid bond strength between normal concrete and ternary system fast setting and rapid hardening self-compacting concrete. *Construction and Building Materials*, 347, 128515. <https://doi.org/10.1016/j.conbuildmat.2022.128515>
- Zhang, W., Lin, J., Huang, Y., Lin, B., & Liu, X. (2024). Experimental and numerical studies on flexural performance of composite beams under cyclic loading. *Structures*, 70, 107728. <https://doi.org/10.1016/j.istruc.2024.107728>
- Zhang, W., Zhang, S., Wei, J., & Huang, Y. (2024). Flexural behavior of SFRC-NC composite beams: An experimental and numerical analytical study. *Structures*, 60, 105823. <https://doi.org/10.1016/j.istruc.2023.105823>
- Zhang, W., Zheng, D., Huang, Y., & Kang, S. (2024). Experimental and simulative analysis of flexural performance in UHPC-RC hybrid beams. *Construction and Building Materials*, 436, 136889. <https://doi.org/10.1016/j.conbuildmat.2024.136889>

List of Scientific Publications by the Author on the Topic of the Dissertation

Papers in the Reviewed Scientific Journals

Masėnas, J., Šalna, R., Juknevičius, L., & Valivonis, J. (2021). Deflection analysis of layered slabs with plastic inserts. *Materials*, 14(20), 6050. <https://doi.org/10.3390/ma14206050>

Masėnas, J. (2022). Cracking analysis of precast – in situ reinforced concrete slab with plastic void formers. *Mokslas – Lietuvos Ateitis / Science – Future of Lithuania*, 14. <https://doi.org/10.3846/mla.2022.15151>

Masėnas, J., Šalna, R., Juknevičius, L., & Valivonis, J. (2023). Analytical method and analysis of cold-joint interface. *Applied Sciences*, 13(7), 4176. <https://doi.org/10.3390/app13074176>

Masėnas, J., & Valivonis, J. (2025). Evaluation of connectors' influence on the interface behaviour between concrete layers. *Materials and Structures*, 58, 28. <https://doi.org/10.1617/s11527-024-02553-1>

Valivonis, J., Masėnas, J., & Kaklauskas, G. (2026). Experimental and analytical analysis of layered concrete beams with partially stiff interfaces. *Engineering Structures*, 349, 121885. <https://doi.org/10.1016/j.engstruct.2025.121885>

Papers in Other Editions

Masénas, J., & Valivonis, J. (2024). Layer interface behaviour in layered concrete structural elements. In *Modern building materials, structures and techniques: MBMST 2023 (Lecture Notes in Civil Engineering, Vol. 392, pp. 109–118)*. Springer. https://doi.org/10.1007/978-3-031-44603-0_10

Summary in Lithuanian

Įvadas

Problemos formulavimas

Konstruciniai elementai, sudaryti iš skirtingu metu betonuotų ir skirtingų medžiagų savybių betono sluoksnių, yra vadinami sluoksniuotaisiais gelžbetoniniais konstrukciniais elementais. Kai yra naudojamas papildomas didelio stiprio betono sluoksnis, palyginti su ištisinais skerspjūviais, šio tipo elementai gali suteikti tokių privalumų kaip mažesnės medžiagų sąnaudos, skerspjūvio aukštis, mažesni įlinkiai ir aukštesnė šlyties laikomoji galia. Viršutiniai betono sluoksniai taip pat gali būti naudojami stiprinti esamoms konstrukcijoms, darant renovaciją tvaresnę - mažinant griovimo darbų mastą, sutaupant medžiagų ir mažinant atliekų kiekį. Taip pat sluoksniuotieji gelžbetoniniai elementai gali būti įrengiami su plastikiniais intarpais, kurie mažina konstrukcijos svorį ir betono tūrį, taip suteikdami aplinkosauginę naudą dėl sumažinto cemento kiekio ir naudojamų perdirbto plastiko gaminių. Sluoksniuotų gelžbetoninių konstrukcijų pavyzdžiai apima liktinio klojinio gelžbetonines plokštes, tiltų sijas ir kiaurymėtąsias gelžbetonines plokštes su viršutiniu betono sluoksniu. Betonas taip pat gali būti betonuojamas etapais dėl įvairių techninių priežasčių.

Sluoksniuotų gelžbetoninių konstrukcinių elementų darbas priklauso nuo sluoksnių jungties charakteristikų. Nepakankama sąveika tarp sluoksnių mažina jungties standumą ir sluoksniuotojo elemento lenkiamąjį standumą. Dalyje publikuotų tyrimų (Cavaco & Camara, 2017; Foraboschi, 2009; Marčiukaitis et al., 2006) teigiama, kad sluoksniuotų

elementų jungtys beveik niekada nėra visiškai standžios ir turėtų būti laikomos dalinio standumo elementais dar net prieš apkrovimą.

Didžioji dalis gelžbetoninių konstrukcijų projektavimo normų ir egzistuojantys teoriniai modeliai literatūroje neatsižvelgia į dalinį sluoksnių jungties standumą. Yra siūloma vertinti visiškai standžią jungtį ir rekomenduojama tipinė ištisinio skerspjuvio konstrukcijos analizė – taip perversinant sluoksniuotos konstrukcijos lenkiamąjį standumą. Atskirų betono sluoksnių nepaisymas sukelia papildomų reikšmingų apribojimų. Ignoruojant skirtingas sluoksnių medžiagų savybes ir geometrines charakteristikas, dar labiau didėja lenkiamojo standumo vertinimo netikslumas. Nepaisant atskirų sluoksnių darbo, negalima numatyti individualaus sluoksnių pleišėjimo. Galiausiai, literatūroje pateikti analitiniai modeliai nevertina sluoksnių susitraukimo skirtumo efekto, atsirandančio dėl skirtingo betono sluoksnių betonavimo laiko. Šis reiškinys sukelia įtempius jungtyje, kurie sumažina jungties stiprumą ir standumą.

Darbo aktualumas

Šiame darbe pristatoma betono sluoksnių jungties ir lenkiamųjų sluoksniuotų gelžbetoninių elementų elgsenos analizė. Disertacijoje pateikiami nauji teoriniai modeliai jungties atsparumui ir šlyties standumui, sluoksnių susitraukimo skirtumo efektui, lenkiamųjų sluoksniuotų elementų standumui, vertinti. Drauge šie modeliai sudaro naują sluoksniuotų gelžbetoninių elementų analitinį standumo metodą, atsižvelgiantį į dalinį jungties standumą. Disertacijoje pateikta eksperimentinė ir skaitinė sluoksniuotų gelžbetoninių elementų analizė praplečia supratimą apie sluoksniuotų gelžbetoninių elementų elgseną ir jų sluoksnių jungtis bei veiksnius, turinčius įtakos jų darbui. Pasiūlyti teoriniai modeliai suteikia naujas galimybes analitiškai vertinti tokius elementus. Tinkamai vertinant jungties elgseną ir konstrukcijos darbą, gali būti pasiektas saugesnis ir efektyvesnis sluoksniuotų gelžbetoninių elementų projektavimas. Galiausiai, yra geriau išnaudojami tokie elementų privalumai kaip mažesnės medžiagų sąnaudos, didesnis statybos greitis, aplinkai draugiški inžineriniai sprendimai, konstrukcinė ir ekonominė nauda bei kt.

Tyrimo objektas

Šio tyrimo objektai – sluoksniuotųjų gelžbetoninių elementų, veikiamų trumpalaikę statinę apkrovą, elgsenos analizė, sluoksnių jungties šlyties standumo ir sluoksniuotųjų gelžbetoninių elementų lenkiamojo standumo modeliai.

Darbo tikslas

Disertacijoje siekiama sukurti analitinį modelį, skirtą įvertinti sluoksniuotų gelžbetoninių elementų lenkiamąjį standumą, atsižvelgiant į sluoksnių jungties savybes ir elgseną.

Darbo uždaviniai

Darbo tikslui pasiekti sprendžiami šie uždaviniai:

1. Atlikti esamų betono sluoksnių jungčių ir sluoksniuotų lenkiamųjų gelžbetoninių elementų tyrimų, taip pat teorinių jungčių elgsenos ir sluoksniuotų elementų lenkiamojo standumo modelių apžvalgą.

2. Sukurti analitinį betono sluoksnių jungties elgsenos modelį, vertinantį sluoksnių susitraukimo skirtumo efektą.
3. Sukurti analitinį sluoksniuoto gelžbetoninio elemento lenkiamojo standumo modelį, vertinantį sluoksnių jungties dalinį standumą.
4. Atlikti sluoksniuotos gelžbetoninės plokštės su plastiko intarpais skaitinę analizę.
5. Atlikti eksperimentinius betono sluoksnių jungčių, sluoksniuotų gelžbetoninių sijų ir sluoksniuotų gelžbetoninių plokščių tyrimus.
6. Atlikti siūlomų teorinių modelių validaciją, lyginant analitinių skaičiavimų rezultatus su eksperimentinės ir skaitinės analizės rezultatais.

Tyrimų metodika

Siekiant ištirti tyrimo objektą parinkti šie metodai:

- teoriniai metodai: sukurti teoriniai betono sluoksnių jungties ir lenkiamojo sluoksniuoto gelžbetoninio elemento elgsenos modeliai. Taip pat sukurtas skaitinis lenkiamojo sluoksniuoto gelžbetoninio elemento modelis;
- eksperimentiniai metodai: atlikti eksperimentiniai betono sluoksnių jungčių ir lenkiamųjų sluoksniuotų gelžbetoninių elementų bandymai;
- statistikos metodai: išvados padarytos renkant, analizuojant ir aiškinant statistinius duomenis.

Darbo mokslinis naujumas

Teorinių ir eksperimentinių sluoksniuotų gelžbetoninių konstrukcinių elementų tyrimų mokslinio naujumo aspektai:

1. Sukurti nauji analitiniai skaičiavimo modeliai, betono sluoksnių jungties standumui ir šlyties atsparumui, taip pat sluoksniuotų gelžbetoninių elementų su dalinai standžiomis jungtimis lenkiamajam standumui, vertinti.
2. Sukurtas naujas teorinis modelis, skirtas sluoksnių susitraukimo skirtumo deformacijai ir dėl šio efekto susidariusiam šlyties įtempiui, turinčiam įtaką jungties darbui, nustatyti.
3. Gauti nauji duomenys apie veiksnius, darančius įtaką betono sluoksnių jungčių ir lenkiamųjų sluoksniuotų gelžbetoninių elementų standumui ir stiprumui, kartu su šių elementų pleišėjimo ir irimo pobūdžio analize.
4. Gauti nauji duomenys apie sluoksniuotų gelžbetoninių elementų skaitinio modeliavimo procesus ir analizę.

Darbo rezultatų praktinė reikšmė

Teorinių ir eksperimentinių sluoksniuotų gelžbetoninių elementų tyrimų praktinės reikšmės aspektai:

1. Naujas teorinis skaičiavimo modelis, kuris gali būti naudojamas projektuojant sluoksniuotas betonines jungtis. Naudojant modelį galima parinkti efektyviausias medžiagų savybes ir užkirsti kelią būdingiems jungties yrimo būdams.
2. Naujas sluoksnių susitraukimo skirtumo modelis, kuris gali būti naudojamas įvertinti šio efekto poveikiui betono jungčių galiai ir standumui.
3. Naujas teorinis sluoksniuotų konstrukcijų modelis, kuris gali būti naudojamas projektuojant lenkiamus sluoksniuotus gelžbetoninius elementus su dalinai standžiomis jungtimis. Faktinio jungties standumo vertinimas padeda tiksliau nustatyti lenkiamąjį sluoksniuoto gelžbetoninio elemento standumą.
4. Eksperimentiniai betoninių sluoksnių jungčių ir sluoksniuotų lenkiamų elementų bandymų rezultatai suteikia žinių apie konstrukcijų yrimo, pleišėjimo būdus, taip pat medžiagų savybių ir kitų veiksnių įtaką sluoksniuotų elementų elgsenai.
5. Naudojant šiame darbe pateiktus analizės duomenis, galima efektyviau išnaudoti sluoksniuotų elementų privalumus, įskaitant mažesnes medžiagų sąnaudas, mažesnę statybos darbų trukmę, aplinkai draugiškus inžinerinius sprendimus, konstrukcinę, ekonominę naudą ir kt.

Ginamieji teiginiai

1. Siūlomu betono sluoksnių jungties elgsenos analizės metodu tiksliai numatoma jungties šlyties įtempio ir sluoksniuoto pasislinkimo priklausomybė keturiomis jungties darbo stadijomis. Iš žinomų šlyties įtempio ir atitinkamo sluoksniuoto pasislinkimo reikšmių galima nustatyti tikslią jungties šlyties standumo modulio vertę.
2. Siūlomas sluoksnių susitraukimo skirtumo efekto modelis tiksliai vertina sluoksnių susitraukimo skirtumo deformacijas ir šio efekto sukeltus jungties šlyties įtempius.
3. Siūlomas analitinis metodas, atsižvelgiantis į dalinį jungties standumą, tiksliai vertina sluoksniuoto lenkiamo gelžbetoninio elemento įlinkį prie skirtingų jungties standumo reikšmių ir konstrukcijos apkrovimo stadijų.

Darbo rezultatų aprobavimas

Disertacijoje atlikti tyrimai publikuoti 5 moksliniuose straipsniuose: 4 – žurnaluose, indeksuojamuose *WoS*.

- Tyrimų rezultatai paskelbti 3 mokslinėse konferencijose, iš kurių 2 buvo tarptautinės:
- 25^o Jaunųjų mokslininkų konferencijoje „Mokslas – Lietuvos ateitis“, 2021 m., Vilniuje, Lietuvoje.
 - MBMST 2023: „14th International Conference Modern Building Materials, Structures and Techniques“, 2023 m., Vilniuje, Lietuvoje.
 - ICCEFA 2024: „5th International Conference on Civil Engineering Fundamentals and Applications“, 2024 m., Lisabonoje, Portugalijoje.

Disertacijos struktūra

Disertaciją sudaro įvadas, trys skyriai, bendrosios išvados, literatūros sąrašas, autoriaus publikacijų disertacijos tema, sąrašas. Disertacijos apimtis (be priedų) – 136 puslapiai. Darbe pateiktos 139 lygtys, 91 paveikslas, 22 lentelės ir 102 literatūros šaltiniai.

Padėka

Darbo autorius nuoširdžiai dėkoja savo vadovui, Gelžbetoninių konstrukcijų ir geotechnikos katedros vedėjui, prof. dr. Juozui Valivoniui už pagalbą, vertingus patarimus, dalijimąsi žiniomis ir skatinimą viso šio tyrimo metu.

Autorius dėkoja ir tiems, kurie padėjo eksperimentinių tyrimų etape: Statybinių konstrukcijų ir geotechnikos laboratorijos vedėjui Gintarui Jurkėnui, taip pat dr. Aleksandr Sokolov, Lolitai Kairytei, Juozui Gervei, Aleksandr Zajac, Grigorij Kuksov ir Lukui Ravnaličevui už neįkainojamą techninę pagalbą. Taip pat kolegoms doktorantams už jų bendradarbiavimą, Statybos fakulteto dekanui doc. dr. Remigijui Šalnai už palaikymą.

Padėka kolegoms iš Lisabonos NOVA universiteto, kur buvo atlikta mokslinė stažuotė ir disertacijos pristatymas. Ypatingas ačiū dr. Eduardo Cavaco ir kolegoms doktorantams Barbara Gomes ir Peiman Ghaderi už dosnų pasidalinimą žiniomis apie sluoksniuotų betoninių elementų mechaniką, skaitmeninį modeliavimą ir gelžbetoninių konstrukcijų elgseną.

Dalis disertacijos tyrimų buvo atlikti įgyvendinant projektą „Misijomis grįstų mokslo ir inovacijų programų įgyvendinimas“ Nr. 02-002-P-0001, finansuojamą Ekonomikos gaivinimo ir atsparumo didinimo plano „Naujos kartos Lietuva“ lėšomis.

Galiausiai autorius dėkoja savo šeimai – tėvams už paskatinimą rinktis doktorantūros studijas, žmonai Viktorijai ir vaikams už ramybę, nuolatinį palaikymą, suteiktą galimybę tęsti mokslus ir asmeniškai tobulėti.

1. Sluoksniuotųjų gelžbetoninių elementų su dalinai standžiomis sluoksnių jungtimis lenkiamojo standumo analizė

Pirmajame disertacijos skyriuje atlikta literatūros šaltinių disertacijos tema apžvalga. Skyriaus pabaigoje apibrėžtas disertacijos tikslas bei iškelti darbo uždaviniai, aptarta sluoksnių jungties elgsenos specifika. Nurodyti veiksniai, lemiantys jungties atsparumą šlyčiai ir šlyties standumą. Taip pat analizuoti jau publikuoti jungties elgsenos analitiniai modeliai. Nustatyta, kad didžioji dalis jungties modelių vertina tik jungties atsparumą šlyčiai, tačiau šioje disertacijoje tiriamas jungties šlyties standumas. Išanalizavus literatūroje pateiktus jungties šlyties standumo modelius, padaryta išvada, kad esamų modelių kiekis yra nepakankamas, modeliai retai vertina kelias jungties darbo stadijas, kintančią skirtingų šlyties mechanizmų įtaką. Nustatyta, kad modeliai nevertina sluoksnių susitraukimo skirtumo efekto. Iškeltas tikslas sukurti naują betono sluoksnių jungties šlyties standumo modelį, vertinantį prieš tai minėtus aspektus.

Šiame skyriuje pristatyti realiomis inžinerinėmis sąlygomis aptinkami, sluoksniuotų lenkiamų gelžbetoninių elementų pavyzdžiai ir jų elgsenos specifika. Taip pat atlikta sluoksniuotųjų gelžbetoninių elementų eksperimentinių tyrimų analizė, pateikta literatūroje.

Padaryta išvada, kad norint tinkamai vertinti sluoksniuotų gelžbetoninių elementų lenkiamąjį darbą, privaloma vertinti sluoksnių jungties standumą ir kitas savybes. Galiausiai, išanalizuoti analitiniai sluoksniuotų gelžbetoninių konstrukcijų lenkiamojo standumo modeliai. Nustatyta, kad didžioji dalis modelių nevertina sluoksnių jungties standumo arba nepateikia analitinės metodikos šiam dydžiui nustatyti. Taip pat modeliai neteisingai vertina atskirų sluoksnių charakteristikas. Iškeltas tikslas sukurti naują sluoksniuotų gelžbetoninių konstrukcijų lenkiamojo standumo modelį, vertinantį jungties standumą ir atskirų sluoksnių geometrines bei medžiagų savybes.

2. Betoninių sluoksnių jungčių ir lenkiamų sluoksniuotų gelžbetoninių elementų standumo vertinimo modeliai

Antrajame skyriuje pristatytas analitinis metodas, kuriuo nustatomas lenkiamojo sluoksniuotojo gelžbetoninio elemento įlinkis, vertinant dalinį jungties standumą. Metodas susideda iš dviejų etapų.

Pirmajame etape naudojamas autoriaus sukurtas jungties elgsenos modelis, kuriuo nustatoma jungties šlyties įtempių ir sluoksnių pasislinkimo priklausomybė prie skirtingų jungties elgsenos stadijų. Taip pat, naudojantis autoriaus pasiūlytų sluoksnių susitraukimo skirtumo modeliu, nustatomi šio efekto sukelti papildomi jungties šlyties įtempiai. Žinant jungties šlyties įtempių ir sluoksnių pasislinkimo vertes, nustatomas jungties šlyties standumo modulis prie skirtingų jungties elgsenos stadijų. Antrame etape pristatomas analitinis metodas, kuriuo nustatomas sluoksniuotos konstrukcijos įlinkis prie skirtingų apkrovimo etapų. Taip pat svarbu paminėti, kad šiame modelyje naudojama kintanti, pagal anksčiau aprašytą metodiką nustatyta, jungties šlyties standumo vertė. Šioje santraukoje pateikiami bendrieji pasiūlytų analitinių metodų principai.

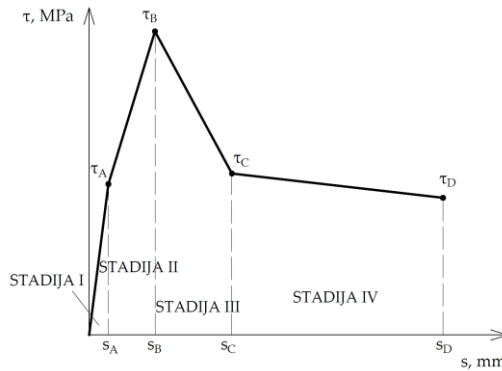
Analitinis jungties šlyties standumo modelis sukurtas atlikus literatūroje pateiktų eksperimentinių jungties šlyties tyrimų analizę (Barbosa et al., 2017; Crane, 2010; Fang et al., 2020; Figueira et al., 2016; Júlio et al., 2010; Liu et al., 2019, 2021; Mohamad & Ibrahim, 2015; Scott, 2010; Semendary et al., 2020; Shaw & Sneed, 2014; Sneed et al., 2016) ir pritaikius projektavimo normų rekomendacijas (European Committee for Standardization, 2023; International Federation for Structural Concrete (fib), 2020). Jungties šlyties įtempių- sluoksnių pasislinkimo priklausomybės kreivė susideda iš 4 jungties darbo stadijų (S2.1 pav.).

Kiekvienai stadijai būdingas skirtingų šlyties mechanizmų dominavimas, taip pat skirtinga jungties medžiagų geometrinių savybių įtaka. Pirmoje stadijoje adhezija tarp sluoksnių priešinasi jungties šlyčiai. Taške τ_A prasideda jungties pleišėjimas. Šlyties įtempių ir sluoksnių pasislinkimo lygtys pirmoje stadijoje (S2.1 ir S2.2 lygtys):

$$\tau_A = 0.2\eta f_{ct}, \quad (S2.1)$$

$$s_A = 0.01 \div 0.05 \text{ mm}, \quad (S2.2)$$

čia η – koeficientas, vertinantis jungties atstumą nuo kompozitinio skerspjūvio svorio centro, f_{ct} – tempiamasis betono stipris.



S2.1 pav. Jungties analitinio modelio šlyties įtempių-sluoksnių pasislinkimo priklausomybės kreivė

Antroje stadijoje jungtis yra pradėjusi pleišėti. Taške τ_B galutinai prarandama adhezija ir mikro trintis tarp sluoksnių – jungties plyšys išsivysto per visą jungties plokštumą. Šlyties įtempių ir sluoksnių pasislinkimo lygtys antroje stadijoje (S2.3 ir S2.4 lygtys):

$$\tau_B = \eta \kappa (\tau_{fr} + 0.5\tau_{dw}) - \sigma_{sh}, \quad (S2.3)$$

$$s_B = 106 f_c^{-2.08} + 18 \left(\frac{f_y \rho}{f_c} \right)^{2.08}, \quad (S2.4)$$

čia κ – koeficientas, vertinantis jungties betono stiprio ir jungties inkarų įtempių santykį, τ_{fr} – jungties trinties šlyties įtempiai, τ_{dw} – jungties kaiščio efekto įtempiai, σ_{sh} – sluoksnių susitraukimo skirtumo sukelti šlyties įtempiai, f_c – betono gniuždomasis stipris, f_y – inkarų takumo įtempiai, ρ – jungties inkarų santykis.

Trečioji stadija yra pereinamoji stadija prie jungties inkarų darbu paremtų šlyties mechanizmų. Šlyties įtempių ir sluoksnių pasislinkimo lygtys trečioje stadijoje (S2.5 ir S2.6 lygtys):

$$\tau_C = \eta (\tau_{fr} + 0.5\tau_{dw}), \quad (S2.5)$$

$$s_C = 2.3 f_c^{-0.28} - 0.00003 A_s^{1.4}, \quad (S2.6)$$

čia A_s – bendras jungties inkarų skerspjūvio plotas.

Ketvirtoje stadijoje trintis ir kaiščio efektas priešinasi jungties šlyčiai. Šlyties įtempių ir sluoksnių pasislinkimo lygtys ketvirtoje stadijoje (S2.7 ir S2.8 lygtys):

$$\tau_D = \eta D (\tau_{fr} + 0.5\tau_{dw}), \quad (S2.7)$$

Sluoksnių susitraukimo skirtumo sukelti šlyties įtempiai apskaičiuojami pagal lygtį S2.9:

$$\sigma_{sh} = \frac{F_v}{lb}, \quad (\text{S2.9})$$

čia F_v – sluoksnių susitraukimo skirtumo sukelta šlyties jėga jungtyje, l – jungties ilgis, b – jungties plotis.

Sluoksnių susitraukimo skirtumo deformacija yra nustatoma pagal lygtį S2.10:

$$\varepsilon_s = \varepsilon_{2,y} - \varepsilon_{1,t}, \quad (\text{S2.10})$$

čia $\varepsilon_{2,y}$ – susitraukimo deformacija antrojo sluoksnio svorio centre, $\varepsilon_{1,t}$ – susitraukimo deformacija pirmojo sluoksnio viršuje.

Galiausiai, atlikus jungties elgsenos analizę (žinant jungties šlyties įtempių ir sluoksnių pasislinkimo vertes ir įvertinus sumažėjusį šlyties atsparumą dėl traukumo), skirtingomis jungties elgsenos stadijomis, nustatomas kintantis jungties šlyties standumo modulis pagal lygtį S2.11:

$$G_{eff}(s) = \frac{\tau}{s}, \quad (\text{S2.11})$$

čia τ – jungties šlyties įtempiai atitinkamoje elgsenos stadijoje, s – sluoksnių pasislinkimas toje pačioje elgsenos stadijoje.

Antroje sluoksniuotos konstrukcijos analizės stadijoje, naudojantis sudėtinių sluoksnių teorija pagrįstu standumo modeliu, nustatomos elemento įlinkių reikšmės prie skirtingų jungties standumo verčių ir konstrukcijos apkrovimo stadijų. Pagal lygtį S2.12 nustatomas įlinkis:

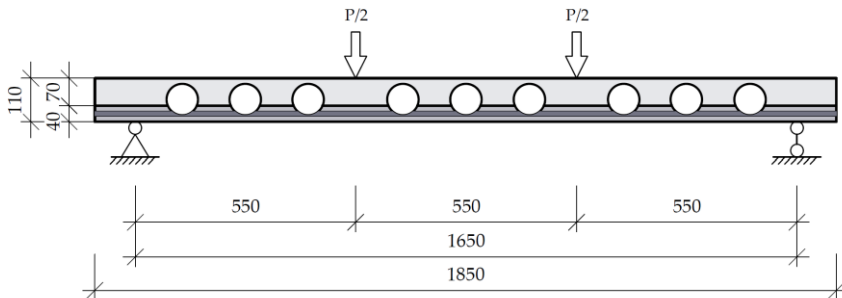
$$w = M \left(\left(\frac{l^2}{8E_{eff}I_{eff}} \right) + \frac{1}{D} \left(\frac{\cosh(0,5\lambda l) - 1}{\lambda^2 \cosh(0,5\lambda l)} \right) \right), \quad (\text{S2.12})$$

$$\lambda = \sqrt{\alpha\gamma}, \quad (\text{S2.13})$$

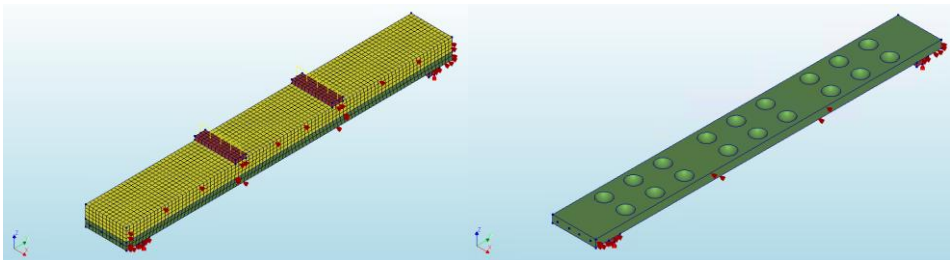
$$\alpha = \frac{bG_{eff}}{z_{eff}}, \quad (\text{S2.14})$$

čia M – lenkiamasis momentas, l – tarpatramis, $E_{eff}I_{eff}$, $\frac{1}{D}$ ir γ – kompozitinę konstrukcijos standumą apibūdinantys dydžiai, λ ir α – jungties šlyties standumą apibūdinantys dydžiai, b – jungties plotis, z_{eff} – atstumas tarp sluoksnių svorio centrų.

Šiame skyriuje taip pat atlikta skaitinė sluoksniuotos plokštės su plastiko tarpais analizė. Plokštės skaičiuotinė schema parodyta S2.4 pav. Plokštės skaitinis modelis pavaizduotas S2.5 pav. Modelis išdalintas 20 mm trimačiais baigtiniais elementais. Betono gniuždomosios savybėms naudotas Thorefeldt modelis (TNO DIANA BV, 2015), o tempimui apibudinti – trapaus irimo kreivė (DIANA FEA BV, 2017). Armatūros fiziniams savybėms aprašyti taikomas Von Mises plastiškumas. Sluoksnių jungčiai naudotas tamprios elgsenos modelis. Netiesinė analizė atlikta arkos ilgio metodu. Plokštė apkrauta keilomis apkrovimo stadijomis (A-F).

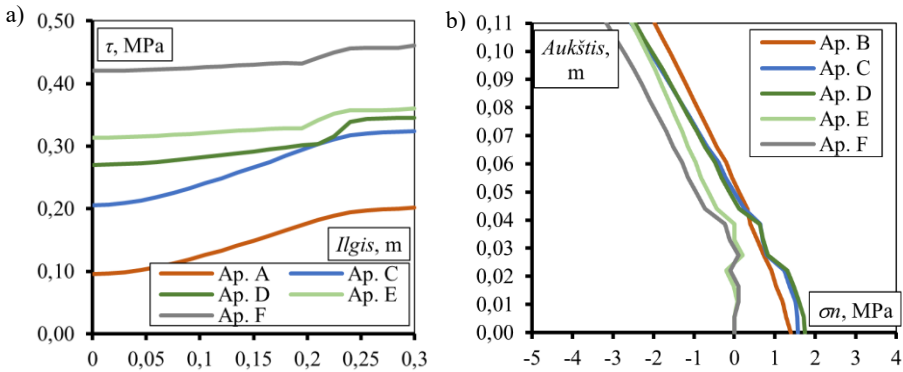


S2.4 pav. Sluoksniuotos plokštės skaičiuotinė schema

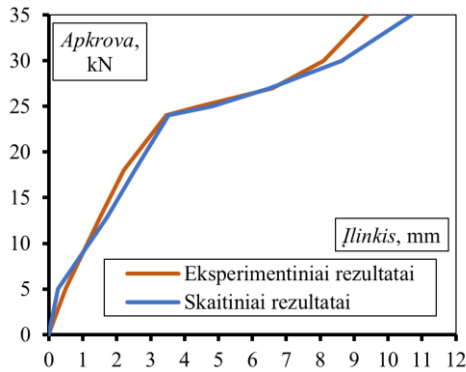


S2.5 pav. Sluoksniuotos plokštės skaitinis modelis

Analizės rezultatai parodė, kad jungties deformacija lemia normalinių įtempių persiskirstymą konstrukcijos skerspjūvyje ir šlyties įtempių persiskirstymą sluoksnių jungtyje, konstrukcijos sluoksniai pradeda veikti individualiau ir tai lemia suintensyvėjusį sluoksnių pleišėjimą normaliniame pjūvyje. Jungties šlyties įtempių pasiskirstymas pavaizduotas S2.6a pav., o normalinių įtempių pasiskirstymas viename iš analizuotų pjūvių pavaizduotas S2.6b pav. Taip pat didesnė normalinių įtempių koncentracija pastebėta zonose, esančiose šalia tuštumų, kurias suformuoja plastikiniai tarpai. Mažesnės įtempių reikšmės nustatytos betoninėse sienelėse tarp tuštumų. S2.7 pav. matomos eksperimentinės ir skaitinės analizės metu nustatytos plokštės įlinkių kreivės.



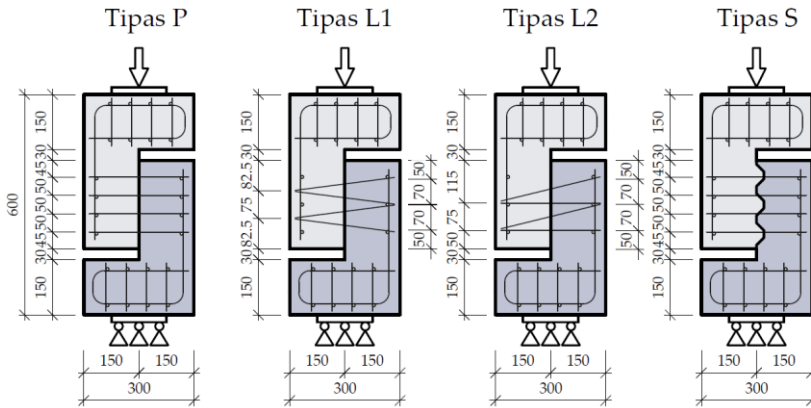
S2.6 pav. Įtempių pasiskirstymas: a) šlyties įtempiai jungtyje, b) normaliniai įtempiai skerspjūvyje



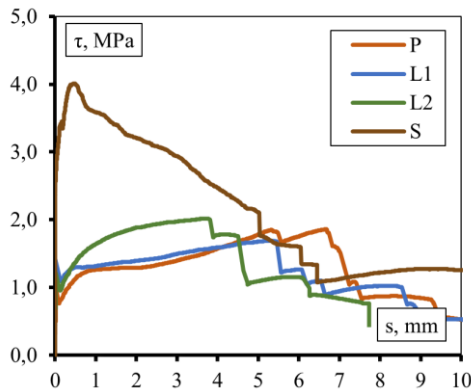
S2.7 pav. Eksperimentinė ir skaitinė įlinkių kreivės

3. Eksperimentiniai sluoksniuotų gelžbetoninių elementų su dalinai standžiomis sluoksnių jungtimis tyrimai

Trečiajame skyriuje aprašyti eksperimentiniai sluoksniuotų elementų bandymai ir atlikta analitinių modelių validacija. Išbandyta 17 eksperimentinių sluoksnių jungties bandinių. Bandiniai skyrėsi jungties geometrija (lygi ir sprauselių jungtis) ir jungties inkarų išdėstymu (statmeni inkarai, pasvirę). Bandinių geometrija pavaizduota S3.1 pav. Nustatyta, kad lygi jungtis turi 3,1–3,5 kartų mažesnę atsparumą šlyčiai už sprauselių jungtį. Taip pat nustatyta, kad kuo labiau jungties inkarai pasvirę šlyties jėgos kryptimi, tuo pasiekiamas didesnis jungties šlyties atsparumas ir standumas (L2 konfigūracija pademonstravo didžiausią atsparumą ir standumą). Analizėje pastebėta, kad vienos jungties inkarų išdėstymo konfigūracijos lemia siauresnį jungties plyšį (siauriausias plyšys nustatytas prie L1 konfigūracijos), kitos – mažiau suvaržo plyšio plotį. S3.2 pav. pavaizduotos keturių skirtingų tipų bandinių (savo kategorijoje pademonstravusių artimiausias vidutinėms reikšmes) jungties šlyties įtempių-sluoksnių pasislinkimo kreivės.

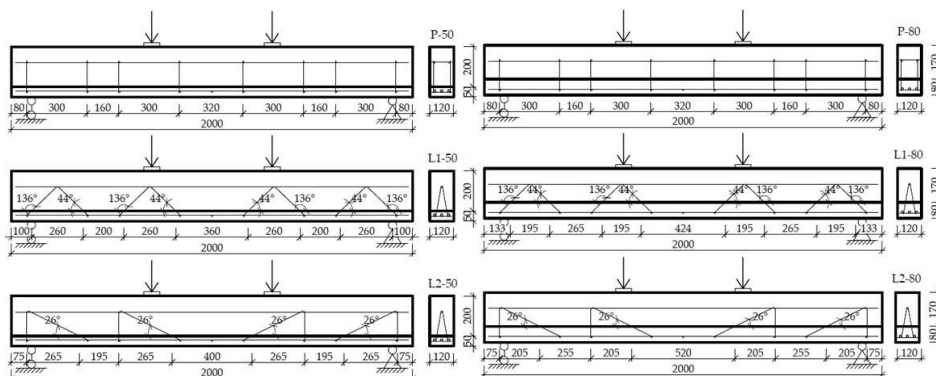


S3.1 pav. 4 tipų betoninių sluoksnių jungčių eksperimentinių tyrimų bandiniai

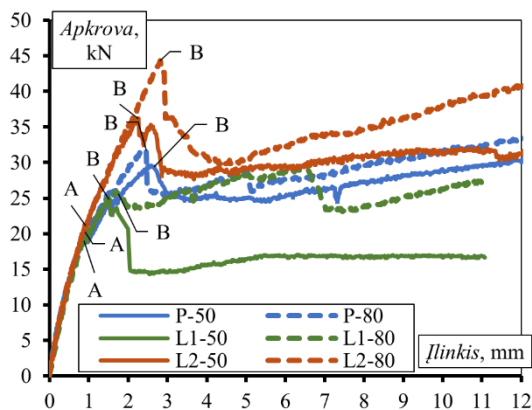


S3.2 pav. 4 tipų betoninių sluoksnių jungčių šlyties įtempių- sluoksnių pasislinkimo kreivės

Šiame skyriuje taip pat pristatyti 6 sluoksniuotų sijų eksperimentiniai bandymai. Šios skyrėsi jungties inkarų išdėstymu (statmeni inkarai, pasvirę) ir sluoksnių storio santykiu. Sijų geometrija pavaizduota S3.3 pav. Nustatyta, kad inkarų išdėstymo konfigūracija lemia jungties laikomąją galią ir lenkiamojo elemento laikomąją galią. Labiausiai jungties šlyties jėgos kryptimi pasvirę inkarai lemia didžiausią konstrukcijos atsparumą (L2 tipo inkarų išdėstymas). Inkarų išdėstymas taip pat lemia ir konstrukcinio pleišėjimo pobūdį. Šioje analizėje taip pat nustatyta, kad sijos su storesniu pirmuoju sluoksniu pasiekia aukštesnę laikomąją galią. S3.4 pav. pateiktos visų sijų įlinkių kreivės.

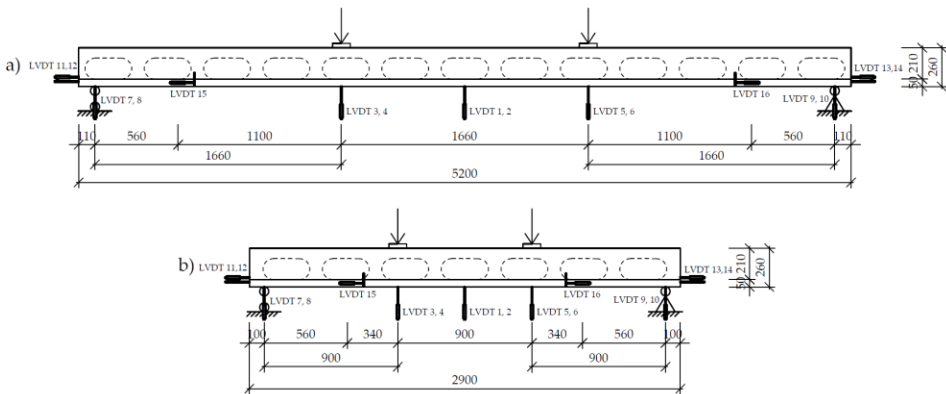


S3.3 pav. 6 sluoksniuotųjų sijų geometrija



S3.4 pav. Sluoksniuotų sijų įlinkių kreivės

Šiame skyriuje pateikti eksperimentiniai surenkamųjų – monolitinių plokščių su plastiko tarpais rezultatai. Išbandytos dviejų skirtingų tarpatramių plokštės. Sijų geometrija pavaizduota S3.5 pav. Nustatyta, kad tarpatramio ilgis lemia pleišėjimo, irimo pobūdį. Ilgesnioji plokštė (S-1) patyrė irimą normaliniame pjūvyje, o trumpesnioji (S-2) – ir normaliniame pjūvyje ir sluoksnių jungtyje. Trumpesniojoje plokštėje nustatytas sluoksnių pasislinkimas. S-1 plokštės bandymas nutrauktas ties 142,8 kN apkrova dėl itin didelio įlinkio (152,8 mm). S-2 plokštės bandymas nutrauktas dėl yrimo gniuždomojoje zonoje. Didžiausia plokštės laikomoji galia buvo 335,4 kN, atitinkanti 137,8 mm įlinkį.

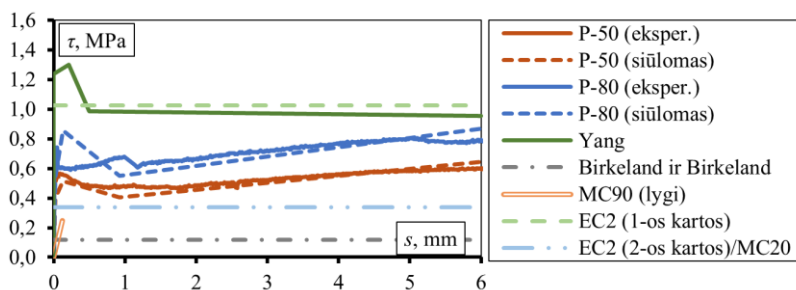


S3.5 pav. Sluoksniuotųjų plokščių su plastiko tarpais bandymo schemas:
a) S-1 plokštė, b) S-2 plokštė

Santraukoje pateikiama autoriaus pasiūlytų analitinių metodų validacija, vaizduojant analitinių skaičiavimų rezultatų lyginimą su P tipo sluoksniuotųjų sijų (S3.3 pav.) eksperimentiniais rezultatais. Pagrindinėje disertacijos dalyje naujų modelių validacija išsamesnė. S3.6 pav. pateiktos eksperimentinės ir analitinės jungties elgsenos kreivės. Matome, kad analitiškai nustatytos kreivės artimos eksperimentinėms. Pasiūlytu modeliu gauti analitiniai rezultatai buvo artimesni eksperimentiniams ir detaliau atvaizduojantys eksperimentinę kreivę negu kiti modeliai iš literatūros. Modelio tikslumas P-50 sijai: $R^2 - 0,94$ ir RMSE – 0,07 MPa. Modelio tikslumas P-80 sijai: $R^2 - 0,75$ ir RMSE – 0,16 MPa. Kitais modeliais gautos R^2 reikšmės svyravo 0,13–0,46 ir RMSE buvo intervale 0,24–0,77 MPa.

S3.1 lentelėje parodytos sluoksnių traukumo skirtumo metodu nustatytas traukumo ir jungties traukumo šlyties įtempių vertės. Naudojantis analitinėmis šlyties įtempių ir sluoksnių pasislinkimo reikšmėmis, nustatomas šlyties standumo modulis skirtingomis jungties darbo stadijomis (S3.2 lentelė). 0, A, B, C, D žymi jungties elgsenos stadijų taškus. Galiausiai, naudojantis sluoksniuoto elemento įlinkio skaičiavimo metodu, vertinant kintančias šlyties standumo modulio reikšmes ir koreguojant konstrukcijos skerspjūvio geometrines charakteristikas, kintančias dėl sluoksnių pleišėjimo, nustatoma analitinės sluoksniuotų sijų apkrovos-įlinkio kreivės (S3.7 pav.).

Matoma, kad analitiniai rezultatai artimi eksperimentiniams. Šioje validacijoje naudojami ir kitų autorių sluoksniuotojo elemento lenkiamojo standumo vertinimo modeliai. Galima teigti, kad Magnucki et al. (2020) modelis yra tinkamas tik iki jungties adhezijos pradžios stadijos, nes nevertina jungties standumo. Tuo tarpu, Peng et al. (2024) modelis vertina jungties standumą, tačiau nepateikia jungties standumo reikšmių nustatymo metodikos. Dėl priimto monolitinio jungties standumo naudojantis šiais modeliais, prie jungties adhezijos pradžios apkrovos nustatytos mažesnės įlinkių reikšmės. Pasiūlyto modelio tikslumas P-50 sijai: $R^2 - 0,99$ ir RSMSE – 0,12 mm. Modelio tikslumas P-80 sijai: $R^2 - 1,00$ ir RMSE – 0,24 mm. Kitais modeliais gautos R^2 reikšmės svyravo 0,92-0,98 ir RMSE buvo intervale 0,48-0,66 mm.



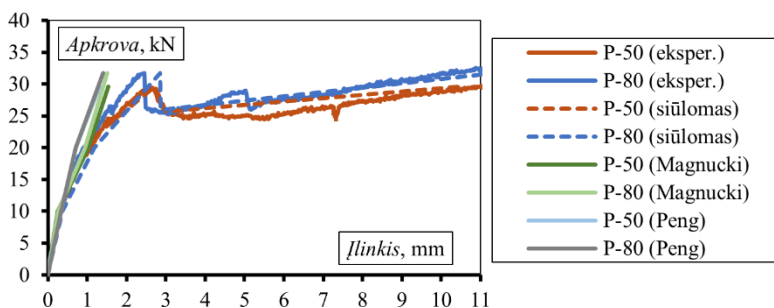
S3.6 pav. Sijų P jungties elgsenos eksperimentinės ir analitinės kreivės

S3.1 lentelė. Sijų P traukumo deformacijų reikšmės

Sija	ε_1 , $\mu\varepsilon$	ε_2 , $\mu\varepsilon$	$\varepsilon_{1,0}$, $\mu\varepsilon$	$\varepsilon_{2,s}$, $\mu\varepsilon$	$\varepsilon_{2,r}$, $\mu\varepsilon$	$\varepsilon_{2,c}$, $\mu\varepsilon$	$\varepsilon_{2,t}$, $\mu\varepsilon$	$\varepsilon_{2,y}$, $\mu\varepsilon$	$\varepsilon_{1,t}$, $\mu\varepsilon$	ε_s , $\mu\varepsilon$	σ_{sh} , MPa
P-50	843	753	751	128	286	24	315	206	93	113	0,56
P-80	843	753	751	112	286	24	331	214	93	121	0,60

S3.2 lentelė. Sijų P jungties šlyties standumo reikšmės

Sija	τ , MPa					S , mm					G_{eff} , GPa				
	0	A	B	C	D	0	A	B	C	D	0	A	B	C	D
P-50	0	0,4	0,5	0,4	0,6	0	0	0,1	0,9	6,0	8,7	8,7	4,0	0,4	0,1
P-80	0	0,5	0,9	0,6	0,9	0	0	0,1	0,9	6,0	8,7	8,7	6,7	0,6	0,1



S3.7 pav. Sijų P eksperimentinės ir analitinės įlinkių kreivės

Bendrosios išvados

1. Darbe pabrėžiama, kad analizuojant sluoksniuotus lenkiamus gelžbetoninius elementus reikia vertinti jungties šlyties standumą. Esamų jungties šlyties standumo modelių kiekis yra nepakankamas, modeliuose nevertinamos kelios jungties elgsenos stadijos ir sluoksnių susitraukimo skirtumo efektas. Be to, daugelis

sluoksniuotos konstrukcijos lenkiamojo standumo modelių nevertina dalinio jungties standumo.

2. Disertacijoje pateikiamas naujas jungties šlyties standumo modelis. Modelis apibūdina jungties šlyties įtempio ir sluoksnių pasislinkimo priklausomybę keturiomis jungties elgsenos stadijomis, vertina sluoksnių susitraukimo skirtumo efektą ir daugelį jungties charakteristikų: betono stipris, inkarų stipris, inkarų koeficientas, jungties šiuurkštumas ir kt. Papildomiems jungties šlyties įtempiams, atsirandantiems dėl sluoksnių susitraukimo skirtumo, įvertinti sukurtas naujas modelis.
3. Darbe pateikiamas naujas sluoksniuotų gelžbetoninių konstrukcijų lenkiamojo standumo modelis, pagrįstas sudėtinių sluoksnių teorija. Jame vertinamas dalinis jungties šlyties standumas. Modelyje naudojamos jungties šlyties standumo vertės nustatomos naujuoju jungties šlyties standumo modeliu.
4. Disertacijoje pristatomas skaitinis sluoksniuotos gelžbetoninės plokštės su plastiko tarpais baigtinių elementų modelis. Rezultatai parodė, kad jungties deformacija sukelia normalinių ir šlyties įtempių persiskirstymą elemente, sumažinamas kompozitinis sluoksnių darbas ir suintensyvėja sluoksnių pleišėjimas. Nustatyta, kad įtempių koncentracijos yra didesnės šalia tarpų tuštumų ir mažesnės betono sienelėse.
5. Atlikus eksperimentinius jungties šlyties tyrimus, padaryta išvada, kad jungties inkarų posvyris ir jungties šiuurkštumas (geometrija) turi didelę įtaką jungties šlyties atsparumui ir standumui. Nustatytas dėsnis dėl jungties inkarų išdėstymo: kuo didesnis inkarų posvyris jungties šlyties jėgos kryptimi, tuo didesnis jungties atsparumas šlyčiai ir standumas.
6. Eksperimentinių sluoksniuotų sijų bandymų rezultatai parodė, kad (panašiai kaip jungties šlyties bandiniuose) sijų jungtys, kurių inkarai buvo labiausiai pasvirę jungties šlyties jėgos kryptimi, pasiekė didžiausią atsparumą šlyčiai ir standumą. Tokios sijos pasiekė didžiausią lenkiamąją galią ir standumą. Sijos su stipresnėmis jungtimis patyrė žymesnį pleišėjimą normaliniame pjūvyje, o sijos su silpnesnėmis jungtimis pleišėjo mažiau. Be to, sijos su storesniais apatiniais sluoksniais pasiekė didesnę lenkiamąją galią ir standumą.
7. Nustatyta, kad eksperimentinės sluoksniuotos gelžbetoninės plokštės su plastikais tarpais suiro normaliniame pjūvyje. Tačiau bandymų metu taip pat pastebėtas jungties pleišėjimas ir sluoksnių pasislinkimas.
8. Siūlomas analitinis metodas validuotas lyginant analitinių skaičiavimų rezultatus su eksperimentinės ir skaitinės analizės rezultatais. Naujasis metodas pademonstravo didesnę sutapimą nei literatūroje esantys modeliai. Nustatytos jungties šlyties įtempių-sluoksnių priklausomybės ir įlinkių reikšmės tinkamai atspindėjo eksperimentinę elgseną, patvirtindamos, kad metodas yra veiksmingas analizuojant sluoksniuotus lenkiamus gelžbetoninius elementus.

Annexes

Annex A. Push-Off Specimen Characteristics

Annex A. Push-Off Specimen Characteristics

Table A.1. Physical characteristics of experimental push-off specimens from the literature, used for the creation of the proposed interface shear stiffness model.

Authors	Number of specimens	Interface roughness	Concrete compressive strength f_c , MPa (first/second layer)	Connector yield strength f_y , MPa	Co-connector ratio ρ	Connector diameter ϕ , mm
Fang et al., 2020	9	Smooth	31.84-49.13/65	285.13-418.98	0.0080-0.0180	8-12
Figueira et al., 2016	3	Smooth	65.50-69.50/43.60-44.80	605.40	0.0107	8
Júlio et al., 2010	4	Smooth	43.00/43.00	443.00	0-0.0035	6
Liu et al., 2021	9	Smooth	25.80-55.60/19.80-51.00	451.00-645.00	0.0050	8
Liu et al., 2019	10	Smooth	83.10/71.70	446.00	0.0050	8
Shaw & Sneed, 2014	6	Smooth	33.51-52.06/33.51-52.06	456.00	0.0133	10
Sneed et al., 2016	6	Smooth, rough	32.89-38.40/32.89-38.40	498.00	0.0090-0.0130	10
Barbosa et al., 2017	4	Rough	28.20/31.30	420.00-550.00	0.0041-0.0064	13-16
Mohamad & Ibrahim, 2015	8	Smooth	36.45-37.98/23.45-24.30	250.00	0.0057	6
Scott, 2010	9	Smooth, rough	53.64-76.53/42.40-43.09	-	-	-
Semen-dary et al., 2020	2	Rough	63.00/136.00	-	-	-
Crane, 2010	2	Smooth	200.00/84.40-200.00	-	-	-

Juozas MASĖNAS

FLEXURAL STIFFNESS MODEL FOR LAYERED
CONCRETE ELEMENTS WITH PARTIAL SHEAR CONNECTION

Doctoral Dissertation

Technological Sciences,
Civil Engineering (T 002)

SLUOKSNIUOTŲJŲ GELŽBETONINIŲ KONSTRUKCIJŲ
SU DALINAI STANDŽIOMIS SLUOKSNIŲ JUNGTIMIS
LENKIAMOJO STANDUMO VERTINIMO MODELIS

Daktaro disertacija

Technologijos mokslai,
Statybos inžinerija (T 002)

Lietuvių kalbos redaktorė Deimantė Grigaitė
Anglų kalbos redaktorė Jūratė Griškėnaitė

2026 04 13. 12,7 sp. l. Tiražas 20 egz.
Leidinio el. versija <https://doi.org/10.20334/2026-018-M>
Vilniaus Gedimino technikos universitetas
Saulėtekio al. 11, 10223 Vilnius
Spausdino UAB „Ciklonas“,
Žirmūnų g. 68, 09124 Vilnius